

Adsorption of Surfactants on Colloidal Silica: Effects of Surface Curvature on the Structure of Surface Aggregates

vorgelegt von
Diplom-Ingenieur
Dersy Marileth Lugo Quijada
aus Maturín – Venezuela

Von der Fakultät II - Mathematik und Naturwissenschaften
der Technischen Universität Berlin
Zur Erlangung des akademischen Grades

Doktor der Ingenieurwissenschaften
Dr. Ing.

genehmigte Dissertation

Promotionsausschuss:

Vorsitzender: Prof. Dr. R. von Klitzing, TU Berlin
Berichter: Prof. Dr. G. H. Findenegg, TU Berlin
Berichter: Prof. Dr. R. Schomäcker, TU Berlin
Berichter: Dr. J. Oberdisse, Université Montpellier II

Tag der wissenschaftlichen Aussprache: 07.04.2010

Berlin 2010

D 83

The difference between a successful
person and others is not a lack of
strength, not a lack of knowledge,
but rather a lack of will.

Vince Lombardi

This work is dedicated to my family (Juan, Carmen, Argenis, Mary C., Argenis E., Kevin and Ernesto), who encouraged me during the performance of my research.

Acknowledgment

First of all, I would like to thank to God for putting on my way such an encouraging and amazingly incomparable advisor like Prof. Dr. Gerhard H. Findenegg, who always reassured me and gave me important advices and inspiration through my work and in my personal life. Who was always like my father to me in Germany, always helping me to grow in all aspects of life. And for whom I feel a great admiration that I cannot describe with words. I only hope that in the future I could find a boss like you.

I would like to express my deep and sincerely gratitude to Dr. Julian Oberdisse from Montpellier University for his constant and friendly support, for his fruitful collaboration in this work and for sharing his knowledge with me every time we met in Germany or in France and most importantly, for opening the door for me to his family (wife and children), who always made me feel like I was in Venezuela during my stay in Montpellier.

I am also sincerely grateful to Dr. Sylvain Prévost for his invaluable advice and guidance on the SANS measurements and fitting of the SANS data, and moreover, for his friendship.

I also acknowledge Prof. Dr. Reinhard Schomäcker, for being my second supervisor, for his amenable and fruitful discussions about my work and for the advice letters written to the DAAD. I want to thank Prof. Dr. Regine von Klitzing for agreeing to be the "Vorsitzenderin" in the defence of my work and for always giving me a lot of motivation.

I would like to express my sincere thanks to the people belonging to the Stranski Laboratory for opening the doors to me and for always being very friendly and for giving me the opportunity to be one member more of this harmonious family. I would like to further address sincere thanks to Guillermo Orts (now in BAM, Berlin), Matthias Karg (now in Melbourne University), Pilar Caamano, Gabi Hedicke, Michaela Dzionara, Ingke Ketelsen, Barbara Paepow, Jens Meissner and Claudia Oppel for their help in my research work, but also especially for the personal support.

Dr. Ralf Schweins from the Institut Laue-Langevin, Dr. Sylvain Prévost from the Helmholtz Zentrum Berlin für Materialien und Energie GmbH and Dr. Alain Lapp from the Laboratoire Léon Brillouin, for their fruitful help during the SANS measurements.

Dr. Dirk Berger from ZELMI (TU Berlin) for his help in the TEM measurements and for the friendly atmosphere in his group.

The Technical Chemistry group from TU Berlin is kindly acknowledged for the harmonic and friendly atmosphere that they offered me when I performed the BET measurements. Moreover I would like to further address sincere thanks to

Gabi Vetter, Henriette Nowothnick, Xiao Xie, Kirsten Langfeld, Benjamin Frank, Hary Soerijanto, Benjamin Beck, Melissa Sudartono and Sebastian Arndt for the personal support.

I would especially like to thank my adoptive sisters in Germany, Dilek Akcakayiran and Pinar Akcakayiran, for always making me feel at home, for always giving me emotional strength and for always being there to listen to me.

Moreover, I am sincerely grateful to Michael Muthig, Yan Zeng, Cagri Üzümlü, Bhuvnesh Bharti, Claire Look, Guillermo Orts, Claudia Oppel, Ingo Hoffman, Anina Barth, Susanne Jähnert, Cristina Giordano, Samuel Dodoo, Kornelia Gawlitza, Paul Wafula, Mariel Saez, Marga Garrido and all those friends, which were once in Berlin sharing amenable time with me. Thanks for your friendship, for your support and for always being there when I needed to talk with a very good friend.

Luis Colmenares and Yahira Ramirez, thanks for giving me the impulse to come to Germany to do my PhD. studies and for your guidance in personal and professional life. You will be always my friend and my family model. I am always acknowledged to God to allow me to meet both of you.

There are no words to express my gratitude to my parents (Carmen Quijada and Argenis Lugo), my sister (Mary Lugo), my brother (Argenis Jr. Lugo), my nephew (Kevin Lisboa) and my brother in law (Ernesto Lara). Thanks for being always there supporting me in my decisions and always giving me the strength to be far away from all of you and to make me feel good every time when I am not motivated.

To my best friend, Juan Milano, as you say “we are one, our decisions are only one”. You are my whole world and heart, who has made me the life most easy to understand, who always is giving me emotional strength, motivation and impulse to reach my goals. You have been always there for me, guiding me, understanding me and always giving me very good advices when I am in the wrong way. I do not know what I will do if you are not with me.

To God for allowing me to enjoy my time during my PhD, for giving me health and for never abandoning me.

Abstract

Adsorbed surfactants can play an important role as a protection layer for the steric stabilization of colloids and for the preparation of nanostructured functional surfaces. In many cases highly curved surfaces are involved, and this surface curvature may have a pronounced influence on the structure and stability of the adsorbed surfactant layer. In order to better understand these influences, the work presented in this thesis focuses on the study of self-assembled structures of three classes of nonionic surfactants and some of their binary mixtures on silica nanoparticles dispersed in water.

The adsorption of an alkyl ethoxylate surfactant ($C_{12}E_5$), two alkyl maltosides (β - $C_{10}G_2$ and β - $C_{12}G_2$) and an alkyldimethylamine oxide surfactant ($C_{12}DAO$), as well as binary mixtures of $C_{12}DAO$ with β - $C_{10}G_2$ and β - $C_{12}G_2$ onto purpose-synthesized silica sols of uniform particle size (mean diameter 16, 27 and 42 nm) was studied by small-angle neutron scattering (SANS). The silicas were prepared by two variants of the Stöber synthesis. Their particle size was characterized by electron microscopy (TEM), dynamic light scattering (DLS), and SANS, and the specific surface area was determined by N_2 adsorption. It was found that $C_{12}E_5$ exhibits strongly cooperative adsorption onto the silica particles with a surface concentration plateau value Γ_{mx} similar to that on flat silica surfaces. Analysis of the SANS profiles of silica sols with adsorbed $C_{12}E_5$ or $C_{12}DAO$ showed that these surfactants do not form a laterally uniform adsorbed bilayer. Instead, spherical surface micelles are formed on particles of 16 nm. For $C_{12}DAO$ a morphological transition from spherical to oblate ellipsoidal surface micelles was found as the diameter of the silica particles increases from 16 nm to 27 and 42 nm. The ellipsoidal surface micelles of $C_{12}DAO$ have similar dimensions as micelles in the bulk solution. β - $C_{10}G_2$ and β - $C_{12}G_2$ show very weak adsorption onto silica beads, but their adsorption can be promoted by $C_{12}DAO$, when small amounts of β - C_nG_2 are present. However, desorption of the surfactants from the particles and formation of mixed micelles in solution occurs if larger amounts of the maltoside surfactant are added.

Zusammenfassung

Die Adsorption von Tensiden an Kolloid-Teilchen kann zu einer sterischen Stabilisierung der kolloidalen Dispersion führen und ist daher von großer Bedeutung für die Herstellung nanostrukturierter funktionaler Oberflächen. Stark gekrümmte Oberflächen spielen in solchen Systemen eine große Rolle und können einen maßgebenden Einfluss auf Struktur und Stabilität der adsorbierten Tensidfilme haben. Die vorliegende Doktorarbeit verfolgt das Ziel, den Einfluss der Oberflächenkrümmung auf die Morphologie der adsorbierten Schicht von nichtionischen Tenside an Silika-Nanoteilchen zu bestimmen.

Die Struktur der Adsorptionsschicht eines Alkylethoxylats ($C_{12}E_5$), der Alkylmaltoside β - $C_{10}G_2$ und β - $C_{12}G_2$, und des Alkyldimethylaminoxids $C_{12}DAO$, sowie von binären Mischungen von $C_{12}DAO$ mit β - $C_{10}G_2$ und β - $C_{12}G_2$ an Silica-Nanoteilchen wurde mittels Kleinwinkel-Neutronenstreuung (SANS) untersucht. Die Silica-Nanoteilchen mit Teilchendurchmessern im Bereich von 16 bis 42 nm wurden nach der Stöber-Methode synthetisiert und mit Elektronenmikroskopie (TEM), dynamischer Lichtstreuung (DLS) und SANS, sowie durch Stickstoff-Adsorption charakterisiert. Die Adsorptionsisotherme von $C_{12}E_5$ zeigt einen stark kooperativen Verlauf mit einem Plateauwert ähnlich wie an atomar glatten Silica-Oberflächen. Die Analyse der SANS-Streukurven der Dispersionen mit $C_{12}E_5$ und $C_{12}DAO$ zeigt, dass diese Tenside an den Silika-Teilchen keine homogene Tensiddoppelschicht, sondern im Falle der kleinsten Silika-Teilchen (16 nm) kugelförmige Oberflächenmizellen bilden. Im Fall von $C_{12}DAO$ konnte mit zunehmender Teilchengröße ein morphologischer Übergang von kugelförmigen zu oblat ellipsoidalen Oberflächenmizellen nachgewiesen werden, die eine ähnliche Größe wie die Mizellen in wässrige Lösung haben. Im Gegensatz zu $C_{12}E_5$ und $C_{12}DAO$ wurde für β - $C_{10}G_2$ und β - $C_{12}G_2$ keine signifikante Adsorption an den Silica-Teilchen gefunden. Es konnte aber gezeigt werden, dass die Adsorption dieser Tenside an Silica-Teilchen durch die Anwesenheit von $C_{12}DAO$ begünstigt wird (synergetischer Effekt). Erhöhung der Konzentration von β - $C_{10}G_2$ und β - $C_{12}G_2$ bewirkt jedoch eine Desorption von $C_{12}DAO$ und die Bildung von Mischmizellen in der Lösung.

Contents

1	Introduction	1
2	Fundamentals	5
2.1	Surfactants.....	5
2.1.1	Surfactants in Solution.....	5
2.1.2	Micellar Structure and Shape.....	8
2.1.3	Mixed Surfactant Systems.....	11
2.2	Adsorption of Surfactants	16
2.2.1	Adsorption at the Air/Liquid Interface.....	17
2.2.1.1	The Gibbs Adsorption Equation.....	18
2.2.2	Adsorption at the Solid/Liquid Interface.....	19
2.2.2.1	Mechanisms of Surfactant Adsorption	20
2.2.2.2	Adsorption Isotherms	21
2.3	Structure of the Surface Aggregates.....	27
2.4	Scattering Techniques	28
2.4.1	Dynamic Light Scattering (DLS).....	29
2.4.2	Small Angle Neutron Scattering (SANS)	22
3	Experimental Section	50
3.1	Chemicals.....	50
3.2	Sample Preparation.....	50
3.2.1	Synthesis of the Silica Nanoparticles	50
3.2.2	Characterization of the Silica Nanoparticles	51
3.2.3	Surfactant Solutions.....	52
3.2.4	Surfactant Adsorption on the Silica Nanoparticles.....	53
3.2.5	Adsorption from Surfactant Mixtures on the Silica Nanoparticles.....	54
3.3	Methods.....	55
3.3.1	Nitrogen Adsorption.....	55
3.3.2	Transmission Electron Microscopy (TEM).....	57
3.3.3	Zeta Potential.....	57

3.3.4	Dynamic Light Scattering (DLS).....	57
3.3.5	Surface Tension.....	58
3.3.6	Small Angle Neutron Scattering (SANS).....	58
4	Surface Aggregate Structure of Nonionic Surfactants on Colloidal Silica Nanoparticles	60
4.1	Introduction.....	60
4.2	Results.....	62
4.2.1	Characterization of the Silica Particles.....	62
4.2.2	Adsorption and Film Thickness of C ₁₂ E ₅ on the Silica.....	65
4.2.3	Characterization of the Adsorbed Layer by SANS	67
4.2.3.1	Core-Shell Model.....	69
4.2.3.2	Micelle-Decorated Silica Model.....	72
4.3	Discussion.....	75
5	Effect of Nanoparticle Size on the Morphology of Adsorbed Surfactant Layers	79
5.1	Introduction.....	79
5.2	Results and Discussion.....	81
5.2.1	Characterization of the Silica Particles.....	81
5.2.2	SANS Study of adsorbed C ₁₂ DAO Layer.....	86
5.2.3	Geometric Modelling.....	89
5.2.4	Core-Shell Model	90
5.2.5	Micelle-Decorated Silica Model	92
5.2.6	Scattering from Index-matched Silica Particles Decorated with Ellipsoidal Micelles.....	98
5.2.7	Influence of the Surfactant Head Group.....	101
5.2.8	Influence of the Nanoparticle Size.....	102
6	Surface Aggregate Structure of Mixtures of Sugar-Based Surfactants with an Amphoteric Surfactant on Silica Beads	105
6.1	Introduction.....	105
6.2	Results and Discussion.....	107
6.2.1	Characterization of the Silica Particles.....	107

6.2.2	Adsorption of the Binary Surfactant Mixtures at the Air/Liquid Interface.....	110
6.2.3	Structure of Surfactant Aggregates in Aqueous Solutions.....	114
6.2.3.1	Geometric Modelling	115
6.2.3.2	Form Factor Models.....	117
6.2.4	SANS Study of the Adsorbed Layer of Surfactant Mixtures on the Surface of Silica Nanoparticles.....	120
6.2.4.1	Geometric Modelling	123
6.2.4.2	Core-Shell Model.....	125
6.2.4.3	Micelle-Decorated Silica Model.....	127
6.2.5	Effect of the Maltoside Surfactants on the Adsorption of C ₁₂ DAO on Silica.....	133
7	Summary and Outlook	138
8	Appendix	143

1 Introduction

Surfactants and their mixtures can drastically change the surface properties of solids and hence they play a key role in many industrial processes such as dispersion/flocculation, corrosion inhibition, drug delivery, colloidal stabilization, enhanced oil recovery, and so on. In this context it is of great importance to get information about the adsorbed amount of surfactant and the structure of the adsorbed layer, in order to improve or to control the desired conditions for the performance of modification of surfaces by adsorption of amphiphilic molecules for a specific technical or biological application. For this reason, many investigations have been performed during the past decades to study the thermodynamics and mechanism adsorption of surfactants at the solid/liquid interface, as well as the molecular organization of the adsorbed surfactants on solids. However, most studies have been centered on the former aspects, based on experimental techniques for the determination of adsorption isotherms and adsorption enthalpies and entropies [1.1]. Pioneering research into interfacial aggregation with adsorption isotherms [1.2] and the surface force apparatus, SFA [1.3] has provided quantitative measures of adsorption but little information on aggregate structures. Modelling of the adsorption mechanisms of surfactants has traditionally been based on the interpretation of adsorption isotherms. However, this first level of investigation is not sufficient for a complete understanding of the surfactant self-assembly structures on solids. Therefore, direct inspection of adsorbed layer of surfactant molecules at the solid–liquid interface is needed. Surface aggregates or hemi-micelles had been proposed as partial surface coverage as early as 1955 in order to explain the shapes of the adsorption isotherms. Subsequently, hemi-micelles were shown to be quite common and there was some headway in determining the structure of these hemi-micelles, particularly their relationship to bulk solution micelles. Theoretical adsorption isotherms were developed which included hemimicelle formation either as well-defined micelles [1.4] or as a patchy monolayer or bilayer [1.5]. Recent efforts to probe these structures on flat surfaces have used fluorescence decay [1.6], neutron reflection [1.7], ellipsometry [1.8] and atomic

force microscopy (AFM) [1.9]. These studies have shown that surfactants often self-assemble on flat hydrophilic surfaces to form structures analogous to those observed in bulk solution, *i.e.* spherical or cylindrical surface micelles, as well as patchy or complete bilayer-type structures. On hydrophobic surfaces surfactants tend to form monolayers or hemi-micellar aggregates. These studies have strongly enhanced the knowledge about adsorbed layer morphologies on flat surfaces. On the other hand, information about the interfacial aggregation of surfactant molecules on colloidal particles is still limited and not yet well understood.

An understanding of the structure of surfactant layers at the surface of nanoparticles in suspensions is of vital importance for the fabrication of nano-structured functional surfaces, which play an important role as a protection layer for the steric stabilization of colloidal dispersions for the preparation of paints, printing inks, agrochemicals, detergents, etc. Non-ionic surfactants are often more attractive than ionic surfactants in these applications due to their weaker salt-sensitivity and their larger tendency to preferentially adsorb to hydrophobic surfaces.

Small-angle neutron scattering (SANS) is the most powerful method to investigate the nature of adsorbed surfactant layers on colloidal solids, as it allows to study structural details at a length-scale of 1 nanometer and below. In addition, it allows to highlight the surfactant layer by matching the colloidal particles with partial deuteration of the solvent. Unlike scanning force microscopy techniques, neutron scattering represents a noninvasive technique, which is of particular importance for detecting soft structures as in the case of adsorbed surfactant layers. Cummins et al. [1.9] performed pioneering work to elucidate the morphology of surfactant layers adsorbed on silica particles 20 years ago. They proposed that alkyl polyoxyethylene ether (C_nE_m) surfactants adsorb on Ludox HS and TM silica sols as a layer of uniform density. However, recent work by Despert and Oberdisse [1.10] has indicated that the structure of the surfactant layer may be more complex than suggested by earlier studies. This was concluded from the fact that the SANS measurements indicated a significantly higher surface area of the adsorbed surfactant than the area of a

surfactant bilayer. It was proposed that the surfactant layer is not laterally uniform but consists of discrete surface micelles. This study was performed with a technical-grade surfactant (Triton X-100) and a commercial silica dispersion (Bindzil). In view of the influence of adsorbed surfactant layers on colloidal particles in many technical fields it was desirable to verify these results and to find out if they apply to a wider class of surfactants or if they may be artifacts caused by the use of a technical-grade surfactant and silica.

The aim of the present work is to gain a better understanding of the morphology of surfactant adsorbed layers on silica nanoparticles of size below 100 nm. In particular, the applicability of the new micelle-decorated silica model of Despert and Oberdisse should be tested for different classes of nonionic surfactants with a low and a high adsorption capacity and to find out to what extent the structure of the adsorbed layer at the surface of the silica nanoparticles depends on the size and chemical nature of the surfactant head group. A longer-term goal of this work is to gain a better understanding of the effects of surface curvature and the influence of size of the silica nanoparticles on the nature and relative stability of the surface aggregates of these surfactants.

A further point of interest in this work was to clarify the nature of mixed surfactant aggregates formed by two nonionic surfactants of different adsorption affinity on colloidal silica sols in a concentration regime, *i.e.* when the amount of the preferred surfactant is not sufficient to cover the silica particles with a complete adsorbed bilayer. In this 'surfactant-deficient' regime the amount adsorbed can be controlled simply by adjusting the overall amount of surfactants in the system. This possibility is of relevance particularly for surfactant mixtures, where it may allow preparing nanoparticles covered by an *asymmetric surfactant bilayer*, such that one surfactant is forming the inner layer, while the other surfactant forms the outer layer of the adsorbed bilayer. It is expected that this situation can arise whenever the surfactant of higher adsorption affinity (component A) is present at an overall amount not sufficient to form a complete bilayer but only half of a bilayer. It is likely that in such a case the surfactant of lower adsorption affinity (surfactant B) may be

accommodated in the outer layer to complete the bilayer. Such a situation may indeed prevail in technically relevant situations when surfactant mixtures are used to stabilize colloidal dispersions.

References of Chapter 1

- [1.1] (a) Király, Z.; Börner, R.H.K.; Findenegg G.H. *Langmuir* **1997**, 13, 3308-3315. (b) Király, Z.; Findenegg G.H. *J. Phys. Chem. B* **1998**, 102, 1203-1211.
- [1.2] (a) Gaudin, A.M.; Fuerstenau, D.W. *Trans Am. Inst. Min. Metall. Pet. Eng.* **1955**, 202, 958-962. (b) Fuerstenau, D.W. *J. Phys. Chem.* **1956**, 60, 981-985.
- [1.3] (a) Pashley, R. M.; Israelachvili, J. N. *Colloids Surf.* **1981**, 2, 169-187. (b) Pashley, R. M.; McGuiggan, P. M.; Horn, R. G.; Ninham, B. W. J. *Colloid Interface Sci.* **1988**, 126, 569-578.
- [1.4] (a) Gu, T.; Zhu, B.-Y. *J. Chem. Soc., Faraday Trans. I* **1989**, 85, 3813-3817. (b) Zhu, B.-Y.; Gu, T.; Zhao, X., *J. Chem. Soc., Faraday Trans. I* **1989**, 85, 3819-3824.
- [1.5] (a) Somasundaran, P.; Fuerstenau, D.W. *J. Phys. Chem.* **1966**, 70, 90-96. (b) Harwell, J.H.; Hoskins, J.C.; Schechter, R.S.; Wade, W.H. *Langmuir* **1985**, 1, 251-262. (c) Böhmer, M.R.; Koopal, L.K. *Langmuir* **1992**, 8, 2649-2659.
- [1.6] Levitz, P.; Van Damme, H.; Keravis, D. *J. Phys. Chem.* **1984**, 88, 2228-2235.
- [1.7] Lee, E. M.; Thomas, R. K.; Cummins, P. G.; Staples, E. J.; Penfold, J.; Rennie, A. R. *Chem. Phys. Lett.* **1989**, 162, 196-202.
- [1.8] Tiberg, F.; Landgren, M. *Langmuir*, **1993**, 9, 927-932.
- [1.9] (a) Manne, S.; Cleveland, J. P.; Gaub, H. E.; Stucky, G. D.; Hansma, P. K. *Langmuir*, **1994**, 10, 4409-4413. (b) Manne, S. ; Gaub, H.E. *Science*, **1995**, 270, 1480-1482. L.K. *Langmuir* **1992**, 8, 2649-2659.
- [1.10] (a) Cummins, P. G.; Staples, E.; Penfold, J. *J. Phys. Chem.*, **1990**, 94, 3740-3745. (b) Cummins, P. G.; Penfold, J.; Staples, E. *J. Phys. Chem.*, **1992**, 96, 8092-8094. (c) Penfold, J.; Staples, E.; Tucker, I.; Cummins, P. *J. Phys. Chem.*, **1996**, 100, 18133-18137.
- [1.11] Despert, G.; Oberdisse, J. *Langmuir*, **2003**, 19, 7604-7610.

2 Fundamentals

This chapter provides a brief overview of the general characteristics of the self-assembly process of surfactants and their binary mixtures in aqueous solutions as well as at the solid/liquid interface.

2.1 Surfactants

The following sections present a brief review of some of the basic concepts pertaining to the formation of surfactant micelles and their behavior at the air/liquid and solid/liquid interfaces. As it is known, surfactants are amphiphilic molecules consisting of a non-polar hydrophobic portion, usually a straight or branched hydrocarbon chain, which is attached to a polar or ionic portion (known as hydrophilic), which can be non-ionic, ionic, or zwitterionic [2.1].

2.1.1 Surfactants in solution

When a surfactant molecule is dissolved in an aqueous medium, the hydrophobic group distorts the structure of the water by structuring the water in the vicinity of the hydrophobic group causing a decrease in entropy and thus an increase of the free energy. As a result of this effect, hydrophobic molecules or groups of a molecule are sparingly soluble in water, *i.e.* are “expelled”. This is the basis of the so-called *hydrophobic effect*. As a consequence some of the surfactant molecules are expelled to the interfaces of the system, with their hydrophobic groups oriented so as to minimize contact with water molecules

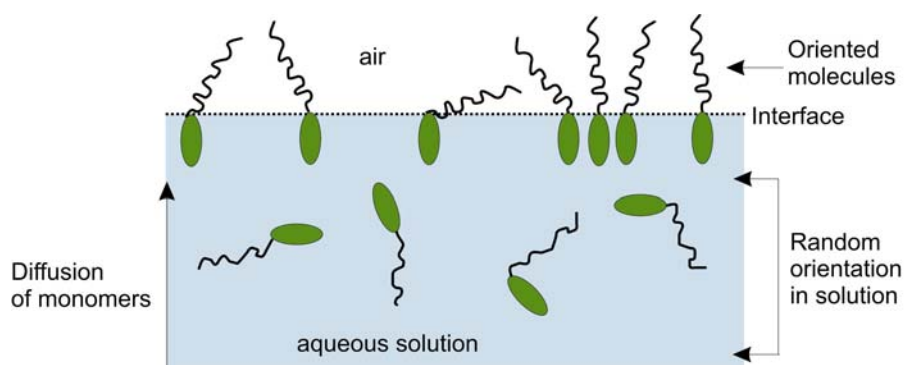


Figure 2.1. Schematic representation of the adsorption process at the air/liquid interface from an aqueous solution of surfactant.

and in this way lowering the system free energy. The surface of the water becomes covered with a single layer of surfactant molecules with their hydrophobic groups oriented predominantly toward the air [2.2], as shown in Figure 2.1. The presence of surfactant at the air/liquid interface results in a decrease of the surface tension due to the molecules of water close to the interface will not be as constrained as it would be without the surfactant molecules. Another mechanism by which the contact of water with the hydrophobic chains of the surfactant can be avoided is surfactant aggregation. Specifically, in micellar aggregates the hydrophobic tails are withdrawn from the contact with water by shielding through the hydrophilic head group (see Fig. 2.2). The micellization phenomenon is predominantly an entropy driven process, which is the result of the hydrophobic effect of the amphiphilic molecules, as well as the repulsive interactions between the head groups of these molecules as they come close to each other in the micelle shell. The concentration at which micelles start to form is known as the critical micelle concentration, *CMC*. Upon reaching the *CMC*, any further addition of surfactants will cause an increase in the number of micelles rather than a further growth of existing micelles.

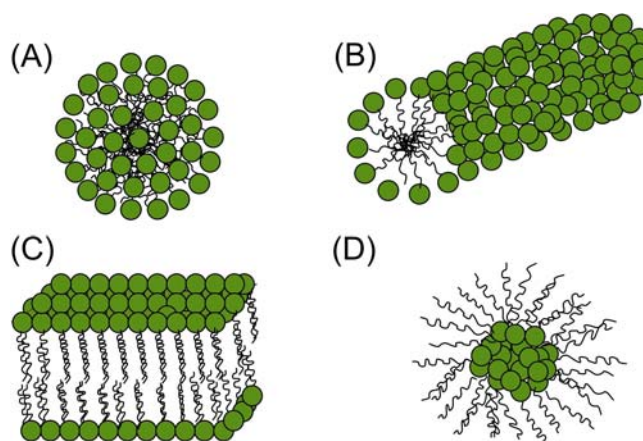


Figure 2.2. Typical self-assemblies of surfactants in solution: (A) spherical micelles; (B) cylindrical micelles; (C) bilayer; (D) inverted spherical micelles (formed in non-aqueous solutions).

The *CMC* can be estimated by measuring physico-chemical properties of the solution, such as turbidity, solubilization, surface tension, equivalent conductivity and so on. It is indicated by an abrupt break of slope in the

measured property as a function of the surfactant concentration. This abrupt change is interpreted as a significant change in the nature of the solute species, *i.e.*, the formation of micelles. The most common technique to measure the *CMC* is by determining the surface tension γ of the solution in a range of concentration, which shows a break at the *CMC*, as is exemplified in Figure 2.3. The value of the *CMC* is affected by several factors. In the present context only those related to the surfactant chemical structure are of relevance: **(i)** the *CMC* decreases strongly with increasing hydrocarbon chain length in a homologous series of surfactants, due to the increase of the hydrophobic interactions; **(ii)** the *CMCs* of nonionic surfactants is much lower than that of ionic surfactants of the same alkyl chain length, because the head groups repel each other less; **(iii)** for nonionic surfactants, *e.g.* with oxyethylene head groups (EO), there is a moderate increase of the *CMC* as the polar head-group becomes larger, which is directly related to the increase of the hydrophilicity of the surfactant molecules; **(iv)** presence of alkyl chain branching and double bonds, aromatic groups or some other polar character in the hydrophobic part produce sizeable changes in the *CMC*; *e.g.*, a dramatic lowering of the *CMC* results from perfluorination of the alkyl chain [2.3].

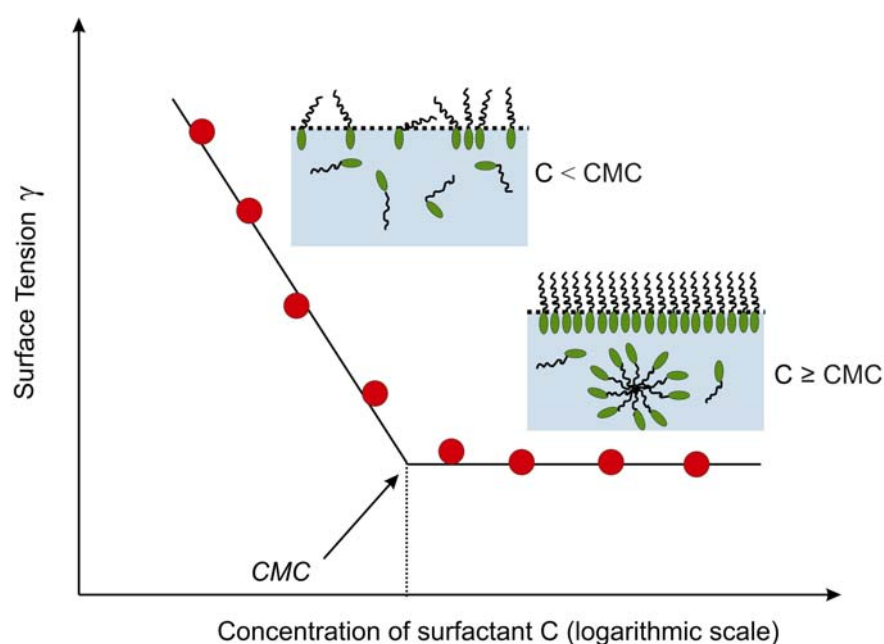


Figure 2.3. Schematic illustration of variation of surface tension of a surfactant solution with surfactant concentration. Typical technique to determine the *CMC* of surfactants in solution.

Along with the *CMC*, the main factor determining the properties of surfactant solutions is the micellar aggregation number n , *i.e.* the number of surfactant molecules in a micelle. Several methods have been used to calculate aggregation numbers of different types of surfactants, such as NMR self-diffusion coefficients, small-angle neutron scattering, static light scattering, etc.

From geometric considerations, the aggregation numbers n of micelles in aqueous media should increase with increasing in the length of the hydrophobic group l_c of the surfactant molecule, and decrease with increase in the cross sectional area of the hydrophilic group a_0 or the volume of the hydrophobic group V [2.2].

2.1.2 Micellar Structure and Shape

The classical picture of micelles formed by simple surfactant systems in aqueous solution is that of spherical micelles, which was first suggested by Adam [2.4] and Hartley [2.5]. They proposed that the spherical micelles have a core of essentially liquid-like hydrocarbon, with a radius approximately equal to the length of the hydrocarbon chain of the surfactant, surrounded by a shell containing the hydrophilic head groups along with associated counterions and water of hydration (see Fig. 2.2A). It is usually assumed that there are no water molecules included in the micellar core, but it is considered that the aqueous phase penetrates until to the first few methylene groups of the hydrophobic chain adjacent to the hydrophilic head, as is supported by Clifford et al. [2.6], and therefore, these methylene groups are often considered in the hydration sphere. Considering this, it is useful to divide the interior region into an outer core that may be penetrated by water and an inner core from which water is excluded. The extent of that water–hydrocarbon contact will be determined by the surface area occupied by each head group and the radius of the core. It seems that the relative ratio between the micellar core volume and surface area must play an important role in controlling the thermodynamics and architecture of the association process.

Tanford [2.7] and Israelachvili, Mitchell and Ninham [2.8] were the pioneers of the two most important ideas to answer the question: how the molecular

structure of the surfactant controls the shape and size of the resulting aggregate? Tanford proposed the concept of opposing forces to formulate a quantitative expression for the standard free energy change on aggregation. Using this free energy expression and the geometrical relations for aggregates, he was able to explain why surfactant aggregates form in aqueous solutions, why they grow, why they do not keep growing but are finite in size, and why they assume a given shape. Israelachvili, Mitchell, and Ninham proposed the concept of molecular packing parameter P_c , and demonstrated how the size and the shape of the aggregates at equilibrium can be predicted from a combination of molecular packing considerations and general thermodynamic principles.

The molecular packing parameter is defined as $P_c = V/l_c a_0$, where V and l_c are the volume and the length of the surfactant tail, respectively, and a_0 is the effective surface area occupied by the surfactant head group at the interface between the micelle core and shell. Depending on the values of P_c , one can predict the possible shape of the micelles (see Figure 2.4 and Table 2.1). The volume V occupied by the hydrocarbon chain can be obtained by using the expression given by Reiss-Husson and Luzzati **[2.9]** $V = 27.4 + 26.9n_c \text{ \AA}^3$, where n_c is the number of carbon atoms of the chain embedded in the micellar core. The length l_c for a chain with n_c embedded carbon atoms is given by $l_c \leq 1.5 + 1.265n_c \text{ \AA}$, depending upon the extension of the chain **[2.7]**. For saturated, straight chains, l_c may be 80% of the fully extended chain, due to the gauche chain conformations. Chain segments located at the transition region from core to shell, for example, cannot assume arbitrary conformations in order to produce a perfectly “smooth,” homogeneous surface. The micellar surface, therefore, must be assumed to be somewhat rough or irregular, although the dynamic nature of the aggregate may obscure any practical effect of such roughness.

The value of a_0 cannot be easily quantified as in the case V and l_c , because a_0 varies not only with the structure of the hydrophilic head group, but

also with changes in the electrolyte content, temperature, pH, and the presence of additives in the solution. Additives, such as medium-chain alcohols that are solubilized in the vicinity of the head groups, increase the effective value of a_0 . With ionic surfactants, a_0 decreases with increase in the electrolyte content of the solution, due to compression of the electrical double layer, and also with increase in the concentration of the ionic surfactant, since that increases the concentration of counterions in the solution. This decrease in the value of a_0 promotes change in the shape of the micelle, e.g. from spherical to cylindrical shape. For polyoxyethylene (PEO) nonionic surfactants, an increase in temperature may cause a change in shape if temperature increase results in increased dehydration of the POE chain.

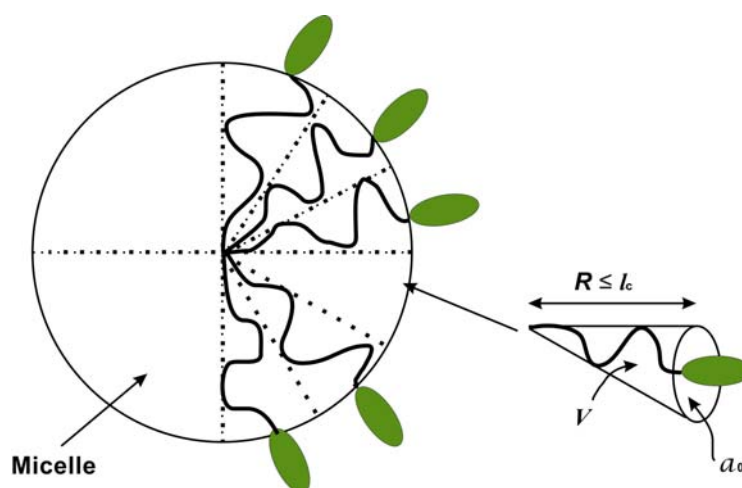







Figure 2.4. Illustration of the geometric parameters for a surfactant and how they influence the size of the micelles.

The micellar shape is determined primarily by the effective cross-sectional area a_0 of the hydrophilic and hydrophobic moieties of the molecules. In aqueous media, surfactants with large water-soluble head groups and small non-polar tails tend to pack into aggregates of highest curvature, *i.e.*, spherical micelles. Micellar shapes of lower mean curvature, such as elongated ellipsoids or oblate shapes will be favored, if the two moieties of the amphiphile have similar cross-sectional areas (*i.e.*, surfactants with short, bulky hydrophobic groups and small, close-packed hydrophilic groups). For example, the addition

of salt or of a co-surfactant to a solution of ionic surfactants causes a structural transition from spherical micelles to cylindrical ones, because the presence of electrolyte or additives screens the head group charge and make it smaller [2.10-2.13].

Table 2.1. Surfactant packing parameter range for various surfactant aggregates. On the right hand a schematic illustration of the representative surfactant shape is displayed.

Structure	Packing parameter, P_c	
Spherical micelles	$P_c < 1/3$	
Cylindrical micelles	$1/3 < P_c < 1/2$	
Vesicles, flexible bilayers	$1/2 < P_c < 1$	
Lamellar, planar bilayers	$P_c \sim 1$	
Inverse micelles	$P_c > 1$	

The geometrical predictions obtained from the molecular packing parameter have been useful for the design of surfactant molecules with specific desirable aggregation characteristics. For commercial surfactants that are mixtures of a homologous series of various chain lengths, that contain potentially surface active impurities (e.g., alcohols), or that have relatively high salt concentrations, care must be taken in extrapolating from model to reality. Likewise, in multiple surfactant systems, a situation commonly encountered in cosmetics, for example, the geometric approach will require a great deal more investigation into possible synergistic interactions before its application becomes widespread.

2.1.3 Mixed Surfactant Systems

Mixed surfactant systems are encountered in many practical applications,

from laundry detergent formulations to industrial and technological systems, due to economical factors as well as beneficial effects of mixtures over individual surfactants. The interaction between different surfactants can lead to synergetic or antagonistic effects, depending on the kinds of surfactants. The most used pairs of surfactants which show synergism are mixtures of a charged and an uncharged compound. The phenomenon of synergism in these cases is due to the interaction between the different head groups. On the other hand, antagonism can be reached by mixing surfactants with the same kinds of head groups, but different kinds of chains, one hydrocarbon and the other perfluorinated, which have a limited solubility in the mixed micelles. This limited solubility is ascribed mainly to the phobicity between the fluorocarbon and hydrocarbon chain, as seen in bulk phases. Because of the incompatibility between these two types of surfactants, the coexistence of two kinds of micelles (one fluorocarbon-rich and one hydrocarbon-rich) has been suggested [2.14]. On the other hand, it has been reported that polyoxyethylene amphiphiles bearing fluorinated or hydrocarbon tails rather form mixed micelles [2.15].

A simple method to determine if a surfactant mixture exhibits synergism or antagonism in mixed micelle formation is to determine the *CMC* of the mixture. If the components of a mixture interact favorably, the *CMC* of the mixture can be less than either the *CMC* of each component in the mixed micelle. But in some cases, the two surfactants interact in such fashion that the *CMC* of the mixture (CMC_{12}) is always intermediate in value between those of the two components of the mixture.

The first thermodynamic treatments of mixed micelle formation were focused on ideal mixing. Thus, Shinoda [2.16] showed that the *CMC*'s of binary mixtures of sodium alkyl carboxylates of different alkyl chain length could be modeled using a formalism based on Raoult's law which relates the *CMC* of the mixture of any composition to the mean of the values for the individual species. Thus, in a micelle containing two surfactants mixing ideally, the *CMC* of the mixture as a function of the surfactant composition can be described by:

$$\frac{1}{CMC_{12}} = \frac{\alpha_1}{CMC_1} + \frac{1 - \alpha_1}{CMC_2} \quad (2.1)$$

where CMC_1 and CMC_2 are the values for the pure surfactants, α_1 is the mole fraction of surfactant 1 in the solution phase on a surfactant only basis (*i.e.*, the mole fraction of surfactant 2 in the mixture is $1 - \alpha_1$).

In Shinoda's work and that of most others, the micelle or surface layer is treated explicitly as a separate phase with a composition distinct from that of the bulk. Clint [2.17] extended this approach to include prediction of monomer activities in the bulk and the micelle composition above the CMC . Rubingh [2.18], Rosen [2.19], and others [2.20] have treated non-ideal binary mixtures using the pseudo-phase separation model (PPS), where non-ideality is included in the form of activity coefficients f of each surfactant in the bulk phase. Thus, the CMC of non-ideal mixture of surfactants as a function of the surfactant composition is given by:

$$\frac{1}{CMC_{12}} = \frac{\alpha_1}{f_1 CMC_1} + \frac{1 - \alpha_1}{f_2 CMC_2} \quad (2.2)$$

Recently, it has increased the investigation of synergism in quantitative terms based upon a simple, convenient method for measuring molecular interactions between surfactants. The molecular interactions between two surfactants at an interface or in micelles are commonly measured by the so-called β parameter [2.21], which indicates the nature and strength of those interactions. β is conveniently obtained from surface (or interfacial) tension or from CMC data by use of equations (2.3)-(2.6). Equations (2.3) and (2.4) are used to calculate the interaction at the air/aqueous solution interface (β^s) from surface tension data [2.21b] (as is shown for the dashed line in Fig. 2.5):

$$1 = \frac{(X_1)^2 \ln(\alpha_1 C_{12} / X_1 C_1^0)}{(1 - X_1)^2 \ln[(1 - \alpha_1) C_{12} / (1 - X_1) C_2^0]} \quad (2.3)$$

$$\beta^{\sigma} = \frac{\ln(\alpha_1 C_{12}^0 / X_1 C_1^0)}{(1 - X_1)^2} \quad (2.4)$$

where X_1 is the mole fraction of surfactant 1 in the total mixed monolayer (on a surfactant-only basis); C_1^0 , C_2^0 , and C_{12} are the molar concentrations in the solution phase of surfactant 1, surfactant 2, and their mixture, respectively, at the mole fraction α_1 of surfactant 1 (on a surfactant-only basis), required to produce a given surface tension, γ , value (obtained from γ -log C plots; see Figure 2.3).

Eqs. (2.5) and (2.6) are used to calculate interaction in the micelles (β^M) from CMC data [2.21a]:

$$1 = \frac{(X_1^M)^2 \ln(\alpha_1 C_{12}^M / X_1^M C_1^M)}{(1 - X_1^M)^2 \ln[(1 - \alpha_1) C_{12}^M / (1 - X_1^M) C_2^M]} \quad (2.5)$$

$$\beta^M = \frac{\ln(\alpha_1 C_{12}^M / X_1^M C_1^M)}{(1 - X_1^M)^2} \quad (2.6)$$

where X_1^M is the mole fraction of surfactant 1 in the total surfactant in the mixed micelle (on a surfactant-only basis); C_1^M , C_2^M , and C_{12}^M are CMC's for surfactant 1, surfactant 2, and their mixture, respectively, at the mole fraction α_1 .

Equation (2.3) (or 2.5) is solved numerically for X_1 , which is then substituted into eq. 2.4 (or 2.6) to calculate β^{σ} or β^M . The experimental determination of β^{σ} and β^M is shown in Figure 2.5. It involves determining the surface tension–log surfactant concentration curves for each of the two individual surfactants in the system and at least one mixture of them at a fixed value of α . For calculating β^{σ} (the molecular interaction parameter for mixed monolayer formation at the air/aqueous solution interface), C_1^0 , C_2^0 , and C_{12} are needed; for β^M , the CMCs, C_1^M , C_2^M , and C_{12}^M are required.

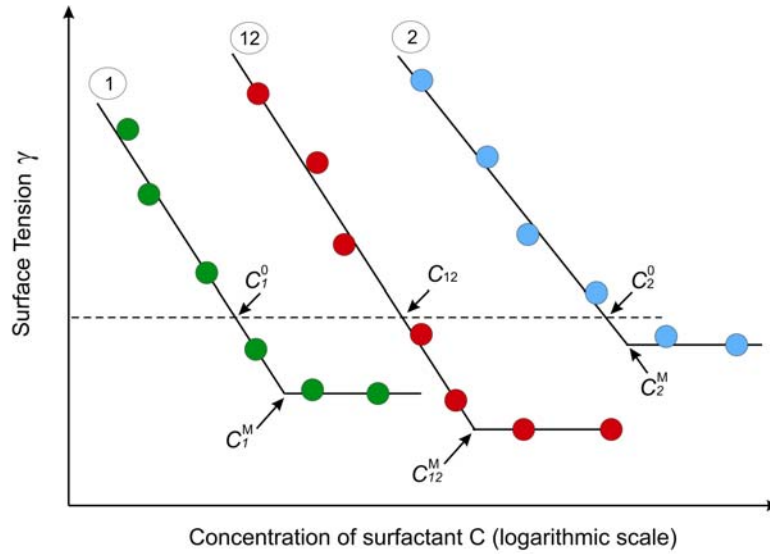


Figure 2.5. Experimental evaluation of β^S or β^M . (1) Individual surfactant 1; (2) Individual surfactant 2; (12) Mixture of surfactants 1 and 2 at a given mole fraction α in solution [2.2].

To obtain valid β^S or β^M parameters, several conditions must be met: **(i)** The surfactants used must be molecularly homogeneous and free of surface-active impurities. **(ii)** For mixtures of ionic and nonionic surfactants, the ionic strength of aqueous solutions of the components of the system and all mixtures of them must be kept constant and, since in the derivation of the equations [2.21a, 2.21b] electrical effects are ignored, it is advisable to use a swamping amount of electrolyte in all solutions. **(iii)** Because the quantity $(X_1)^2/(1 - X_1)^2$ or $(X_1^M)^2/(1 - X_1^M)^2$ in eqs. (2.3) or (2.5), respectively, is subject to a large error as X_1 or X_1^M approaches either 0 or 1, it is advisable to use values of X_1 or X_1^M between 0.2 and 0.8. **(iv)** The common value of γ used in eq. (2.3) should be as low as possible to ensure that the slopes of the γ -log C plots are constant in the regions where C_1 , C_2 , and C_{12} are taken. **(v)** When molecular interactions are strong ($|\beta| > 6$), the change in the average area/molecule at the interface must be taken into account [2.23].

Negative β values are commonly described as indicating attractive interaction between the two surfactants, i.e. synergistic effect of the mixture. When β value is close to zero, this suggests that there is no interaction between these two molecules in the micelles and that the system is ideal.

On the other hand, several investigations about the shape of the micelles formed in mixture systems have been also made. Some authors agree that in this kind of system mixed micelles are formed, but other authors have proposed the coexistence of different shape of micelles in solution. Therefore, this subject is still in study.

2.2 Adsorption of Surfactants

A fundamental characteristic of surfactants is their tendency to adsorb at interfaces in an oriented fashion. In dilute solutions of surface-active agents, the amount of change in any interfacial phenomenon produced by the adsorption of surfactant at the interface is a function of the concentration of surfactant absorbed at the interface. This adsorption process has been studied to determine **(i)** the concentration of surfactant at the interface, since this is a measure of how much of the interface has been covered (and thus changed) by the surfactant; the performance of the surfactant in many interfacial processes (*e.g.*, foaming, detergency, emulsification) depends on its concentration at the interface; **(ii)** the orientation and packing of the surfactant at the interface, since this determines how the interface will be affected by the adsorption, that is, whether it will become more hydrophilic or more hydrophobic; **(iii)** the rate at which this adsorption occurs, since this determines the performance in phenomena such as high-speed wetting or spreading; and **(iv)** the energy changes, ΔG , ΔH , and $T\Delta S$, in the system, resulting from the adsorption, since these quantities provide information on the type and mechanism of any interactions involving the surfactant at the interface, and the maximum concentration that the surfactant can attain at that interface, *i.e.*, the surface concentration of surfactant at surface saturation, Γ_{mx} .

The surface concentration of a surfactant Γ , known also as surface excess or adsorption density, is related to the interfacial area occupied by the surfactant molecule, as will be presented in section 2.2.1.1. For example, the smaller the effective cross-sectional area of the surfactant at the interface, the greater its surface excess of adsorption. Therefore, Γ depends on the structural groupings in the surfactant molecule and its orientation at the interface.

Adsorption can occur at any type of interface, although the distinct characteristics of solid versus liquid interfaces make the analysis of each case somewhat different. For that reason, the discussion of each situation is best presented in the context of specific interfaces. In many practical systems, all four of the principle interfaces may be present, leading to complex situations that make complete analysis very difficult or impossible.

Two kind of situations of physical adsorption can occur at any interface, which one can refer as “positive” or “negative” adsorption. The first situation is met when the interfacial concentration of the adsorbed species is greater than that in the bulk phase(s), which indicates that the interactions between the adsorbate species and the adsorbant are favourable.

2.2.1 Adsorption at the air/liquid interface

The most important fluid interface at which surfactant adsorption occurs is the air/water interface. In this case the surfactant adsorbs with the hydrophilic group pointing towards the liquid leaving the hydrocarbon group pointing towards the air. The presence of surfactant at the air/water interface results in a pronounced decrease of the surface tension γ , as has been previously mentioned in Section 2.1.1 (see Fig. 2.1). The direct determination of the amount of surfactant adsorbed per unit area of air/liquid interface is not generally possible because of the difficulty of isolating the interfacial region from the bulk phase(s) for purposes of analysis when the interfacial region is small, and of measuring the interfacial area when it is large. Instead, the amount of material adsorbed per unit area of interface is calculated indirectly from surface tension measurements. As a result, a plot of surface tension as a function of (equilibrium) concentration of surfactant in the liquid phases (see Fig. 2.3), rather than an adsorption isotherm, is generally used to describe adsorption at this interface. From such a plot the amount of surfactant adsorbed per unit area of interface, *i.e.* Γ , can readily be calculated by use of the Gibbs adsorption equation [2.2].

2.2.1.1 The Gibbs Adsorption Equation

The Gibbs adsorption equation, in its most general form [2.23] is fundamental to all adsorption processes and is described by:

$$d\gamma = -\sum_i \Gamma_i d\mu_i \quad (2.7)$$

where $d\gamma$ is the change in surface tension of the solvent, Γ_i and $d\mu_i$ are the surface excess concentration and the change in chemical potential of any component of the system, respectively.

At equilibrium between the interfacial and bulk phase concentrations, $d\mu_i = RT d \ln a_i$, where a_i is the activity of any component in the bulk (liquid) phase, R is the gas constant and T the absolute temperature. Thus eq. (2.7) can be expressed as:

$$d\gamma = -RT \sum_i \Gamma_i d \ln a_i \quad (2.8)$$

For solutions consisting of the solvent and only one solute, $d\gamma = -RT(\Gamma_0 d \ln a_0 + \Gamma_1 d \ln a_1)$, where subscripts 0 and 1 refer to the solvent and the solute, respectively. The surface excess concentrations Γ_0 and Γ_1 are not independent from each other. For dilute solutions one defines the relative surface excess concentration of the solute, $\Gamma_1^{(0)}$, which corresponds to the value of Γ_1 when $\Gamma_0 = 0$. In addition, the activity of the solute is approximately equal to its molar concentration C_1 , i.e. $a_1 = C_1$. Thus:

$$d\gamma = -RT\Gamma_1^{(0)} d \ln C_1 = -2.303RT\Gamma_1^{(0)} d \log C_1$$

(2.9)

or

$$\Gamma_1^{(0)} = -\frac{1}{2.303RT} \left(\frac{d\gamma}{d \log C_1} \right)_T$$

which is the form in which the Gibbs equation is commonly used for solutions of nonionic surfactants containing no other materials. When γ is in mN/m; $R = 8.31 \text{ J mol}^{-1} \text{ K}^{-1}$, then Γ_1 is in mmol/m².

According to eq. (2.9) the surface excess concentration $\Gamma_1^{(0)}$ can be calculated from the slope of the plot γ vs. $\log C_1$. Accordingly, the maximum surface concentration Γ_{mx} is derived from the linear portion of the plot of γ vs. $\log C_1$, just before *CMC*, as is illustrated in Fig. 2.3.

From the maximum surface excess concentration Γ_{mx} , the minimum area per molecule (in nm²) at the air/liquid interface can be calculated from the relation:

$$A_{1,\min} = \frac{1}{N_A \Gamma_{mx}} \quad (2.10)$$

where N_A is the Avogadro's number.

For surfactants with a single hydrophilic group, either ionic and nonionic, the minimum area occupied by a surfactant molecule at the surface appears to be determined by the area occupied by the hydrated hydrophilic group rather than by the hydrophobic group. The area per molecule $A_{1,\min}$ at the interface provides information on the degree of packing and the orientation of the adsorbed surfactant molecule when compared with the dimensions of the molecule as obtained by use of molecular models.

2.2.2 Adsorption at the solid/liquid interface

The adsorption of surfactants onto a solid surface from solution is an important process in many situations, including those in which we may want to remove unwanted materials from a system (detergency), change the wetting characteristics of a surface (waterproofing), or stabilize a finely divided solid system in a liquid where stability may otherwise be absent (dispersion stabilization). In these and many other related applications of amphiphilic materials, the ability of the surface-active molecule to situate itself at the solid/liquid interface and produce the desired effect is strongly influenced by the chemical natures of the components of the system (solid, surfactant, and

solvent): **(i)** the nature of the structural groups on the solid surface, whether the surface contains highly charged sites or essentially non-polar groupings and the nature of the atoms of which these sites or groupings are constituted; **(ii)** the molecular structure of the surfactant being adsorbed, whether it is ionic or nonionic, and whether the hydrophobic group is long or short, straight or branched chain, aliphatic or aromatic; and **(iii)** the environment of the aqueous phase, its pH, its electrolyte content, the presence of any additives such as short chain polar solutes (e.g. alcohol), and its temperature. Together these factors determine the mechanism by which adsorption occurs, and the surface excess of the surfactant at the interface.

2.2.2.1 Mechanisms of surfactant adsorption

In this sub-section some mechanisms by which surface-active molecules may adsorb onto the solid substrates from aqueous solution are summarized (see Fig. 2.6):

(i) Ion Exchange: involves replacement of protons or other ions at the surface by equally charged surfactant ions [2.24].

(ii) Ion Pairing: adsorption of surfactant ions from solution onto oppositely charged surface sites [2.24a, 2.24c].

(iii) Hydrogen Bonding: hydrogen bond formation between surfactant species and the solid surface species. Normally this mechanism plays a role for surfactants containing hydroxyl, phenolic, carboxylic and amine groups in the head groups. For instance, adsorption of a nonionic surfactant such as ethoxylated alcohol and sugar-based alkyl glucoside on oxide surfaces has been proposed to involve hydrogen bonding [2.25]. In this case, the bond formed between the surfactant functional groups and mineral surfaces should be stronger than that formed between the mineral and interfacial water molecules.

(iv) Adsorption by Polarization of π -Electrons: occurs when the surfactant molecules contain electron-rich aromatic nuclei and the solid adsorbent has strongly positive sites [2.26].

(v) Adsorption by Dispersion Forces: occurs via London–van der Waals dispersion forces acting between hydrophobic adsorbent and adsorbate molecules. Adsorption by this mechanism generally increases with an increase in the molecular weight of the adsorbate or surfactant [2.24a, 2.27].

(vi) Hydrophobic Bonding: occurs when the combination of mutual attraction between hydrophobic groups of the surfactant molecules and their tendency to escape from an aqueous environment becomes large enough to permit them to adsorb onto the solid adsorbent by aggregating their chains [2.28].

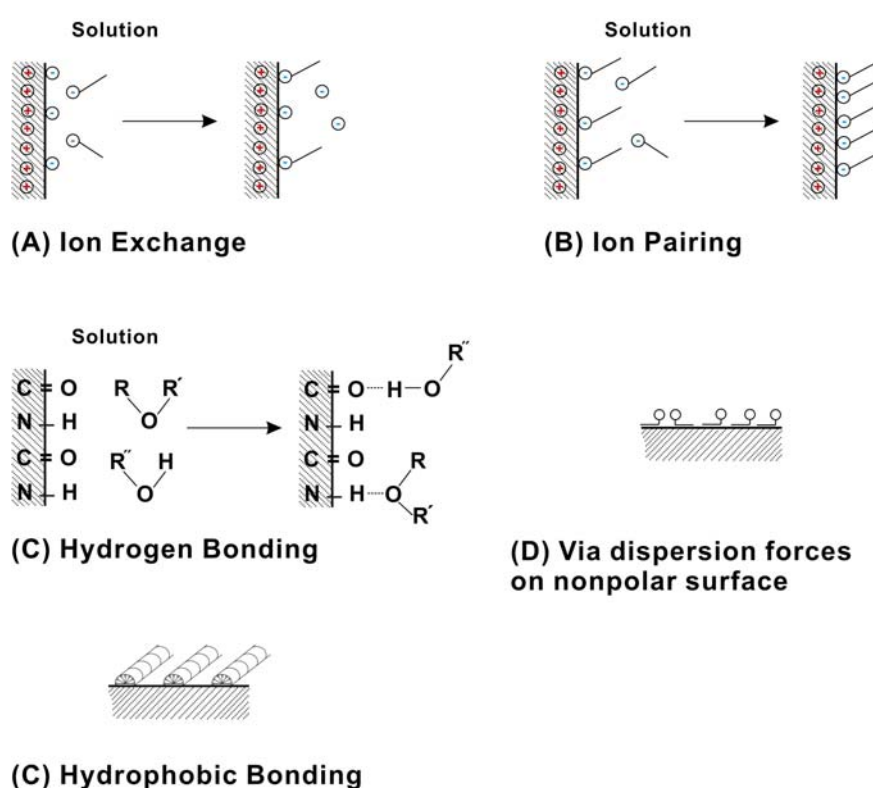


Figure 2.6. Representation of some mechanisms of surfactant adsorption onto the solid substrates from aqueous solution [2.2].

2.2.2.2 Adsorption Isotherms

A conventional method for assessing the adsorption mechanism is through the *adsorption isotherm*, i.e. the functional dependence of the amount adsorbed on the equilibrium concentration in solution. Adsorption isotherms are traditionally determined by solution depletion methods. Here, a surfactant solution of known initial concentration, C_0 , and volume, V , is brought in contact with the adsorbent.

The system is then left to attain equilibrium, which normally takes 1-24 h. The adsorbent are thereafter separated from the bulk solution and the surfactant concentration is determined, thus giving the equilibrium concentration C_{eq} . The adsorbed amount is then obtained from $V(C_0 - C_{eq})$. This quantity is normally expressed either per unit mass or per unit surface area of the adsorbent. The specific surface area of the adsorbent, a_s , can be determined by nitrogen adsorption through a Brunauer-Emmet-Teller (BET) as will described later. Hence, the surface excess Γ can be evaluated by the following expression [2.29]:

$$\Gamma = \frac{(C_0 - C_{eq})V}{ma_s} \quad (2.11)$$

where m is the total mass of the adsorbent.

Adsorption isotherms are generally used to study: **(i)** the nature of solute-surface interaction, which can be qualitatively provided by the shape of the isotherm; **(ii)** the amount of surfactant adsorbed per unit mass or unit area of the solid adsorbent, that is, the surface concentration Γ of the surfactant; **(iii)** the equilibrium concentration C_{eq} of surfactant in the liquid phase required to produce a given surface concentration Γ ; **(iv)** the concentration of surfactant on the adsorbent at surface saturation Γ_{mx} ; **(v)** the rate and extent of adsorption (*i.e.*, monolayer or multilayer formation); **(vi)** the geometric orientation of the adsorbed molecules at the interface; and **(vii)** the effect of environmental factors such as temperature, solvent composition, and pH on the adsorption process and equilibrium.

Due to the complex behavior of amphiphilic surfactant molecules at the solid/liquid interface, several experimental adsorption isotherms of different shapes have been reported in order to try to understand the adsorption mechanism of the surfactant molecules on solid surfaces. Basically, adsorption isotherms can be classified into three types according to their shape: Langmuir type (L-type), S-type and “double plateau” type (L–S type), as shown in Figure 2.7. While the L-type adsorption can be represented by the simple Langmuir

equation [2.30], the mechanisms of S and L–S types are more complex. Some theoretical models have been developed for the description of the adsorption isotherms of S and L–S types. These models have been based on the “two-dimensional condensation” theory [2.31], similar to the “pseudophase separation model” [2.32], taking into consideration the normal potential energies as well as the surface heterogeneity. Later approaches considered the two-dimensional adsorbed structures coexisting with monomers, monolayer and bilayers at the solid/solution interface in the presence of the “excluded volume” effect [2.33]. Somasundaran and Feurstenau [2.34] considered that the electrostatic and hydrophobic lateral interactions are the major driving forces for the adsorption of ionic surfactants on oppositely charged surfaces, and that the adsorption mechanism of ionic surfactants on oxide surfaces can be described by four regions (*c.f.* Section 2.2.2.1 for details). On the other hand, Johnson and Nagarajan [2.35] predicted the nanostructure of cationic and nonionic surface aggregates by comparing the equilibrium free energies for different structures such as spheres, cylinders, and monolayers covered with hemisphere, hemicylinder, finite disk and bilayer. This model can predict the solution concentrations where the surface aggregates transform from one structure to another. In addition to the above, the thermodynamics of the surface aggregation at the solid/solution interface in equilibrium with the bulk solution has been considered by Levitz using the grand partition function [2.36]. Another set of work applied the self-consistent field lattice (SCFL) theory [2.37] originally developed by Scheutjens and Fleer [2.37a] for polymer adsorption. These physical theories of surfactant adsorption relate adsorption to fundamental molecular parameters of the system. On the other hand, they do not yield adsorption isotherms in a single functional form $\Gamma = \Gamma(C)$. In contrast, the simple “one-step” and “two-step” models developed by Gu and Zhu [2.38], represent simple analytical expressions and have been successfully applied for L, S and L–S type isotherms. In this model, the adsorption process is treated as reactions between unoccupied sites and surfactant molecules.

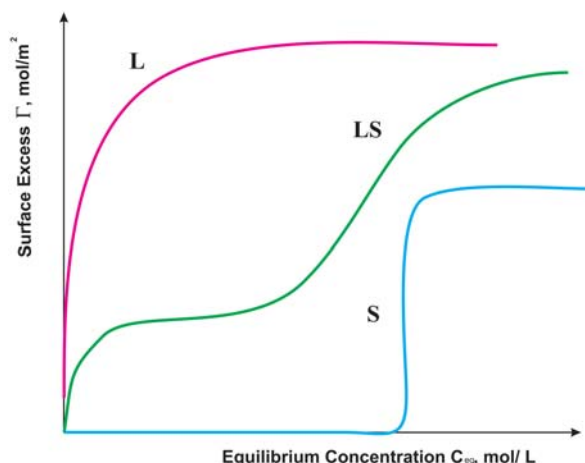


Figure 2.7. Representation of the most common adsorption isotherms to describe the surfactant adsorption process at the solid/liquid interface.

From all above models proposed by different authors, the most common approaches for the interpretation of the adsorption mechanism based on the analysis of the shape of the adsorption isotherms are the four-region, and the one-step and two-step models, which will be described a continuation:

(i) Four-region Adsorption Model: or reverse orientation model was proposed by Somasundaran and Feurstenau [2.34] to describe the adsorption of ionic surfactants on oppositely charged surfaces. The four regions are attributed to four different dominant mechanisms being operative in each of them (see Fig. 2.8). The mechanisms involved in these regions may be described as follows: **Region I**, the adsorption is due to electrostatic interaction between individual isolated charged monomeric species and the oppositely charged solid surface and the adsorption density follows the Gouy–Chapman equation with a slope of unity under constant ionic strength conditions. **Region II**, involves strong lateral interactions between adsorbed monomers, resulting in the formation of surfactant aggregates. Such aggregates are referred to as "solloids" (surface colloids) and include aggregates such as hemimicelles, admicelles and self-assemblies. Therefore, the adsorption density exhibits a sharp increase. **Region III**, exhibits a marked decrease in the rate of adsorption, which is ascribed to the electrically neutralization of the solid surface by the adsorbed surfactant ions. It is thought that this region results from growth of the structures formed in Region II, and that the electrostatic

attraction is no longer operative and adsorption only takes place due to lateral attraction. **Region IV**, a plateau is reached, indicating maximum surface coverage of the solid and normally occurs above the *CMC* of the surfactant. In this stage, the surfactant activity becomes constant and any further increase in concentration causes formation of micelles in solution and does not change the adsorption density. A detailed description of the equations implicated in this model is given in Ref. **2.34**.

This method has been shown to be particularly successful for modeling adsorption behavior of ionic surfactants on oxidic surfaces like alumina and rutile **[2.34, 2.37c]**.

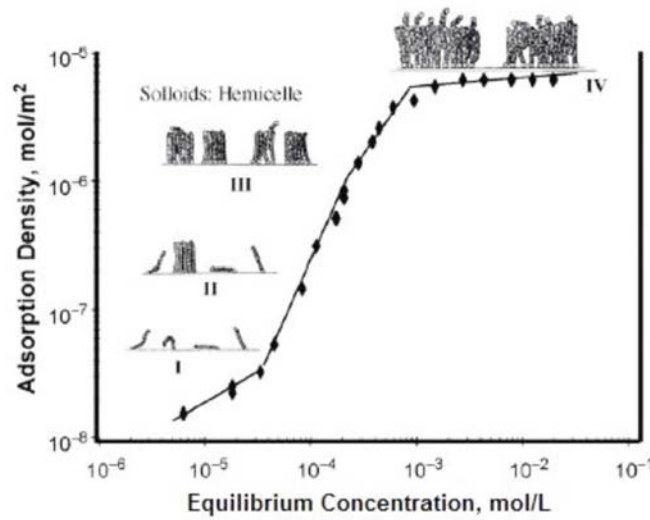


Figure 2.8. The adsorption isotherm of sodium dodecyl sulfate on alumina at pH 6.5. The attached illustrations show of the proposed growth of surface aggregates and orientation of surfactant molecules **[2.34]**.

(ii) One-Step and Two-step Adsorption Model: have been proposed by Gu and Zhu **[2.38]** for the various types of S-shaped adsorption isotherms (non-Langmuir) that are sometimes obtained.

In the one-step model, the surfactant monomer interacts with the active site to form a hemi-micelle, which process can be described by the expression:

$$\Gamma = \frac{\Gamma_{mx} KC^n}{1 + KC^n} \quad (2.12)$$

where Γ is the surface concentration at equilibrium concentration C , Γ_{mx} is the limiting surfactant adsorption at high concentrations, K is the adsorption constant in the low-affinity region, and n is the average aggregation number of the surface aggregates.

Equation (2.12) can be transformed to the logarithmic form:

$$\log[\Gamma / (\Gamma_{mx} - \Gamma)] = \log K + n \log C \quad (2.13)$$

in order to estimate K and n by plotting $\log[(\Gamma/(\Gamma_{mx} - \Gamma))]$ versus $\log C$. When $n = 1$, equation 2.12 becomes the Langmuir adsorption isotherm in the form $\Gamma = \Gamma_{mx}KC/(1+KC)$, where $K = 1/a$ and $a = 55.3 \exp(\Delta G^o / RT)$, in mol/L, at absolute temperature T , in the vicinity of room temperature and where ΔG^o is free energy of adsorption at infinite dilution. If surface aggregation occurs, then n should be greater than 1.

The two-step model is a modified one-step model by considering the adsorption process to occur in two steps. In the first step, the surfactant molecules are adsorbed as individual molecules or ions at concentrations below the critical surface aggregation concentration CSAC. And in the second step, the adsorbed surfactant monomers act as anchors for the formation of hemimicelle.

The general expression for the two-step model is:

$$\Gamma = \frac{\Gamma_{mx} k_1 C (1/n + k_2 C^{n-1})}{1 + k_1 C (1 + k_2 C^{n-1})} \quad (2.14)$$

where the k_1 and k_2 are the equilibrium constants for the first and second reactions, respectively.

Both models have given successful representation of the adsorption of ionic and nonionic surfactants on silica [2.39].

2.3 Structure of the Surface Aggregates

Although adsorption isotherms give indirect information about the adsorption mechanism of amphiphilic molecules, one cannot obtain through them detailed information about the structure of the surfactant aggregates on solid surfaces, known as surface aggregates. In the last decades new techniques have been developed to study these structures formed by the adsorbed surfactants. First, indications that the adsorbed surfactant aggregates on mineral solids represent hemi-micelles were based on wettability, electrokinetic and coagulation experiments, [2.40]. Direct imaging using atomic force microscopy (AFM) at surfactant concentrations above half of the *CMC* has recently shown that the structures of aggregates of nonionic ethoxylated or cationic surfactants on silica sometimes are similar to morphologies of bulk micelles and that the surface aggregates may undergo a sphere-to-cylinder transition as the surfactant concentration increases [2.41]. Although a majority of results from ellipsometry [2.42], small angle neutron scattering [2.43] and neutron reflectivity [2.44] suggested that nonionic ethoxylated and cationic surfactant aggregates exist in the form of patchy or fully covered bilayers, a few exceptions [2.45, 2.46] have been noted using the same techniques. For example, Schulz et al. [2.45] developed a model for micelle-like surface aggregates by analyzing neutron reflectivity data. Despert and Oberdisse [2.46a] analysed the shape of adsorbed surface aggregates of Triton X-100 on silica nanoparticles using small-angle neutron scattering and found that the surface aggregates represent small micelles.

Small-angle neutron scattering (SANS) and dynamic light scattering (DLS) have been used in the present work as the most important methods to get a better understanding of the surface-aggregate structures of single non-ionic surfactants and binary mixtures of them on silica nanoparticles dispersed in aqueous solution. The choice of both techniques complies with the length scale of interest (1-100 nm) and also they can provide structural information without perturbing the sample. While SANS gives direct information about the size and shape of the surface aggregates, DLS is an appropriate method to elucidate the thickness of the surfactant layer at the particles.

In the following sections, the scattering techniques used in this work will be briefly introduced and a detailed description of them will be also given.

2.4 Scattering Techniques

The scattering of light, X-rays and neutrons obeys similar laws. We recall that the scattering arises from fluctuations of electron polarizability for light, the electron density for X-rays and the scattering length related to the properties of the nuclei for neutrons.

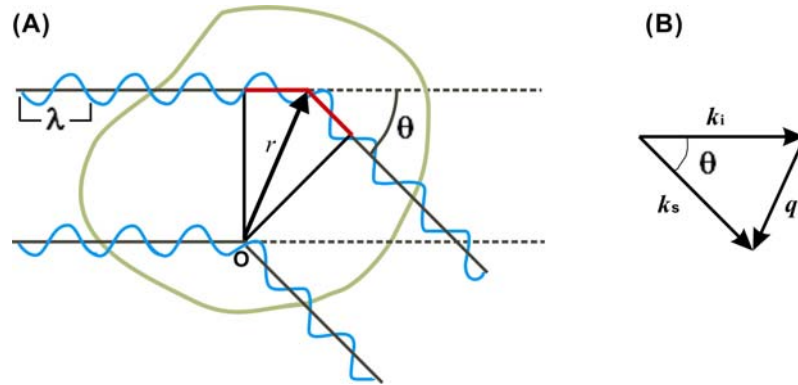


Figure 2.9. (A) A plane wave with wavelength λ is scattered at the origin and at position r inside the scattering medium; (B) Geometric definition of scattering vector q . k_i and k_s are the wave vectors of the incident and scattered waves and θ is the angle between them [2.47].

In general, when a coherent beam (either light, X-rays or neutrons) passes through a sample of volume V , scattered waves of variable intensity are emitted in all directions of space, due to the inhomogeneities in the sample (see Fig. 2.9A). Every point in the sample creates a spherically symmetrical scattered wave with amplitude described by [2.48, 2.49]:

$$A_s(q) \propto b e^{-iqr} \quad (2.15)$$

where r is a position inside the scattering medium relative to the origin, b is the scattering amplitude that depends on the interaction between the material and radiation, and determines the fraction of radiation scattered from the position r , and q is the scattering vector defined by $q = k_s - k_i$ (Fig. 2.9B). For elastic

scattering $|k_s| = |k_i| = 2\pi/\lambda$, where λ the wavelength of the incident beam, and q is expressed by:

$$q = |q| = (4\pi/\lambda)\sin(\theta/2) \quad (2.16)$$

The total amplitude at q is the sum of the waves scattered by all atoms in the sample.

2.4.1 Dynamic Light Scattering

Dynamic Light Scattering, also known as **Photon Correlation Spectroscopy** or **Quasi-Elastic Light Scattering**, can be used to determine the particle size and the size distribution profile of small particles in suspension or in solution and can be also used to monitor the kinetics of time-dependent processes, such as particle aggregation.

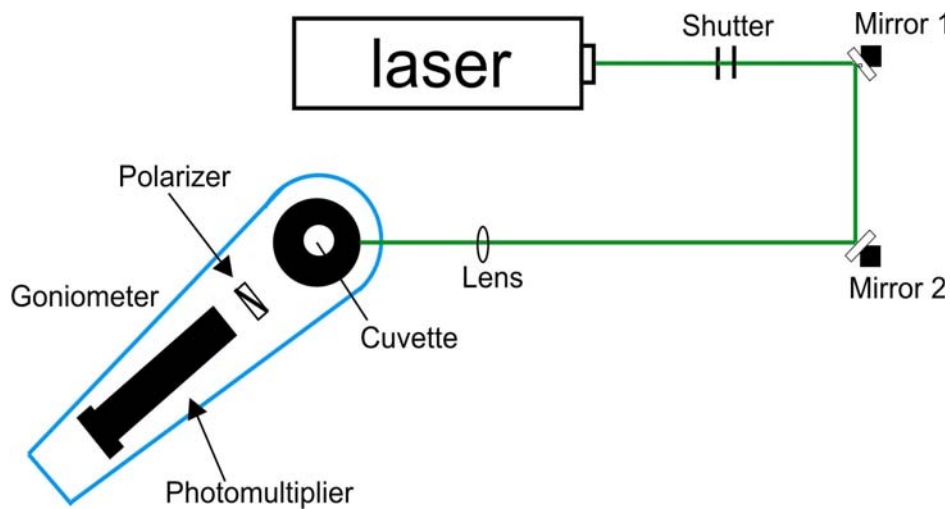


Figure 2.10. Representation of a typical setup for dynamic light scattering experiments [2.50].

A typical light scattering setup is shown in Fig. 2.10. A linear polarized laser light, either from a laser beam which passes through a polarizer or a “good laser”, which itself provides a beam with a relatively high polarization (as in the case of the DLS instrument used in the present work), is guided on the center of the sample cell using a convex lens. Then, the scattered light passes through a polarizer (which ensures that no other light than the scattered light is detected) and is detected by a photodiode, which is mounted on a goniometer

arm. Moreover, pinholes are used to define the optical path and hence the scattering volume. The sample environment in details contains the sample cell made of optical glass (quartz glass), which is placed in the center of a quartz vessel. This vessel is filled with toluene, because matches the refractive index of quartz glass and serves as temperature bath. A PT 100 thermoelement is placed in the matching bath close to the sample cell in order to measure the sample temperature [2.50].

As particles diffuse due to thermal motion, the scattered light undergoes interference effects, and the scattered intensity fluctuates randomly with time. The information about particle size is contained in the rate of decay of the intensity fluctuations $I(t, q)$, *i.e.* rapid diffusion of small particles leads to fast decay, while slow fluctuations result from the motions of larger particles. With modern correlator techniques, one can easily record these fluctuations in terms of the intensity time autocorrelation function $g^2(\tau)$ with the correlation time τ [2.51]:

$$g^2(\tau) = \frac{\langle I(t)I(t + \tau) \rangle}{\langle I \rangle^2} \quad (2.17)$$

The autocorrelation function $g^2(\tau)$ can be related to the normalized correlation function of the electric field of the scattered light $g^1(\tau)$ by the Siegert relationship:

$$g^2(\tau) = \beta_0 + \beta |g^1(\tau)|^2 \quad (2.18)$$

where β_0 is the baseline and β the amplitude of the correlation function, which has the value one in a perfect experiment.

When one considers a suspension of monodisperse spherical particles, this correlation function decays exponentially according to the following expression:

$$g^1(\tau) = \exp(-\Gamma \tau) \quad (2.19)$$

where the relaxation rate Γ is given by:

$$\Gamma = q^2 D \quad (2.20)$$

q is the magnitude of the scattering vector and D is the diffusion coefficient. This relationship shows that the rate of decay depends on the magnitude of the scattering vector, and thus on the scattering angle.

Real samples with a certain polydispersity have a distribution of particle sizes and hence in the diffusion coefficients and relaxation rate. Then, $g^1(\tau)$ can not be described by a simple exponential function and the distribution function of relaxation rates $G(\Gamma)$ has to be considered [2.51]:

$$g^1(\tau) = \int_0^\infty G(\Gamma) \exp(-\Gamma \tau) d\Gamma \quad (2.21)$$

In Figure 2.11 a typical example for the DLS correlation function is shown.

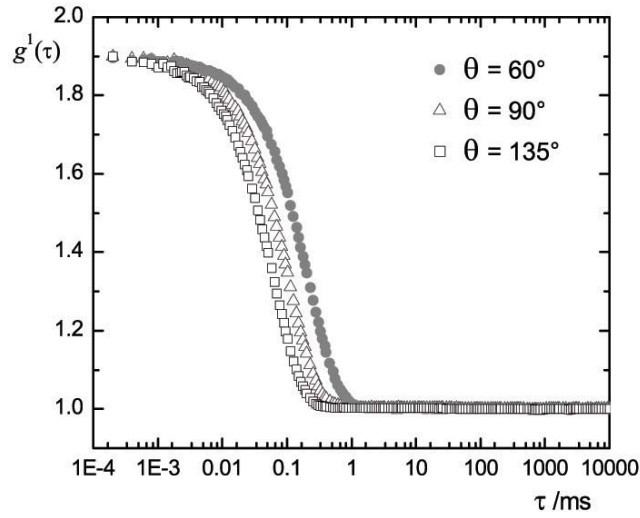


Figure 2.11. Normalized autocorrelation function for silica nanoparticles ($R_H \sim 22$ nm) with $C_{12}E_5$ ($C \sim 5.5 \times 10^{-5}$ mol L $^{-1}$) in water at different scattering angles. The used parameters are $\lambda = 532$, $\eta = 0.8904$ mPas and $T = 298$ K.

The analysis of this function in order to get the mean value of Γ is usually done by the method of cumulants [2.52] or by inverse Laplace transformation (ILT) using the program CONTIN [2.53]. The diffusion coefficient D can be calculated from the DLS experiment using eq. (2.20). Accordingly, the

hydrodynamic radius R_H can be derived making use of the Stokes-Einstein equation:

$$R_H = \frac{kT}{6\pi\eta D} \quad (2.22)$$

with η being the viscosity, k the Boltzmann constant and T the absolute temperature.

2.4.2 Small-Angle Neutron Scattering

While light scattering experiments deal with high wavelengths (typical in the visible range) the wavelength of thermal neutrons is of the order of atomic dimensions, *i.e.* in the range of few Å. This makes neutron scattering well-suited to study structures on a local length scale in the range of atomic or molecular distances.

A general schematic representation of the setup of a SANS instrument is shown in Fig. 2.12, where the basic elements of the instrument include: monochromator, *i.e.* velocity selector, collimator, sample and detector.

Neutrons with a desired wavelength (typical in a range of 0.4 nm to 2nm) are separated from the polychromatic neutron beam, generated by the fission process, using a velocity selector. The monochromatic neutron beam passes a collimation system, which has a comparable function as lenses in optical setups. The collimated radiation of neutrons with flux $I_0(\lambda)$ is incident on the sample, which is placed as close as possible behind the collimation system. This incident neutron radiation is transmitted by the sample, adsorbed and scattered. The flux of neutrons scattered into a solid angle of the detector element $\Delta\Omega$ are recorded by a two-dimensional multidetector, which is positioned at some distance L and scattering angle from the sample. The detector is mounted in a cylindrical, evacuated tube and can move parallel to the flight direction of the neutrons to cover a broad range of momentum transfer q . If the detector is far away from the sample, scattering in a lower angle regime can be resolved and therefore a lower- q range can be studied.

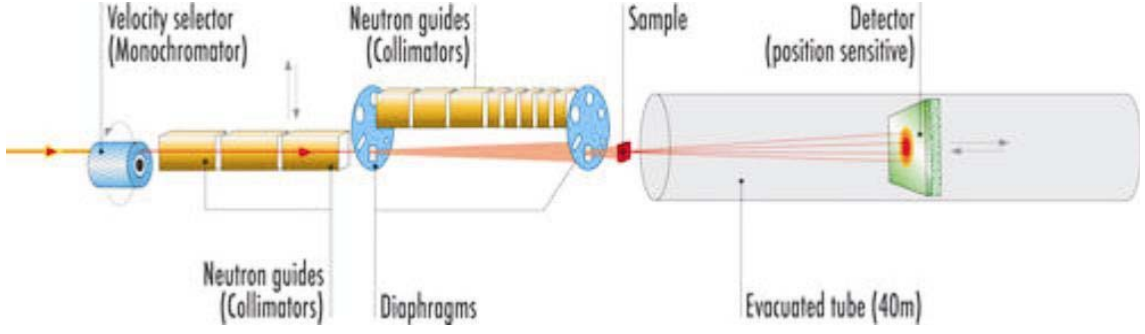


Fig. 2.12. Scheme of a typical setup of a neutron scattering instrument (source: D11 at the Institute Laue.Langevin, Grenoble) [2.54].

The scattered flux $I(\lambda, \theta)$ recorded by the detector can be expressed in general terms as [2.55]:

$$I(\lambda, \theta) = I_0(\lambda) \Delta\Omega \varepsilon(\lambda) T(\lambda) V \frac{\partial \sigma}{\partial \Omega}(q) \quad (2.23)$$

where $\varepsilon(\lambda)$ is the detector efficiency, $T(\lambda)$ and V are transmission and the scattered volume of the sample, respectively. The first three factors on the right-hand side of eq. (2.23) are instrument-specific whilst the last three factors are sample-dependent. From an experimental point of view the most important factor is the last one, the *differential scattering cross section* $(\partial \sigma / \partial \Omega)(q)$, because it contains all the information on the shape, size and interactions of the scattering bodies (assemblies of scattering centres) in the sample. The differential cross-section, also known as scattered intensity $I(q)$ (denomination which will be adopted within this subsection and in the following sections), has the dimensions $1/\text{length}$ and is usually given in cm^{-1} (absolute units). For a two-phase system (*i.e.* scattering objects of uniform composition in an uniform solvent) it is given by [2.47, 2.55]:

$$I(q) = \frac{d\sigma_{coh}}{d\Omega}(q) = \phi \Delta\rho^2 V F(q) S(q) + I_{inc} \quad (2.24)$$

where ϕ is the volume fraction of the scattering objects, $\Delta\rho$ is the contrast, V is the average volume of one scattering object, $F(q)$ and $S(q)$ are the *form factor*

and the *structure factor*, respectively, and I_{inc} denotes the incoherent scattering background.

For dilute samples $S(q)$ with volume fractions ϕ not greater than approximately 1%, $S(q) \approx 1$ and can thus be omitted from eq. (2.24). In this case the scattered intensity after subtraction of I_{inc} is given by:

$$I(q) = \phi \Delta \rho^2 V F(q) \quad (2.25)$$

In order to simplify the analysis of the scattering profile of the samples studied in the present work, dilute solutions were used to determine the size and shape of surface aggregates as well as the shape and size of the silica nanoparticles and the micelles formed by the surfactants in aqueous solution. Accordingly, this analysis is based on eq. (2.25), where the inter-particles interactions are assumed to be negligible, *i.e.* $S(q) = 1$. In the following, the different factors on the right-hand side of eq. (2.25) will be discussed.

The Contrast factor, $\Delta \rho$

The contrast $\Delta \rho$ is given by the difference in neutron scattering length density between the suspended or dissolved particles, and the surrounding medium or matrix, *i.e.* $\Delta \rho = \rho_{particle} - \rho_{solvent}$, where the scattering length densities ρ are usually expressed in units of cm^{-2} .

The value of the scattering length density ρ for each component of the system can be calculated by the sum of all different coherent neutron scattering length b_i of entities “*i*” inside the molecular volume V of the referred component:

$$\rho = \frac{\sum b_i}{V} \quad (2.26)$$

A table with the neutron scattering length b of each atomic nuclei is given by Sears in Ref. **2.56**.

For a two-phase system, if $\Delta \rho = 0$ then from eqs. (2.24) and (2.25) $I(q)$ is also zero and there is no small-angle scattering. When this condition is met the scattering particles are said to be at *contrast match* with the solvent. Since the

scattering from a multi-component solvent is essentially a contrast-weighted summation of the scattering from each individual component, the technique of contrast matching can strongly simplify scattering patterns. This principle can be exploited by *contrast variation*, commonly based on isotope substitution of protons by deuterium atoms, due to their markedly different scattering lengths ($b = -3.739 \times 10^{-15}$ m for ^1H ; and $b = 6.671 \times 10^{-15}$ m for ^2H). For example, in the study of adsorbed layers on solids it is common practice to contrast match the substrate (solid) and the dispersion medium, typically by mixing protonated and deuterated forms of the solvent in an appropriate ratio. In this case the observed scattering arises solely from the adsorbed layer against a uniform background (see Fig. 2.13). Note that in this case, although the particle is contrast-matched by the solvent, the scattering pattern will be affected by the particle size and shape via the form factor of the adsorbed surfactant layer, as outlined below.

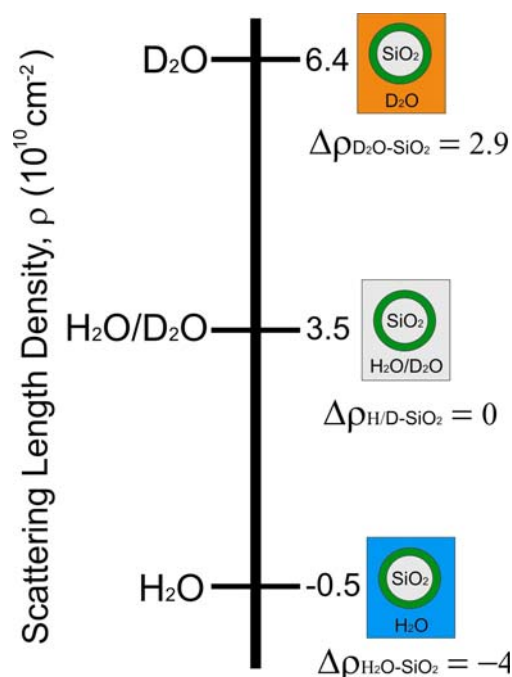


Fig. 2.13. Illustration of the “contrast matching” of a silica particle with a surfactant layer using different $\text{H}_2\text{O}/\text{D}_2\text{O}$ mixtures.

Form Factor, $F(q)$

The form factor is a function that describes how $I(q)$ is modulated by interference effects between radiation scattered from different portions of the scattering object. As a consequence, $F(q)$ is very dependent on the shape of the scattering object. $F(q)$ is termed as normalized particle form factor, when its low- q limit is 1, *i.e.* $F(q) \rightarrow 1$ as $q \rightarrow 0$. $F(q)$ can be calculated by Fourier transformation of the density distribution of the given particle. Below we introduce the form factor functions used within this work:

(i) Homogeneous Sphere. For monodisperse spheres of radius R , $F(q)$ can be expressed as [2.57, 2.58]:

$$F(q) = |f(qR)|^2 \quad (2.27)$$

with

$$f(x) = 3 \frac{\sin(x) - x \cos(x)}{(x)^3}$$

If the scattering objects are polydisperse in size, and if polydispersity can be represented by a log-normal distribution with parameters R_s and polydispersity σ [2.39c, 2.46a]:

$$P(R, R_s, \sigma) = \frac{N/V}{\sqrt{2\pi} R \sigma} \exp\left(-\frac{1}{2\sigma^2} \ln^2 \frac{R}{R_s}\right) \quad (2.28)$$

where N/V is the number density of the scattering objects. The form factor with polydispersity is calculated by integration:

$$F(q) = \int P(R, R_s, \sigma) F(q, R) dR \quad (2.29)$$

The form factor function for monodisperse spheres as well as for polydisperse spheres with a log-normal size distribution integrated in eq. (2.25) is shown as a function of q in Figure 2.14. This figure illustrates that several key features of spherical and more generally globular objects can be determined by SANS measurements.

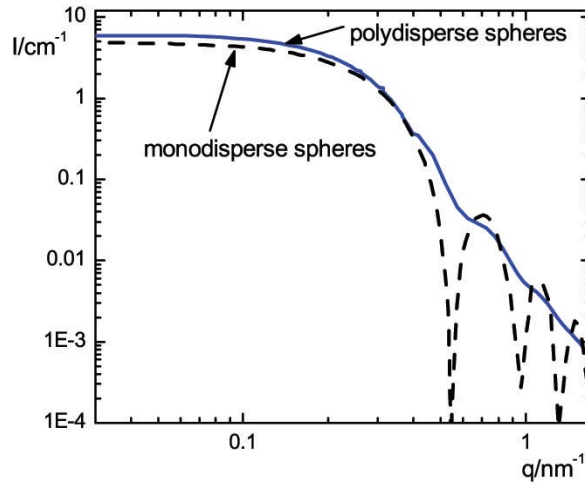


Fig. 2.14. Example of scattered intensities of monodisperse and polydisperse spheres of identical contrast and volume fraction. Monodisperse ($R = 8.2$ nm), polydisperse ($R_p = 8.2$ nm, log-normal size distribution, $\sigma = 0.10$), plotted versus q .

For scattering from a dilute solution of non-interacting particles in the limit of low q , the scattered intensity $I(q)$, is simply related to $(R_g q)^2$, and can be described by the Guinier Approximation:

$$I(q) = I_0 \exp\left(-\frac{q^2 R_g^2}{3}\right) \quad (2.30)$$

where I_0 is the zero angle scattering and R_g is the radius of gyration of the particles, which can be obtained from the slope of the plot $\ln(I(q))$ vs. q^2 (see Fig. 2.15).

The Guinier approximation is strictly valid only in the range in which $qR_g \ll 1$. The determination of scattering data at very low q values is often difficult for experimental reasons. Generally, the Guinier approximation gives estimates which are accurate to within 5-10% if the analysis is conducted using data collected within the range where $qR_g \leq 1$.

The radius of gyration R_g expresses the “typical size” of any finite-sized object and is not only commonly used for particles, but also for polymer coils, and can be related to the dimensions of a variety of well-known scattering

geometries, e.g. in the case spherical particles with radius R , R_g is given by $R_g^2 = (3/5)R^2$. Therefore, the Guinier law is independent of the actual shape, and all form factors for small q will develop universally into the same q -dependence.

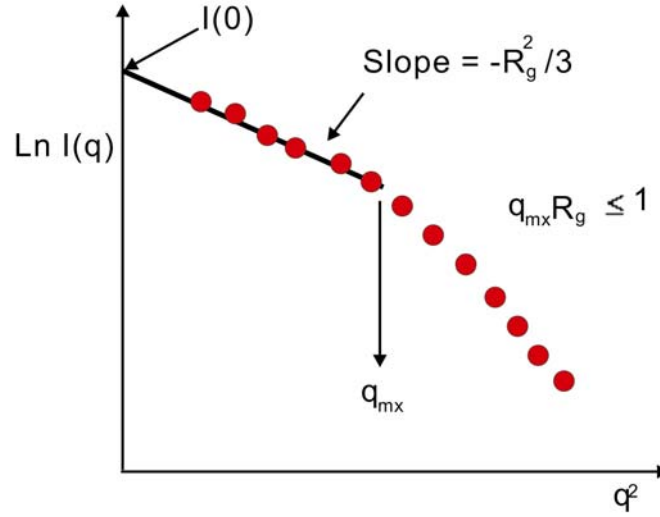


Figure 2.15. Schematic representation of the use of Guinier Approximation.

Another important key in the low- q limit is the zero-angle scattering I_0 , which allows us to access the volume fraction φ of the scattering objects, and thus indirectly the mass of the scattering object:

$$I_0 = \varphi \Delta \rho^2 V \quad (2.31)$$

where V is the volume of the scattering objects.

In Figure 2.14 but at large q values, the scattered intensity is proportional to the surface between the particle and the “matrix”. In this regime, $I(q)$ falls off rapidly, following a power-law envelope, $I(q) = A_P/q^4$ for sharp phase boundaries. This is called Porod scattering, and it is observed for well-defined sharp interfaces. The Porod constant A_P can be directly related to the specific surface of the particles, S/V by the following expression [2.48, 2.58]:

$$A_p = 2\pi\Delta\rho^2 \frac{S}{V} \quad (2.32)$$

In the case of spheres, the specific surface can be easily calculated from the radius and volume fraction of spheres, $S/V = 3\phi/R$, and vice versa. To summarize, the radius R of monodisperse spheres can be determined from $I(q)$ in the Guinier regime at low q , and from the Porod decay at high q . If these numbers agree, one may be quite sure of the spherical nature of the scattering objects. In contrast if they are in strong disagreement, there are different possible explanations: deviations from sphericity, or polydispersity, or both. An example of the scattering profile for polydisperse spheres is also shown in Figure 2.14. The contribution of different ensemble averages to different parts of the intensity leads to an increase in the apparent particle volume (given by the low-angle limit, proportional to $\langle V^2 \rangle / \langle V \rangle$, where the brackets $\langle \rangle$ denote the average over the size distribution), but it also affects the Guinier domain (its square is given by $\langle R^8 \rangle / \langle R^6 \rangle$), and the radius deduced from the Porod regime $\langle R^3 \rangle / \langle R^2 \rangle$. Moreover, the oscillations of the form factor are almost completely wiped out by polydispersity [2.58].

$$R_G^2 = \frac{\langle R^8 \rangle}{\langle R^6 \rangle} = R_s^2 e^{14\sigma^2} \quad (2.33)$$

$$R_p = \frac{\langle R^3 \rangle}{\langle R^2 \rangle} = R_s e^{5\sigma^2/2} \quad (2.34)$$

It is important to notice that different assemblies of particles can give very similar in theory even identical – scattering profiles $I(q)$. For example, polydisperse spheres and ellipsoids, may yield the same $I(q)$. This is due to the loss of the phase information of the radiation when measuring its intensity instead of its amplitude. Fitting of scattering data will therefore never give a unique solution. One way out of this dilemma is cross-checking with other techniques, like direct imaging (TEM, etc.). Another way is to concentrate on

main features of the intensity, as outlined above: average volume (low- q), average radius (intermediate- q), and average specific surface (high- q) are robust parameters measured without ambiguity. Combining them should give a good hint of what the structure might be.

(ii) Spheres with an adsorbed layer. The form factor of spherical particles with an adsorbed layer of surfactant or polymer can be modeled by using a simple core-shell model, as shown in (Fig. 2.16A), which has been parameterized with an inner radius R and a shell thickness δ . Its form factor can be represented as [2.39c, 2.43, 2.46a, 2.59]:

$$F(q, R) = \left[\frac{4\pi}{3} (R + \delta)^3 f(q(R + \delta)) - \frac{4\pi}{3} R^3 f(qR) \right] \quad (2.35)$$

Here R denotes particle radius, δ layer thickness and $f(x)$ is defined in eq. (2.27); where in the first term $x = q(R + \delta)$ and in the second term $x = qR$. The polydispersity of the particles could be included by integration similarly as in eq. (2.29).

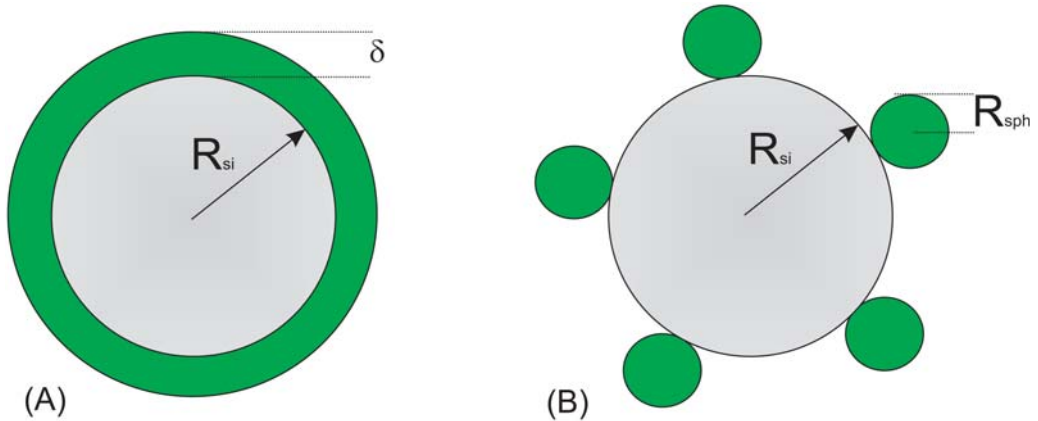


Figure 2.16. Schematic representation of surfactant self-assembly structures on silica beads: (A) spherical core-shell model; (B) micelle-decorated silica model with spherical surface micelles.

For a spherical particle with attached surfactant aggregates in the form of isolated, identical, spherical surface micelles, which interact only through

excluded volume interactions (see Fig. 2.16B), the scattered intensity $I(q)$ can be calculated according to the micelle decorated silica model [2.39c, 2.46a]:

$$I(q) = \frac{N}{V} N_{mic} \Delta\rho^2 V_{mic}^2 F_{mic}(q) S_{mic}(q) S(q) \quad (2.36)$$

where $F_{mic}(q)$ is the normalized form factor of free micelles of volume V_{mic} , modeled as monodisperse spheres; $S(q)$ is the inter-particle structure factor and $S_{mic}(q)$ is the inter-micellar structure factor of micelles sticking to one silica particle, (*cf.* ref. 2.46a for details). In the calculations of $S_{mic}(q)$ the polydispersity in the radius of the particles, which leads to a polydispersity in the number of adsorbed micelles, is taken into account. The data are convoluted with the resolution function.

(iii) Homogeneous ellipsoids. An ellipsoid having two equal equatorial semiaxes (*i.e.*, a spheroid) can be described by the length of the equatorial axis R_e and the ratio v between the principal axes and equatorial axes (see Fig. 2.17A). If the equatorial semi-axis R_e is larger than the principal axis the spheroid becomes oblate, *i. e.* $v < 1$, and if it is smaller it becomes prolate, *i. e.* $v > 1$. orientationally averaged form factor is expressed as [2.59]:

$$F_{ell}(q) = \int_0^\pi f^2(qR_e \sqrt{v^2 \cos^2 \theta + \sin^2 \theta}) d\theta \quad (2.37)$$

where $f(x)$ is the function defined in eq. 2.27.

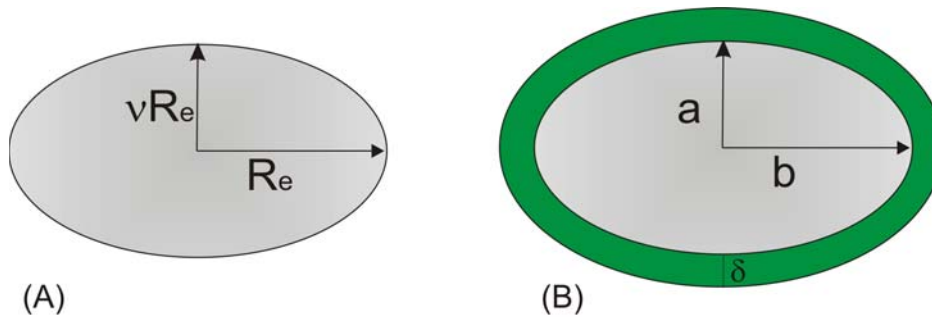


Figure 2.17. Schematic representation of: (A) homogeneous ellipsoid; (B) core-shell ellipsoid.

(iv) Ellipsoids with an adsorbed layer. For a particle of ellipsoidal shape having two equal equatorial semiaxes which is coated by a homogeneous layer of thickness δ , assumed to be the same along the short and long axes (see Fig. 2.17B), the form factor is given by [2.59]:

$$F(q, \mu) = \Delta\rho_{p-sh} V_p \left[\frac{3j(x_p)}{x_p} \right] + \Delta\rho_{sh-sol} V_t \left[\frac{3j(x_t)}{x_t} \right] \quad (2.38)$$

where μ is a orientation variable related to spatial average of the ellipsoid over all possible orientations, equal to the cosine of the angle between \mathbf{q} and the direction of the spheroid major axis parameter, and the function $j(x)$, and parameters x_p, x_δ, V_p, V_t are given by [2.59]:

$$j(x) = \frac{\sin(x) - x \cos(x)}{(x)^2} \quad (2.39)$$

$$x_p = q \sqrt{a^2 \mu^2 + b^2 (1 - \mu^2)} \quad (2.40)$$

$$x_t = q \sqrt{(a + \delta)^2 \mu^2 + (b + \delta)^2 (1 - \mu^2)} \quad (2.41)$$

$$V_p = \frac{4}{3} \pi a b^2 \quad (2.42)$$

$$V_t = \frac{4}{3} \pi (a + \delta) (b + \delta)^2 \quad (2.43)$$

(v) Wormlike micelles. The form factor of wormlike micelles with cylindrical cross-section with radius R_{core} , Kuhn-length l and contour length L was used in this work to model the scattering profile of aqueous solutions of the surfactant pentaethylene glycol monododecyl ether ($C_{12}E_5$). In this model the form factor for worm-like micelles are approximated by the form factor of the Kholodenko-worm [2.59], where the scattering length density profile across the worm segments is described by that of a rod-like micelle:

$$F_{core}(q, R_{core}, l, L) = F_{worm}(q, l, L) F_{cs}(q, R_{core}, \delta, R_g) \quad (2.44)$$

the contribution of the worm-like conformation of the micelle $F_{worm}(q, l, L)$ is described by the equation of Kholodenko for worm-like structures given in ref. **2.60**. The contribution of the cross-section F_{cs} is given by:

$$F_{cs}(q, R_{core}, \delta, R_g) = \left[\frac{2J(qR_{core})}{qR_{core}} \right]^2 \quad (2.45)$$

and $J(x)$ is the first order Bessel function.

(vi) Cylindrical micelles. The form factor of cylindrical micelles with circular cross-section endcaps (see Fig. 2.18) was used in this work to model the scattering profile of aqueous solutions of the surfactant mixtures of dimethyldodecylamine-*N*-oxide (C₁₂DAO) and the alkyl maltoside β -C₁₂G₂. The scattering from cylindrical micelles with a core (R, L) containing the hydrocarbon group and a shell ΔR containing the hydrated head group is given by **[2.59]**:

$$I_{cyl}(q) = \int_0^1 (f_{cyl}(q, \Delta\rho_{c-shell}, R, L, x) + f_{cyl}(q, \Delta\rho_{shell-solv}, R + \Delta R, L + 2\Delta R, x))^2 dx \quad (2.46)$$

where, for example:

$$f_{cyl}(q, \Delta\rho, R, L, x) = 2\pi R^2 L \Delta\rho_{c-shell} \frac{J(qR\sqrt{1-x^2})}{qR\sqrt{1-x^2}} \frac{\sin(qLx/2)}{qLx/2} \quad (2.47)$$

and $J(x)$ is the first order Bessel function.

Structure Factor in interacting systems, $S(q)$

The structure factor is a function that describes how $I(q)$ is modulated by interference effects between radiation scattered by different scattering bodies. Consequently it is dependent on the degree of local order in the sample and

reflects the positional correlations between particles. The Fourier transform of the particle pair correlation function can be written in terms of the position r of N particles as [2.57, 2.58, 2.61]:

$$S(q) = \frac{1}{N} \sum_{j=1}^N \sum_{k=1}^N \exp(-iq(r_j - r_k)) \quad (2.48)$$

where r_j and r_k represent the position of two interacting particles.

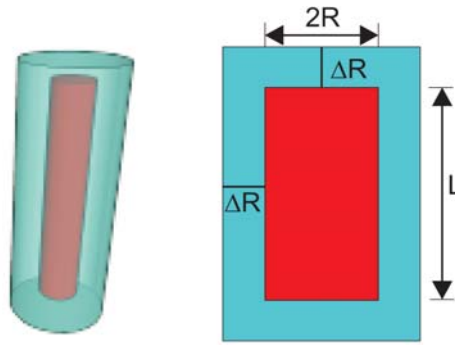


Figure 2.18. Schematic representation of cylindrical micelles with circular cross-section endcaps [2.59].

For anisotropic systems, the vectorial dependences of $S(q)$ need to be kept, whereas in isotropic systems the exponential can be replaced by a $\sin(x/x)$, with $x = q\Delta r$. In Figure 2.19 the influence of the structure on the scattering is illustrated. In dilute systems, where the range of interaction between particles is smaller than the average distance, particles are not positionally correlated, like in a gas, and $S(q) = 1$. In this case, only the particle form factor $F(q)$ is measured by $I(q)$ (see Fig 2.14). At higher concentrations, $S(q)$ deviates from 1, and in the case of repulsive interactions the average distance between particles, D , also becomes the most probable distance. In this case $S(q)$ exhibits a peak at $q_0 \approx 2\pi/D$, and this structure peak at q_0 can be used to estimate the particle radius R if the volume fraction of particles in the dispersion, ϕ , is known. If the particles form a simple cubic lattice model the volume per particle is $V = D^3 = (2\pi/q_0)^3$. Since the particle volume $V_{\text{particle}} = (4\pi/3)R^3$ is given by $V_{\text{particle}} = \phi D^3$ one finds [2.62]:

$$R = \sqrt[3]{\frac{6\pi^2\varphi}{q_0^3}} \quad (2.49)$$

One may note that it is good practice to measure if possible the form factor at high dilutions ($S = 1$), and obtain directly $S(q)$ at higher particle concentrations using Eq. (2.24) by division [2.58]. The structure factor can then be compared to theoretical predictions. These can be obtained quite easily either by numerical simulation or by using published structure factors. The latter are usually derived from the Ornstein–Zernicke equation [2.63] with specific closure relations used for certain types of interparticle potentials. Specifically, the simply analytical Percus–Yevick closures are appropriate for particles with short-scale repulsion, including hard sphere interactions [2.64], whereas the rescaled mean spherical approximation is good for long-range repulsion, including electrostatic interactions [2.65].

Fig. 2.19 shows the effect of repulsive inter-particle interactions on the scattering profile of a dilute dispersion of silica particles. One observes a weak correlation peak at $q_0 \approx 0.1 \text{ nm}^{-1}$. This feature is missing in the scattering profile of non-interacting particles (see Fig 2.14).

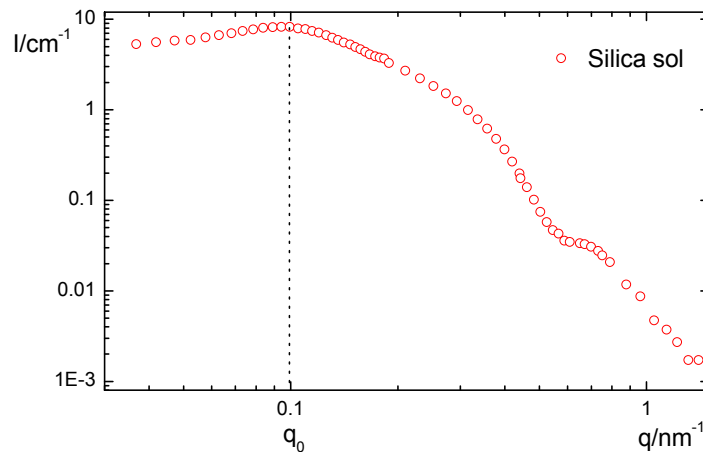


Figure 2.19. Scattering profile for 1.8 wt-% silica dispersion in nearly pure D_2O at pH 9 (298 K).

References of Chapter 2

- [2.1] Tadros, T. F., *Applied Surfactants*, **2005**, 1st ed., Wiley VCH: UK.
- [2.2] Rosen, M.J., *Surfactants and Interfacial Phenomena*, **2004**, 3rd ed., Wiley Interscience, New York.
- [2.3] Lindman, B. in *Handbook of Applied Surface and Colloid Chemistry*, Vol. 1, **2002**, 1st ed., ed. K. Holmberg, John Wiley & Sons, LTD, England, chap. 19, pp 421-442.
- [2.4] Adam, N. K. *J. Phys. Chem.* **1925**, 29, 87-101.
- [2.5] Hartley, G. S., *Aqueous Solutions of Paraffin Chain Salts*, **1936**, Hermann and Cie, Paris.
- [2.6] (a) Clifford, J.; Pethica, B. A. *Trans. Faraday Soc.* **1964**, 60, 1483-1490. (b) Clifford, J. *Trans. Faraday Soc.* **1965**, 61, 1276-1282.
- [2.7] (a) Tanford, C. *J. Phys. Chem.* **1972**, 76, 3020-3024. (b) Tanford C. *J. Phys. Chem.* **1974**, 78, 2469-2479. (c) Tanford C. *Proc. Nat. Acad. Sci USA* **1974**, 71, 1811-1815.
- [2.8] (a) Israelachvili, J. N.; Mitchell, D. J.; and Ninham, B.W., *J. Chem. Soc. Faraday Trans. 1* **1976**, 72, 1525-1568. (b) Israelachvili, J. N.; Mitchell, D. J.; Ninham, B.W. *Biochim. Biophys. Acta* **1977**, 470, 185-201.
- [2.9] Reiss-Husson, F.; Luzzati, V. *J. Phys. Chem.* **1964**, 68, 3504-3511.
- [2.10] Ikeda, S.; Hayashi, S.; Imae, T. *J. Phys. Chem.* **1981**, 85, 106-112.
- [2.11] Ranganathan, R.; Peric, M.; Medina, R.; Garcia, U.; Bales, B. L. *Langmuir* **2001**, 17, 6765-6770.
- [2.12] Zhang, W.; Li, G.; Mu, J.; Shen, Q.; Zheng, L.; Liang, H.; Wu, C. *Chinese Science Bulletin* **2000**, 45, 1854-1857.
- [2.13] Acharya, D. P.; Sato, T.; Kaneko, M.; Singh, Y.; Kunieda, H. *J. Phys. Chem. B* **2006**, 110, 754-760.
- [2.14] (a) Funasaki, N. In *Mixed surfactant systems*, **1993**, ed. K. Ogino, M. Abe, Surfactant Science Series 46; Dekker: New York, chap. 5, pp 145-188. (b) Barthélémy, P.; Tomao, V.; Selb, J.; Chaudier, Y.; Pucci, B. *Langmuir* **2002**, 18, 2557-2563.
- [2.15] (a) Meguro, K.; Muto, Y.; Sakurai, F.; Esumi, K. In *Phenomena in mixed surfactant systems*, **1986**, ed. J. F. Scamehorn, ACS Symposium Series 311; American Chemical Society: Washington, DC, chap. 4, pp 61-67. (b) Villeneuve, M.; Nomura, T.; Matsuki, H.; Kaneshina, S.; Aratono M. *J. Colloid Interface Sci.* **2001**, 234, 127-136.
- [2.16] Shinoda, K. *J. Phys. Chem.* **1954**, 58, 541-544.
- [2.17] Clint, J. H. *J. Chem. Soc., Faraday Trans. 1* **1975**, 71, 1327-1334.
- [2.18] Rubingh, D. N. In *Solution Chemistry of Surfactants*, Vol. 1, **1979**, ed. K. L. Mittal, Plenum: New York, pp 354.
- [2.19] Rosen, M. J.; Hua, X. Y. *J. Colloid Interface Sci.* **1982**, 90, 212-219.
- [2.20] (a) Nagarajan, R. *Langmuir* **1985**, 1, 331-341. (b) Hall, D. G.; Huddleston, R. W. *Colloids Surf.* **1985**, 13, 209-219.
- [2.21] (a) Rubingh, D. N. in *Solution Chemistry of Surfactants*, Vol. 1, **1979**, 1st ed., ed. K. L. Mittal, Plenum, New York, pp 337-354. (b) Rosen, M. J.; Hua, X. Y. *J. Colloid Interface Sci.*

- 1982**, 86, 164-172. (c) Hines, J. D.; Thomas, R. K.; Garrett, P. R.; Rennie, G. K.; Penfold J. J. *Phys. Chem. B* **1997**, 101, 9215-9223. (d) Zhou, Q.; Rosen, M. J. *Langmuir* **2003**, 19, 4555-4562.
- [2.22] Gu, Ben; Rosen, M. J. *J. Colloid Interface Sci.* **1989**, 129, 537-553.
- [2.23] Gibbs, J. W., The Collected Works of J. W. Gibbs, Vol. 1, **1928** Longmans, Green, London, pp. 119.
- [2.24] (a) Law, J. P.; Kunze, G. W. *Soil Sci. Soc. Am. Proc.* **1966**, 30, 321-327. (b) Wakamatsu, T.; D.W. Fuerstenau, In *Adsorption from Aqueous Solution*, 1968, ed. W. J. Weber, and E. Matijevic, American Chemical Society, Washington, DC, pp. 161-172. (c) Rupprecht, H.; Liebl, H. *Kolloid Z. Z. Polym.* **1972**, 250, 719-723.
- [2.25] (a) Doren, A.; Vargas, D.; Goldfrab, J. *Inst. Min. Metall. Trans., Sect. C* **1975**, 84, 34-39. (b) Somasundaran, P.; Snell, E. D.; Xu, Q. *J. Colloid Interface Sci.* **1991**, 144, 165-173. (c) Zhang, L.; Somasundaran, P.; Maltesh, C., *J. Colloid Interface Sci.* **1997**, 191, 202-208.
- [2.26] Snyder, L. R. *J. Phys. Chem.* **1968**, 72, 489-494.
- [2.27] (a) Kölbel, H.; Hörig, K. *Angew. Chem.* **1959**, 71, 691-697. (b) Kölbel, H.; Kuhn, P. *Angew. Chem.* **1959**, 71, 211-215.
- [2.28] Dick, S. G.; Fuerstenau, D. W.; Healy, T. W. *J. Colloid Interface Sci.* **1971**, 37, 595-602.
- [2.29] Findenegg, G. H. in *Theoretical Advancement in Chromatography and related Separation Techniques*, **1992**, ed. F. Dondi, G. Guiochon (Hrsg.), Kluwer Academic Publishers, Dordrecht,.
- [2.30] Langmuir I. *J Am Chem Soc* **1918**, 40, 1361-1403.
- [2.31] Cases, J. M.; Mutaftschiev, B. *Surf. Sci.* **1968**, 9, 57-72.
- [2.32] Harwell, J. H.; Hoskins, J. C.; Schechter, R. S.; Wade, W. H. *Langmuir* **1985**, 1, 251-262.
- [2.33] (a) Łajtat, L.; Narkiewicz-Michalek, J.; Rudziński, W.; Partyka, S. *Langmuir* **1993**, 9, 3174-3190; (b) Łajtat, L.; Narkiewicz-Michalek, J.; Rudziński, W.; Partyka, S. *Langmuir* **1994**, 10, 3754-3764.
- [2.34] Somasundaran, P.; Fuerstenau, D.W. *J. Phys. Chem.* **1966**, 70, 90-96.
- [2.35] Johnson, R.A.; Nagarajan R. *Colloids Surf, A Physicochem. Eng. Asp.* **2000**, 167, 21-30.
- [2.36] Levitz P. *Langmuir* **1991**, 7, 1595-1608.
- [2.37] (a) Scheutjens, J.M.H.M.; Fleer G.J. *J. Phys. Chem.* **1979**, 83, 1619-1635. (b) Böhmer, M.R.; Koopal, L.K. *Langmuir* **1992**, 8, 1594-1602. (c) Koopal, L.K.; Lee, M. L.; Böhmer, M.R. *J. Colloid Interface Sci.* **1995**, 170, 85-97.
- [2.38] (a) Gu, T; Zhu, B.-Y. *J. Chem. Soc., Faraday Trans. I* **1989**, 85, 3813-3817. (b) Gu, T; Zhu, B.-Y. *Colloids and Surfaces* **1990**, 44, 81-87.
- [2.39] (a) Zhu, B.-Y.; Gu, T.; Zhao, X., *J. Chem. Soc., Faraday Trans. I* **1989**, 85, 3819-3824. (b) Findenegg, G.H.; Eltekov, A.Y. *J. of Chromatography A* **2007**, 1150, 236-240. (c) Lugo, D.; Oberdisse, J.; Karg, M.; Schweins, R.; Findenegg, G.H. *Soft Matter* **2009**, 5, 2928-2936.
- [2.40] Kunjappu, J.T.; Somasundaran P. *Colloids Surf* **1989**, 38, 305-311.

- [2.41] (a) Manne, S.; Gaub, H.E. *Science*, **1995**, 270, 1480-1482. (b) Grant, L. M.; Tiberg, F.; Ducker, W. A., *J. Phys. Chem. B*, **1998**, 102, 4288-4294. (c) Warr, G. G. *Current Opin. Colloid Interface Sci.* **2000**, 5, 88-94. (d) Dong, J.; Mao, G., *Langmuir*, **2000**, 16, 6641-6647.
- [2.42] (a) Tiberg, F.; Jönsson, B.; Tang, J.; Lindman, B. *Langmuir* **1994**, 10, 2294-2300. (b) Tiberg, F. *J. Chem. Soc., Faraday Trans. II* **1996**, 92, 531-538.
- [2.43] (a) Cummins, P. G.; Staples, E.; Penfold, J., *J. Phys. Chem.* **1990**, 94, 3740-3745. (b) Cummins, P. G.; Penfold, J.; Staples, E., *J. Phys. Chem.* **1992**, 96, 8092-8094. (c) Penfold, J.; Staples, E.; Tucker, I.; Cummins, P. G. *J. Phys. Chem.* **1996**, 100, 18133-18137. (d) Grillo, I.; Levitz, P.; Zemb, T. *Eur. Phys. J. B* **1999**, 10, 29-34.
- [2.44] Thirtle, P.N.; Li, Z.X.; Thomas, R. K.; Rennie A. R.; Satija, S. K.; Sung, L. P. *Langmuir* **1997**, 13, 5451-5458.
- [2.45] Schulz, J. C.; Warr, G. G.; Hamilton, W. A.; Butler, P. D. *J. Phys Chem, B* **1999**, 103, 11057-11063.
- [2.46] (a) Despert, G.; Oberdisse, J. *Langmuir* **2003**, 19, 7604-7610. (b) Oberdisse, J. *Phys. Chem. Chem. Phys.* **2004**, 6, 1557-1561.
- [2.47] Bäverbäck, P. Ph.D Thesis **2009**, chap. 1, pp. 1-22.
- [2.48] Spalla, O. in *Neutrons, X-rays and Light: Scattering Methods Applied to Soft Condensed Matter* **2002**, 1st ed., ed. P. Lindner and Th. Zemb, Elsevier, Boston, chap. 3, pp. 49-71.
- [2.49] Williams, C. E.; May, R. P.; Guinier, A., in *X-ray Characterization of Materials* **1999**, 1st ed., ed. E. Lifshin, Wiley-VCH, NY, chap. 4, pp. 213-251.
- [2.50] Karg, M. Ph.D Thesis **2009**, chap. 2, pp. 7-30.
- [2.51] Berne, B.J.; Pecora, R., *Dynamic Light Scattering* **1976**, 1st ed., John Wiley & Sons, Inc., NY, chap. 2, pp. 10-23.
- [2.52] Koppel, D.E. *J. Chem Phys.* **1972**, 57, 4814-4820.
- [2.53] (a) Provencher, S. W. *Comput. Phys. Commun.* **1982**, 27, 213-227. (b) Provencher, S. W. *Comput. Phys. Commun.* **1982**, 27, 229-242.
- [2.54] <http://www.ill.eu/instruments-support/instruments-groups/instruments/d11/>
- [2.55] King, S. M.; Griffiths, P. C.; Cosgrove, T., in *Applications of Neutron Scattering to Soft Condensed Matter, Matter* **2000**, 1st ed., ed. B. J. Gabrys, Gordon and Breach Science Publishers, Netherlands, chap. 4, pp. 77-105.
- [2.56] Sears, V.F. *Neutron News*, **1992**, 3, 29-37.
- [2.57] Pusey, N. P. in *Neutrons, X-rays and Light: Scattering Methods Applied to Soft Condensed Matter* **2002**, 1st ed., ed. P. Lindner and Th. Zemb, Elsevier, Boston, chap. 1, pp. 3-21.
- [2.58] Oberdisse, J.; Pyckhout-Hintzen, W.; Straube, E. in *Recent Advances in Polymer Nanocomposites* **2009**, 1st ed., ed. Thomas, G.E. Zaikov and S.V. Valsaraj VSP Publications, chap. 12, pp. 397-438.

- [2.59] Kohlbrecher, J., User Guide for the SASfit software package, Paul Scherrer Institute, Laboratory for neutron scattering, **2009** Edition. Available as pdf (SASfit.pdf) from <http://sans.web.psi.ch/SANSSoft/sasfit.pdf>
- [2.60] Kholodenko, A. L. *Macromolecules* **1993**, *26*, 4179-4183.
- [2.61] D'Aguanno, B.; Klein, R. *J. Chem. Soc. Faraday Trans.* **1991**, *87*, 379-390.
- [2.62] Oberdisse, J.; Hine, P.; Pyckhout-Hintzen, W. *Soft Matter* **2007**, *3*, 476-485.
- [2.63] Hansen, J.P.; McDonald I.R. In *Theory of Simple Liquids* **2006**, *3rd ed.*, Academic Press, London.
- [2.64] Percus, J.K.; Yevick, G.J. *Phys. Rev.* **1958**, *110*, 1-13.
- [2.65] (a) Hayter, J.B.; Penfold, J. *Mol. Phys.* **1981**, *42*, 109-118. (b) Hansen, J.P.; Hayter, J.B. *Mol. Phys.* **1982**, *46*, 651-656.

3 Experimental Section

3.1 Chemicals

The surfactants penta(ethylene glycol) monododecyl ether, $C_{12}E_5$ (Fluka, purity $\geq 98\%$, density 0.963 g cm^{-3} at 293 K), decyl- β -maltoside, β - $C_{10}G_2$ (Glycon, purity $> 99.5\%$, density 1 g cm^{-3}), dodecyl- β -maltoside, β - $C_{12}G_2$ (Glycon, purity $> 99.5\%$, density 1 g cm^{-3}) and *N,N*-dimethyldodecylamine-*N*-oxide, $C_{12}DAO$ (Fluka, purity $\geq 98\%$) and the chemicals tetraethyl orthosilicate, TEOS (Fluka, purity $\geq 99.0\%$), ammonia (Sigma-Aldrich, A.C.S. reagent, 30-33% in water), ethanol, C_2H_5OH (Berkel AHK, purity $\geq 99.9\%$), and D_2O (Euriso-top, 99.9% isotope purity), were used without further purification. Reagent-grade water was produced by a Milli-Q 50 filtration system (Millipore, Billerica, USA) reaching a resistance of $18.2 \text{ M}\Omega$, and was additionally passed through a $0.22 \text{ }\mu\text{m}$ membrane to remove micrometer-sized particles. Commercial colloidal silica suspensions, Ludox SM-30 (30 wt-% in water) and Ludox HS-40 (40 wt-% in water) were supplied by Sigma-Aldrich. They were dialyzed with reagent-grade water (2 weeks) and filtered with a $0.8 \text{ }\mu\text{m}$ Millipore Steril Filter. The silica concentration in the purified suspensions was about one half of the original concentration. The pH was adjusted to 9 by the addition of 0.1 M NaOH in order to preserve colloidal stability. The colloidal dispersions were stored in a refrigerator at 280 K before use.

3.2 Sample Preparation

3.2.1 Synthesis of silica nanoparticles

Three samples of monodisperse silica nanoparticles were prepared by two variants of the Stöber synthesis [3.1]. The preparation of the nanoparticles of smaller size, denoted as silica I (diameter 16 nm) and silica II (27 nm), was made by particle growth from Ludox SM-30 and Ludox HS-40 dispersions, respectively. First a selective growth of Ludox particles was performed in basic conditions using TEOS as the silica source. 12.0 mL of the Ludox stock dispersion was added to a mixture of 240 mL ethanol, 60 mL water and 15.2 mL ammonia (30-33% in water) and was stirred in a PE bottle. 102 μL of TEOS

were then added and stirring was continued for 24 h. After this growth step the Ludox particles had increased in size while the polydispersity had decreased. Particle growth was monitored by dynamic light scattering (DLS) and transmission electron microscopy (TEM). To reach the desired particle diameter the overgrown Ludox particles were dialyzed against Milli-Q water for 1 week with daily change of the reagent-grade water. After dialysis the dispersion was concentrated by a factor 6 by solvent evaporation, using a rotary evaporator (313 K, 160 mbar), then filtered with a Millipore Steril Filter (0.8 μm), and the pH was adjusted to pH 9. The samples were stored in a refrigerator at 280 K before use.

Silica III (diameter 42 nm) was prepared by the classical Stöber synthesis [3.1], *i.e.* by condensation of TEOS, starting from a mixture of 100 mL ethanol and 7.5 mL ammonia at 333 K in a 250 mL three-neck round flask equipped with a magnetic stirrer and reflux-condenser. After 30 min of equilibration time, 3.0 mL TEOS was added dropwise into the solution under stirring with 100 RPM. The colorless and clear solution became turbid within the first 10 min after the addition of the silica precursor TEOS indicating nucleation. In this step of nucleation the stirrer speed was decreased to 50 RPM. The condensation reaction was allowed to continue for 24 h at 313 K. Afterwards, the colloidal dispersion was cooled down to room temperature and the excess of ethanol and ammonia was removed from the resulting suspension in a rotary evaporator (313 K, 160 mbar) by reducing the volume to 20% of the initial value. The suspension was dialyzed with reagent-grade water for 1 week, filtered and stored at pH 9 in a refrigerator at 280 K.

The density and concentration of the resulting dispersions was determined gravimetrically.

3.2.2 Characterization of the silica nanoparticles

The synthesized silica nanoparticles were characterized by several methods as will be described in detail in section 3.3. The silica dispersions obtained after dialysis were diluted to 1 vol.% - 2 vol.% for the characterization by nitrogen adsorption, transmission electron microscopy (TEM), dynamic light scattering

(DLS), zeta potential, and small angle neutron scattering (SANS). For the first three methods the dilution was made using reagent-grade water. In the case of the SANS measurements heavy water (D_2O) was used in order to achieve a high scattering contrast. All samples were diluted and their pH was adjusted to 9 in order to minimize complications by particle aggregation and interaction.

3.2.3 Surfactant solutions

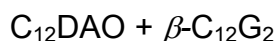
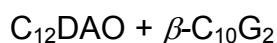
Properties of aqueous solutions of pure surfactants and binary mixtures of surfactants were studied to complement the structural studies of adsorbed surfactant layers on the silica nanoparticles. The following properties were determined:

- (i) Surface tension of binary mixtures was used to determine the *CMC* as a function of the surfactant composition.
- (ii) SANS was used to characterize the size and shape of mixed micelles of pure surfactants and surfactant mixtures.
- (iii) The adsorption isotherms of surfactants on the silica particles was determined by the solution depletion method, using surface tension measurements to determine the surfactant concentration in the supernatant solution.

Below specific information is given for the samples preparation of the binary systems.

Mixtures of amineoxide and maltoside surfactants

The surfactant systems



were studied in order to assess the effect of the tail length of β -alkylmaltoside and thus their *CMC* on the mixed micelles formed with dodecyldimethyl amine oxide. Surface tension measurements were used to determine the *CMC* as a function of the surfactant composition. Stock solutions with the binary surfactant mixture were prepared by adding 25, 50 and 75 weight-% of $\beta\text{-}C_{10}G_2$ or of $\beta\text{-}C_{12}G_2$ to a 2 vol.-% stock solution of $C_{12}DAO$. Samples for the surface tension

measurements were made by dilution of the stock solution of C₁₂DAO and of the stock solution of each surfactant mixture over a range concentration from $C/CMC = 0.003$ to 4. Solutions were prepared in H₂O at pH 9, and equilibrated overnight using a GFL 3025 test tube rotator, before the measurements ($CMC = 2 \times 10^{-3}$ M).

Samples for SANS measurements were prepared in two different solvent contrasts: in pure D₂O (scattering length density $\rho_D = 6.34 \times 10^{10} \text{ cm}^{-2}$) and in a H₂O/D₂O mixture ($\rho_{HD} = 3.54 \times 10^{10} \text{ cm}^{-2}$); the latter of these corresponds to the contrast-matching point of the silica nanoparticles (determined experimentally). 1 vol.-% solutions of each binary system (C₁₂DAO: β -C₁₀G₂ and C₁₂DAO: β -C₁₂G₂) at five different mass ratios (1:0; 3:1; 1:1; 1:3; 0:1) were prepared by dilution of stock solutions of 5 vol.-%. These measurements were made in order to study the size and shape of the mixed micelles in these systems.

3.2.4 Surfactant adsorption on the silica nanoparticles

The adsorption isotherm of surfactants on silica nanoparticles was determined by the solution depletion method, using surface tension measurements to determine the surfactant concentration in the equilibrated systems. Samples were prepared with a low concentration silica sol (1-2 vol.-%) at pH 9. Silica dispersions in normal water were used in surface tension and DLS measurements to study the adsorption of C₁₂E₅ on the silica nanoparticles of 16 nm of particle size. Samples with seven different concentrations of C₁₂E₅ in a C/CMC range from 0.7 to 2.6 were prepared and equilibrated overnight before the measurements ($CMC = 6 \times 10^{-5}$ M, cf. section 4.2.2). SANS measurements were made with silica sols in a H₂O/D₂O mixture of a scattering length density (SLD) which matches that of silica, so that the scattering contrast arises only from the surfactant. It was found that the match point is attained at a SLD $\rho = 3.54 \times 10^{10} \text{ cm}^{-2}$. Samples of the colloidal sol with different surfactant concentrations were prepared by adding appropriate amounts of the surfactant directly to the aqueous dispersion. For C₁₂E₅, samples with four different surface concentrations of the surfactant, corresponding to $\frac{1}{4}\Gamma_{mx}$, $\frac{1}{2}\Gamma_{mx}$, $\frac{3}{4}\Gamma_{mx}$ and Γ_{mx} were prepared, where Γ_{mx} is the plateau value of the surfactant

adsorption isotherm as determined by the surface tension measurements (cf. section 4.2.2) [3.2]. For the surfactants β -C₁₀G₂ and β -C₁₂G₂, two samples corresponding to $\frac{3}{4}\Gamma_{\text{mx}}$ and Γ_{mx} were prepared in an analogous manner.

In the study of the self-assembly of C₁₂DAO on silica beads, dilute silica dispersions (0.4 to 1.5 vol.-%) of three different particle sizes (16 nm, 27 nm, 42 nm) in the contrast-matching H₂O/D₂O solvent mixture at pH 9 were prepared for the SANS measurements. Samples with different adsorbed amounts of C₁₂DAO ($\frac{1}{4}\Gamma_{\text{mx}}$, $\frac{1}{2}\Gamma_{\text{mx}}$, $\frac{3}{4}\Gamma_{\text{mx}}$ and $\frac{7}{8}\Gamma_{\text{mx}}$) were prepared. The adsorption isotherm of C₁₂DAO on Davisil silica gel reported by Pettersson and Rosenholm [3.3] was used to estimate the amounts of surfactant needed for a given surface concentration on the silica particles. According to that work, a plateau value $\Gamma_{\text{mx}} = 7.5 \mu\text{mol m}^{-2}$ is reached at a solution concentrations somewhat above the CMC ($\sim 2 \times 10^{-3}$ M), and the surface concentration at the CMC is about $\frac{7}{8}\Gamma_{\text{mx}}$. This value was chosen as the highest surface concentration of the surfactant on the silica particles, to avoid free micelles in the solution.

3.2.5 Adsorption from surfactant mixtures on the Silica Nanoparticles

The adsorption from mixtures of two nonionic surfactants onto silica sol was studied in order to clarify the nature of mixed surfactant aggregates formed on the silica nanoparticles. Specifically, it was aimed to study the regime in which the amount of the preferred surfactant is not sufficient to cover the silica particles with a complete adsorbed bilayer. The preparation of these mixed surfactant systems is described below.

Mixtures of amine-oxide surfactants and maltoside surfactants

In this series of experiments, C₁₂DAO was used as the strongly adsorbed surfactant (component A), and β -C₁₀G₂ or β -C₁₂G₂ as the weakly adsorbed surfactant (component B). Samples with a low concentration of silica sol (1.5 vol.-%; silica size 24 nm) were prepared in a H₂O/D₂O mixture of scattering length density $\rho_{\text{HD}} = 3.54 \times 10^{10} \text{ cm}^{-2}$, which matches the silica particles, and at pH 9 to avoid congruent dissolution of particles and to minimize complications

by particle interaction and aggregation. For both binary systems ($C_{12}DAO:\beta-C_{10}G_2$ and $C_{12}DAO:\beta-C_{12}G_2$) 1:1 mixtures of the surfactants were prepared for four surface concentrations of $C_{12}DAO$, based on the adsorption values: $\frac{1}{4}\Gamma_{mx}$, $\frac{3}{4}\Gamma_{mx}$, $\frac{7}{8}\Gamma_{mx}$, and Γ_{mx} (at a $C \gg CMC$) of $C_{12}DAO$, where Γ_{mx} is again the plateau value of the adsorption isotherm of surfactant on silica [3.3]. Additionally, an overall concentration of 1 vol.-% of the mixture at three different mass ratios (3:1; 1:1; 1:3) was tested to see the effect of large surfactant excess. And finally, to test the effect of the surfactant composition on the adsorption, a stock solution of $\frac{1}{2}\Gamma_{mx}$ of $C_{12}DAO$ was prepared and different amounts of the maltoside surfactant were added to 1.5 mL of the stock solution in silica sol to prepare binary mixtures with the following mass ratios: 1:0.07; 1:0.33; 1:1; 1:3). Most of the samples were prepared not only in contrast matching H_2O/D_2O but also in nearly pure D_2O which gives a high contrast and low background.

3.3 Methods

3.3.1 Nitrogen Adsorption

The synthesized silica nanoparticles were characterized by nitrogen adsorption in order to obtain their specific surface area from the nitrogen adsorption isotherm according to the BET (Brunauer, Emmett and Teller) theory [3.4], as is shown in Figure 3.1. The specific surface area a_s can be calculated from the amount of gas adsorbed in a monolayer, which is often expressed in by the ideal gas volume V_m under standard conditions (STP) in gas-volumetric measurements:

$$a_s = V_m \cdot \sigma_{N_2} \cdot N_A \quad (3.1)$$

Here σ_{N_2} is the cross-sectional area of one adsorbed nitrogen molecule ($\sigma_{N_2} = 0.162 \text{ nm}^2$) [3.5] and N_A is the Avogadro constant. V_m is obtained from the linearization of the empirical BET equation in the range of relative pressures from 0.05 to 0.3:

$$\frac{p/p_0}{V_{ads}(1-p/p_0)} = \frac{1}{V_m \cdot C_{BET}} + \frac{C_{BET} - 1}{C_{BET} \cdot V_m} \cdot p/p_0 \quad (3.2)$$

where C_{BET} is the scalar BET constant which characterizes the strength of the interaction between the gas molecules and the solid surface. Large values of C_{BET} ($C_{BET} > 100$) indicate relatively strong adsorption energy of molecules in the first adsorption layer with regard to the condensation energy of the adsorptive.

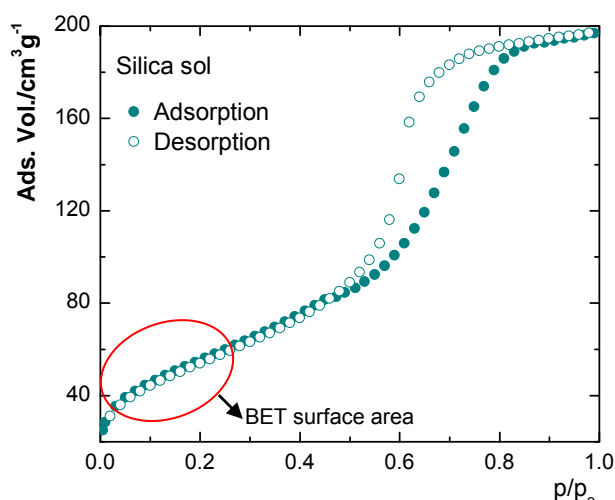


Figure 3.1. Schematic representation of the typical analysis of nitrogen adsorption isotherm for the synthesized silica nanoparticles ($R = 8.2$ nm).

Adsorption isotherms of nitrogen at 77 K were measured by gas volumetry using a Micromeritics Gemini III 2375 Volumetric Surface Analyzer. Before the gas adsorption measurements, the silica dispersions were dried at 218 K for two days using a Freeze Dryer Alpha 2–4 LD/plus (Martin Christ), and then outgassed at 393 K for 1 h under vacuum, and finally, reweighed to determine the net mass of the sample. For the measurements the standard Micromeritics sample tubes were used. For better thermal isolation of the Dewar vessel in which the sample tube is immersed in liquid nitrogen, the original top of the Dewar vessel is replaced by a styrofoam top. In this way it was guaranteed that evaporation of the nitrogen was slow enough to maintain the temperature of the sample constant for the full time of 6 h measurement.

3.3.2 Transmission Electron Microscopy (TEM)

TEM measurements were made at ZELMI at TU Berlin to determine the morphology and size of the silica nanoparticles. TEM images were taken using a Tecnai G² 20 S-Twin electronic microscope operating at an accelerating voltage of 200 kV and an electron source of LaB₆. Samples for TEM were first diluted to a volume fraction less than 1 vol.-% and then prepared by drying a droplet of the dilute dispersion on a copper grid (coated with a carbon film with a thickness of 20 nm). TEM images were taken at a minimum of 5 different locations on the grid, and a total of 220 particles were measured per sample to ensure good statistics in the determination of the particles size.

3.3.3 Zeta Potential

In order to obtain information about the surface charge of the particles zeta potential measurements were carried out with a Malvern Zeta-Sizer 2000 using dilute silica particle dispersions at pH 9 and 298 K.

3.3.4 Dynamic Light Scattering (DLS)

Light scattering experiments were performed to determine the hydrodynamic radius R_H of the silica nanoparticles, and to estimate the layer thickness of adsorbed surfactant on the silica nanoparticles from the difference in R_H of the silica particles in presence and in absence of the surfactant. Dilute silica dispersions (~2 vol.-%) were used for DLS measurements in order to avoid multiple scattering events. The samples were filled in cylindrical quartz cells of 10 mm in diameter (Hellma, Germany). The cells were carefully cleaned and afterwards rinsed with freshly distilled acetone to remove dust particles.

The setup for the DLS instrument used in this work is shown in subsection 2.4.1 (Figure 2.10). The laser is a frequency doubled Nd:YAG-Laser (Compass 150, Coherent, USA) with a wavelength $\lambda = 532$ nm operating in cw mode and providing a constant output power of 150 mW. All particle size measurements were performed at 298 K (temperature controlled by a thermostatted toluene matching bath) and at different scattering angles between 45° and 135°. Correlation functions were generated using an ALV-5000/E multiple τ digital

autocorrelator. The recorded correlation functions were analysed by inverse Laplace transformation with the FORTRAN program CONTIN [3.6]. Sizes reported in this study represent the average of 3–5 measurements. No corrections for the presence of micelles above the *CMC* were made. The viscosity of pure water was used in the calculation of R_H .

3.3.5 Surface Tension

Static surface tension measurements of surfactant solutions were made at 278.3 ± 0.2 K by the Du Noüy ring method [3.7], using a Krüss K11 tensiometer. Prior to the measurements of surfactant solutions, repeated measurements of the surface tension of pure water were made to ensure accuracy and reproducibility of the apparatus. The sample vessels (diameter ~ 30 mm) which hold the solution under study were cleaned by soaking them in Milli-Q grade water overnight, then rinsed and cleaned with acetone and again with Milli-Q grade water. The platinum ring was flame-cleaned prior to use and when the surfactant solution was changed. The prepared samples (*cf.* sections 3.2.3 and 3.2.4) were thermostated in the apparatus for at least 30 min before measurement.

The adsorption isotherm of $C_{12}E_5$ on the silica sol particles was determined by measuring the surfactant depletion in the supernatant solution after removal of the silica by centrifugation (4 h at 8500 rpm in a Universal 320R centrifuge). The equilibrium concentration in the supernatant was determined from its surface tension, using the γ -log(*C*) curve of aqueous solutions of $C_{12}E_5$ as a calibration curve.

3.3.6 Small Angle Neutron Scattering

SANS experiments were performed on instrument D11 of the Institut Laue-Langevin (Grenoble, France), on instrument PAXY of the Laboratoire Léon Brillouin (CEA de Saclay, France), and on instrument V4 of the Helmholtz Zentrum Berlin für Materialien und Energie GmbH (Berlin, Germany).

The setup of all instruments is represented by the scheme illustrated in Figure 2.12 (subsection 2.4.2). In most cases SANS measurements were

performed covering a range of the scattering vector q from 0.03 to 3 nm⁻¹. The samples were contained in standard 2-mm path length quartz cells (QS, Hellma), thermostated to 298 ± 0.1 K. Corrections were made for instrumental background, electronic noise, transmission, and empty cell.

Data reduction from the D11 instrument was done with the ILL standard software package according to ref. 3.8 and 3.9. Data treatment from the PAXY instrument was made using the software provided by LLB [3.10] and the data recorded from V4 instrument were treated by using the software package BerSANS [3.11].

References of Chapter 3

- [3.1] Stöber, W.; Fink, A.; Bohn, E. *J. Colloid Interface Sci.* **1968**, *26*, 62-69.
- [3.2] Lugo, D.; Oberdisse, J.; Karg, M.; Schweins, R.; Findenegg, G.H. *Soft Matter* **2009**, *5*, 2928–2936.
- [3.3] Pettersson, A.; Rosenholm, J. B. *Langmuir* **2002**, *18*, 8436-8446.
- [3.4] Brunauer, S.; Emmett, P. H.; Teller, E. *J. Am. Chem. Soc.*, 1938, **60**, 309-319.
- [3.5] Ismail, M. K. I. *Langmuir* **1992**, *8*, 360–365.
- [3.6] (a) Provencher, S. W. *Comput. Phys. Commun.*, 1982, **27**, 213-227. (b) Provencher, S. W. *Comput. Phys. Commun.*, 1982, **27**, 229-242.
- [3.7] Du Noüy, P. L. *J. Gen. Physiol.* **1919**, *1*, 521.
- [3.8] Ghosh, R. E.; Egelhaaf S. U.; Rennie, A. R. *A Computing Guide for Small-Angle Scattering Experiments*, ILL Report ILL06GH05T, 2006 Edition. Available as pdf (sans_manual.pdf); from ftp://ftp.ill.fr/pub/cs/sans/sans_manual.pdf
- [3.9] Lindner, P. in *Neutrons, X-rays and Light: Scattering Methods Applied to Soft Condensed Matter*, ed. P. Lindner and Th. Zemb, Elsevier, Boston, 1st edn., 2002, ch. 2, pp. 23-48.
- [3.10] Brûlet, A.; Lairez, D.; Lapp, A.; Cotton, J.-P. *J. Appl. Cryst.* **2007**, *40*, 165-177.
- [3.11] (a) Keiderling, U. *Physica B* **1997**, *234*, 1111-1113. (b) Keiderling, U. *Appl. Phys. A* **2002**, *74*, 1455-1457.

4 Surface Aggregate Structure of Nonionic Surfactants on Colloidal Silica Nanoparticles*

4.1 Introduction

The adsorption of nonionic surfactants at solid surfaces is of interest because of its importance to a great number of industrial and technological processes associated with colloidal stability and detergency. Adsorption of surfactants from aqueous solutions onto flat surfaces [4.1-4.5], colloidal silica [4.2, 4.6-4.8] and in porous silica [4.9-4.12] has been studied extensively in the past in view of its practical importance and rich bulk and interfacial behavior. A common point emerging from these studies is that adsorption at hydrophilic silica surfaces represents a surface aggregation process similar to micelle formation in the bulk solution. Surface aggregation may lead to discrete surface micelles or to fragmented or complete bilayers, depending on the surfactant composition and relative sizes of the head groups and the tails of the surfactant. However, information about the interfacial aggregation of surfactant molecules is still limited and it is not yet well understood.

Structural information about adsorbed surfactant layers at the interface of the aqueous phase against flat solid surfaces has been gained mainly by neutron reflectometry (NR) [4.1, 4.2, 4.4] and atomic force microscopy (AFM) [4.13-4.17]. Direct evidence about surface aggregate structures of amphiphiles at flat solid surfaces has been gained by non-contact AFM. Specifically, it has become clear that many of the aggregate geometries which exist in bulk solution may also develop at the solid/solution interface, depending on the hydrophilic or hydrophobic nature of the surface [4.17]. These findings are consistent with calorimetric studies which show that at hydrophilic surfaces the enthalpy of adsorption of nonionic surfactants in the

*modified from published article in Soft Matter: Lugo, D.; Oberdisse, J.; Karg, M.; Schweins, R.; Findenegg, G.H. *Soft Matter* **2009**, 5, 2928–2936.

surface-aggregation regime is of similar magnitude as the enthalpy of micelle formation in the bulk solution [4.18]. NR yields the scattering-length density profile $\rho(z)$ which comprises information about the laterally averaged structure of the surfactant layer. In favourable cases, when using partially deuterated surfactants and different contrast scenarios, information about the arrangement of the amphiphile molecules in complete (saturated) mono- or bilayer can be obtained by this method. An attempt to model NR data of adsorbed surfactant films based on the existence of discrete surfactant aggregates of well-defined geometry was presented by Schulz et al. [4.19] As a more direct approach to resolve laterally structured surfactant layers by a non-invasive technique, Steitz et al. [4.20] used grazing-incidence small-angle neutron scattering (GISANS) to study surfactant films at a hydrophilic silicon wafer in the regime below saturation coverage. In that study the mean surface concentration of the chosen nonionic surfactant could be varied over a wide range simply by varying the sample temperature at a constant bulk concentration somewhat below the CMC. The GISANS results indicated the existence of transient surfactant aggregates without a preferred structure at half-coverage of the surface, indicating that the picture of distinct surface aggregates of characteristic size and separation that emerges from AFM studies of saturated surfactant layers cannot be generalized to the situation below complete surface coverage.

Small-angle neutron scattering (SANS) [4.6, 4.8] and fluorescent probe techniques [4.9] have been used to characterize the nature of surfactant layers adsorbed at particulate and colloidal solids in aqueous dispersions. In their pioneering SANS work Cummins et al. [4.6] studied alkyl polyoxyethylene ether (C_nE_m) surfactants on Ludox HS and TM silica sols and demonstrated the effects of temperature, sol type, surfactant type and surfactant concentration on the adsorption at the colloidal silica particles. The adsorbed layer was modeled as a layer of uniform density, and hence the form factor was that of a sphere plus an outer shell. Later, one of the present authors [4.8, 4.21] analysed SANS data of a technical-grade nonionic surfactant (Triton X-100) on silica nanoparticles on the basis of a

model with a well-defined number of micellar aggregates adsorbed at the silica surface. It was found that this *micelle-decorated silica* model accounts in a quantitative manner for the experimental scattering profiles at maximal surface coverage of the silica beads.

In this chapter we present a SANS study of the structure of adsorbed surfactant layers on colloidal silica over a wide range of surface concentrations of the surfactant. A silica sol of uniform particle diameter of ca. 16 nm was prepared and used to study the adsorption behavior of two different types of nonionic surfactants, *viz.*, alkyl polyoxyethylene ether ($C_{12}E_5$) and alkyl maltoside (β - $C_{12}G_2$). The SANS data are analyzed in terms of the core-shell model and the micelle-decorated silica model.

4.2 Results

4.2.1 Characterization of the silica particles

Electron micrographs show that the silica particles, prepared by Stöber synthesis [4.22] using Ludox SM-30 as the starting material, are approximately spherical in shape (Figure 4.1), with an average particle diameter of about 16 nm. A somewhat larger diameter, 18 nm, was found by DLS.

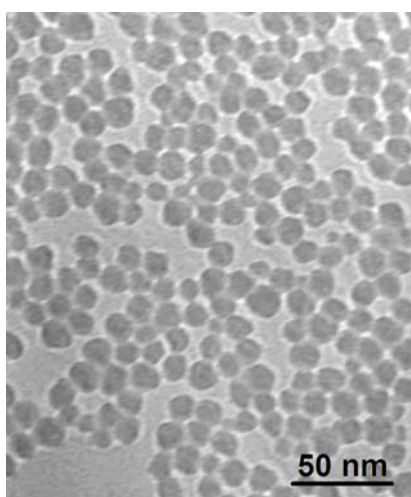


Figure 4.1. Transmission electron micrograph of the silica used in this study.

The aqueous dispersions at pH 9 had a zeta potential of -46 mV and a

conductivity of about $120 \mu\text{S cm}^{-1}$. The high zeta potential indicates a high surface charge of the particles which implies that the silica dispersion is electrically stabilized.

The nitrogen adsorption isotherm of the dried silica was analysed by the BET method in a range of relative pressures p/p_0 from 0.05 to 0.3 (Figure 4.2). A specific surface area $a_s = 205 \text{ m}^2\text{g}^{-1}$ and BET constant $C_{\text{BET}} = 65$ was obtained. The value of a_s is well compatible with the particle radius of 8.2 nm obtained by SANS, which leads to a geometric surface area $a_{\text{geom}} = 168 \text{ m}^2\text{g}^{-1}$. The ratio $a_s/a_{\text{geom}} = 1.2$ can be attributed to surface roughness of the beads and indicates a low porosity of the beads. The features of the nitrogen adsorption isotherm at relative pressures $p/p_0 > 0.5$ (see inset in Fig. 4.2) can be attributed to pore condensation in the voids between close-packed silica beads in the dried sample and are thus of no significance for the present work.

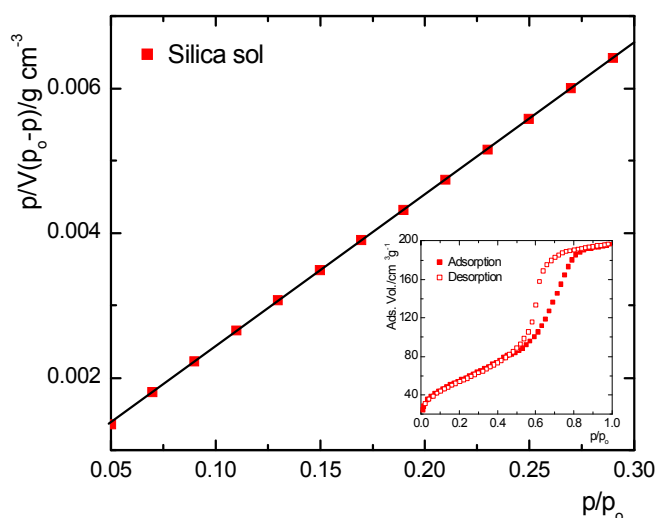


Figure 4.2. BET plot of the nitrogen adsorption on the silica; the full adsorption isotherm is shown in the inset.

The structure and shape of the silica particles was measured in a dilute silica suspension in D_2O -rich water ($\rho_{\text{D}} = 5.17 \times 10^{10} \text{ cm}^{-2}$). The scattering profile $I(q)$, shown in Figure 4.3, exhibits a pronounced oscillation near $q = 0.7 \text{ nm}^{-1}$, indicating a rather uniform size of the silica beads. The peak at $q_0 \approx 0.1 \text{ nm}^{-1}$ indicates repulsive electrostatic interactions between silica particles

and it has been shown that this peak can be reproduced by standard theory [4.8, 4.23]. Since the particle interactions are not of interest in the present context, we have not tried to describe this maximum at low q quantitatively, but we have checked its consistency. Considering that the silica dispersion has a liquid-like structure, this structure peak at $q_0 \approx 0.1 \text{ nm}^{-1}$ can be used to estimate the silica particle radius, R_s , by using a simple cubic lattice model (CLM), based on the conservation of silica volume on a unit cell, with the distance between the particles given by $D = 2\pi/q_0$. Since the volume of each particle can be estimated through $V = \phi D^3$, where ϕ is the volume fraction of the silica beads, R_s can be calculated by using eq. (2.49).

From the position of the peak we find $R_s = 8.1 \text{ nm}$. If we concentrate on the form factor on the right of the $q = 0.7 \text{ nm}^{-1}$ peak, the data can be described as a system of polydisperse spheres with a log-normal size distribution (*cf.* Section 2.3.1.2), with a polydispersity of 10 % and a mean particle radius of 8.2 nm. The relevant parameters of the colloid are summarized in Table 4.1.

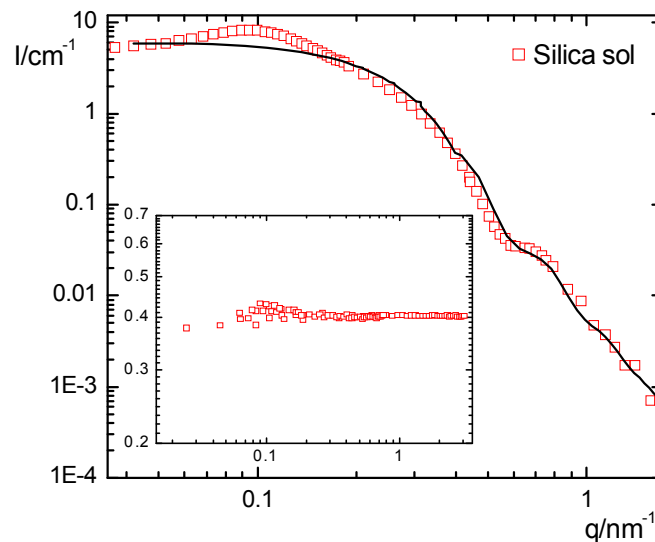


Figure 4.3. Scattering profile for 1.8 wt-% silica dispersion in nearly pure D_2O at pH 9 (298 K). The solid line represents the best fit with the log-normal size distribution function. The inset shows the SANS profile for the dispersion in the contrast-matching $\text{H}_2\text{O}/\text{D}_2\text{O}$ which is used in the scattering experiments in the presence of surfactant.

Table 4.1. Scattering length density ρ , parameters of log-normal size distribution R_s and σ , average radius $\langle R_s \rangle$, average surface area $\langle A_s \rangle$, average volume $\langle V_s \rangle$ of the silica particles.

$(10^{10} \rho \text{ cm}^{-2})$	R_s (nm)	σ	$\langle R_s \rangle$ (nm)	$\langle A_s \rangle$ (nm ²)	$\langle V_s \rangle$ (nm ³)
3.54	8.2	0.10	8.24	$8.62 \cdot 10^2$	$2.42 \cdot 10^3$

4.2.2 Adsorption and film thickness of $C_{12}E_5$ on the silica

The adsorption isotherm of $C_{12}E_5$ on the colloidal silica, shown as curve (A) in Figure 4.4, exhibits a pronounced sigmoidal shape. The surface concentration Γ remains very low up to a concentration C^* at which Γ increases sharply to a plateau value Γ_{mx} . The onset concentration is $C^* = 5 \times 10^{-5}$ M and the plateau value is reached at $C \approx CMC = 6 \times 10^{-5}$ M. The plateau value of the surface concentration, $\Gamma_{mx} = 6 \mu\text{mol m}^{-2}$, corresponds to 5.3×10^{-21} mol $C_{12}E_5$ adsorbed per silica particle. The sharp rise in adsorption prior to the CMC indicates that surface aggregation caused by hydrophobic interactions between surfactant monomers comes into play, as was shown by fluorescence spectroscopy measurements [4.9]. Above the bulk CMC, the surfactant activity remains nearly constant and thus no further adsorption takes place. The shape of the adsorption isotherm is consistent with many literature reports and the plateau value of Γ agrees with the value for $C_{12}E_5$ on silica wafers ($\Gamma_{mx} = 6.0 \mu\text{mol m}^{-2}$) obtained by ellipsometry by Tiberg et al. [4.3] A higher value ($\Gamma_{mx} = 7.5 \mu\text{mol m}^{-2}$) was reported for the adsorption on TK900 silica by Gellan and Rochester [4.24].

The mean thickness δ of the adsorbed layer of $C_{12}E_5$ on the silica beads, shown as curve (B) in Figure 4.4, exhibits the same dependence on the solution concentration as the surface concentration Γ . The plateau value of the film thickness, $\delta_{mx} = 4.6$ nm, is higher than other values for $C_{12}E_5$ on silicon oxide surfaces reported in the literature, viz., 4.2 nm on oxidized silicon wafers obtained by ellipsometry [4.3], 4.4 nm on TK900 silica obtained by X-ray diffraction [4.24], or 4.5 nm on Ludox TM obtained by SANS by Cummins et al. [4.6] The somewhat higher value of δ_{mx} obtained by

DLS in this work may be due to differences in R_H between the bare and surfactant-coated silica particles caused by different hydrodynamic interactions of the two types of surfaces with the aqueous solution.

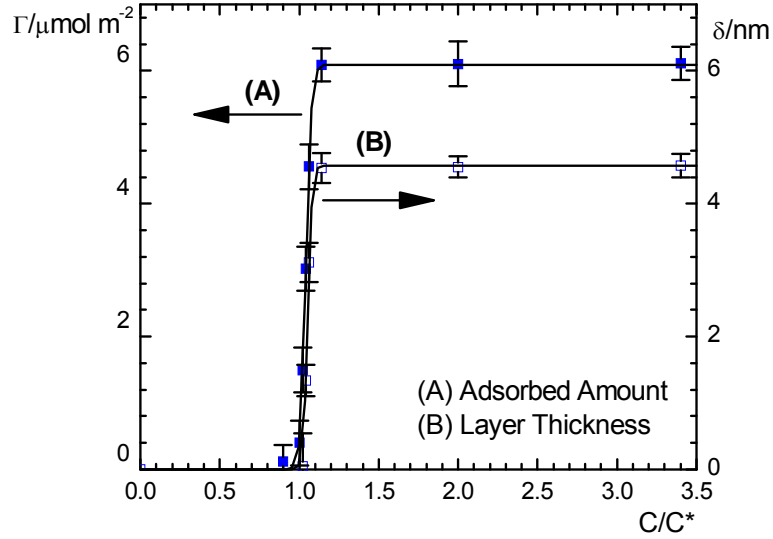


Figure 4.4. Adsorption isotherm of $C_{12}E_5$ on the silica nanoparticles: (A) surface concentration Γ as determined by surface tension measurements of the supernatant; (B) film thickness δ as obtained by dynamic light scattering (see text). The solid lines represent fits by the Gu-Zhu equation.

The data for the surface concentration and film thickness can be represented by the mass action model of one-step formation of surface aggregates proposed by Gu and Zhu, [4.25]

$$Z = \frac{Z_{mx} K (C / C^*)^n}{1 + K (C / C^*)^n} \quad (4.1)$$

where Z is either the surface concentration Γ or the thickness of the adsorbed surfactant layer δ at equilibrium concentration C , Z_{mx} is the limiting values of the surface concentration, Γ_{mx} , or of the adsorbed surfactant layer thickness, δ_{mx} , at high C , C^* is the onset concentration of aggregative adsorption, K is the adsorption constant in the low-affinity region, and n is the average aggregation number of the surface aggregates. Best-fit parameters of eq. (4.1) are given in Table 4.2.

Table 4.2. Parameters of the Gu-Zhu equation (eq. 4.1), for the surface concentration (Γ) and film thickness (δ) isotherms of C₁₂E₅ on the silica sol (298 K, pH 9)

	Γ_{mx} ($\mu\text{mol}/\text{m}^2$)	δ_{∞} (nm)	K	C^* (mol/L)	n
surface concentration	6.1	-	$8.3 \cdot 10^{-2}$	$5 \cdot 10^{-5}$	63
layer thickness	-	4.6	$8.4 \cdot 10^{-2}$	$5 \cdot 10^{-5}$	45

4.2.3 Characterization of the adsorbed layer by SANS

SANS measurements were made to elucidate the structure of the adsorbed layer of the surfactant on the silica particles. A low silica concentration was chosen to suppress the influence of interparticle interactions. The silica concentration in the dispersion was fixed to 1.8 wt-% (0.90 vol.-%) in a H₂O/D₂O mixture that matches the scattering length density of the silica. The contrast-match point was determined experimentally; the quality of contrast-match is illustrated by the inset in Fig. 4.3. Figure 4.5a shows scattering profiles of silica dispersions containing β -C₁₀G₂, β -C₁₂G₂ and C₁₂E₅ under contrast match for the silica particles. In both cases the surfactant concentration was by more than two orders of magnitude higher than the CMC. In the case of C₁₂E₅, the SANS profile exhibits a pronounced oscillation with a maximum at $q = 0.42 \text{ nm}^{-1}$, indicating the existence of a surfactant layer on the surface of the particles [4.6, 4.8]. On the other hand, no such features at intermediate q are observed in the case of β -C₁₀G₂ and β -C₁₂G₂, indicating that these surfactants do not form an adsorbed layer on the surface of the silica particles, in agreement with reports in the literature [4.5]. Instead, β -C₁₀G₂ and β -C₁₂G₂ will form free micelles in solution and one expects that the scattering profile will resemble that of micellar solutions in the absence of silica. Scattering profiles of β -C₁₀G₂, β -C₁₂G₂ and C₁₂E₅ in D₂O are displayed in Figure 4.5b [4.26]. A comparison of Fig. 4.5a and 4.5b shows that the scattering profiles of β -C_nG₂ in the presence and absence of silica are indeed similar. The experimental data for β -C₁₀G₂ and β -C₁₂G₂ in the silica dispersion could be fitted by an oblate ellipsoid core-shell form factor model characterized by an ellipsoid core with rotational semi-axis a

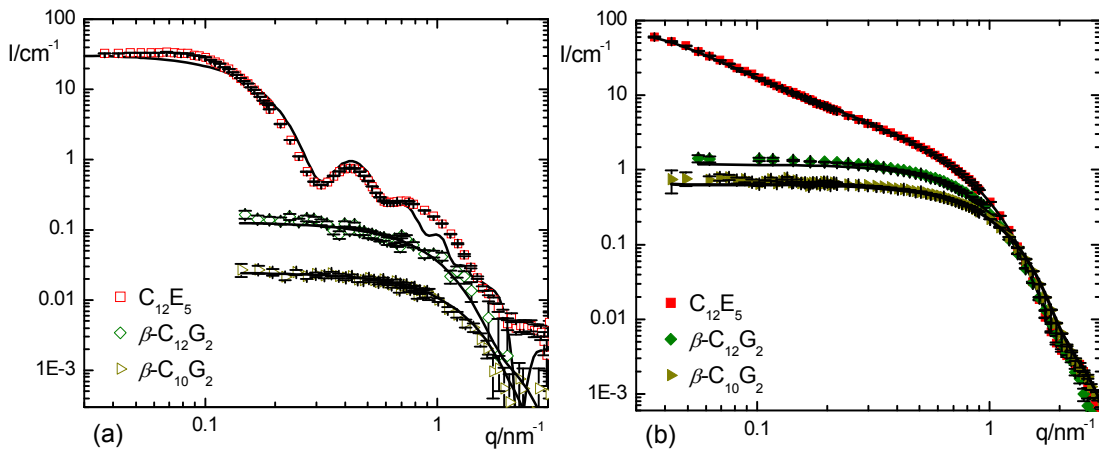


Figure 4.5. SANS profiles of $C_{12}E_5$, $\beta\text{-}C_{12}G_2$ and $\beta\text{-}C_{10}G_2$ (pH 9, 298 K): (a) in the presence of 1.8 wt-% colloidal silica in contrast matching H_2O/D_2O ; surfactant concentrations (vol.-%): 0.80 ($C_{12}E_5$), 0.08 ($\beta\text{-}C_{12}G_2$) and 0.16 ($\beta\text{-}C_{10}G_2$); solid lines represent fits by the micelle-decorated silica model ($C_{12}E_5$) or the ellipsoidal core-shell model for micelles ($\beta\text{-}C_{12}G_2$, $\beta\text{-}C_{10}G_2$). (b) surfactant micelles (1 vol.-%) in D_2O in the absence of silica (1 vol.-% for each surfactant). Solid lines represent fits with the wormlike polymer model ($C_{12}E_5$) or the ellipsoidal core-shell model ($\beta\text{-}C_{12}G_2$, $\beta\text{-}C_{10}G_2$).

and equatorial semi-axis b , surrounded by a head group layer of constant thickness d (i.e., assumed to be the same along the short and long axes). The results are presented in Table 4.3. For the maltoside surfactants in the silica dispersion the best fit was obtained with d values in the range 0.60 – 0.62 nm, in agreement with the values for the surfactant micelles in the absence of the silica ($d = 0.62$ nm). In the case of $C_{12}E_5$ in aqueous solution, the scattering profile could be fitted by a worm-like form factor model characterized by a cylindrical cross-section with a core radius R_c (~ 1.40 nm), a Kuhn-length l (~ 41 nm) and a contour length L (~ 310 nm), as explained in chapter 2. The values of these parameters are in good agreement with those found by Menge et al. [4.27]. Details of these analysis in D_2O will be presented elsewhere [4.26].

Figure 4.6 shows scattering profiles of silica dispersions with different amounts of adsorbed $C_{12}E_5$, corresponding to four different surface concentrations along the adsorption isotherm ($\frac{1}{4}\Gamma_{mx}$, $\frac{1}{2}\Gamma_{mx}$, $\frac{3}{4}\Gamma_{mx}$ and Γ_{mx}). As can be seen, both the scattered intensity and the oscillation in $I(q)$ at intermediate q values increases with increasing surface concentration

of $C_{12}E_5$. In particular, a pronounced maximum at $q = 0.42 \text{ nm}^{-1}$ develops as Γ increases. Below, we analyse these scattering profiles in terms of two form factor models.

Table 4.3. Parameters of the oblate-ellipsoid core-shell model for the SANS profiles of the micelles of β - $C_{10}G_2$ and β - $C_{12}G_2$ in aqueous solution (D_2O) and in the silica dispersion in contrast-matching H_2O/D_2O .

Surfactant	aqueous solution				silica dispersion			
	a (nm)	b (nm)	d (nm)	n_{agg}	a (nm)	b (nm)	d (nm)	n_{agg}
β - $C_{10}G_2$	1.20	2.21	0.62	83	1.16	2.10	0.60	73
β - $C_{12}G_2$	1.46	2.74	0.62	131	1.47	2.82	0.62	140

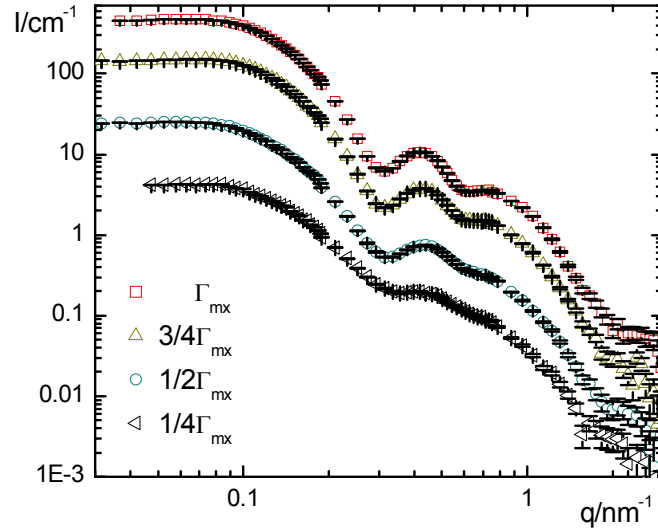


Figure 4.6. SANS profiles of 1.8 wt-% silica in contrast-matching H_2O/D_2O (pH 9, 298 K) in the presence of different amounts of $C_{12}E_5$, corresponding to surface concentration Γ_{mx} , $\frac{3}{4}\Gamma_{\text{mx}}$, $\frac{1}{2}\Gamma_{\text{mx}}$ and $\frac{1}{4}\Gamma_{\text{mx}}$. The curves for higher surface concentrations are shifted vertically relative to that of $\frac{1}{4}\Gamma_{\text{mx}}$ by factors of 2 ($\frac{1}{2}\Gamma_{\text{mx}}$), 6 ($\frac{3}{4}\Gamma_{\text{mx}}$) and 14 (Γ_{mx}).

4.2.3.1 Core-Shell Model

As a first approach, a spherical core-shell model was adopted to fit the scattering profiles of the 1.8 wt-% colloidal silica with adsorbed $C_{12}E_5$ (Figure 2.16A). The particle form factor of this model, given by eq. (2.35) in Section 2, has been used by Cummins et al. [4.6] in their study of surfactant adsorbed layers on colloidal silica. Figure 4.7a shows fits of the data at saturation surface coverage (Γ_{mx}) of $C_{12}E_5$ with three values of the layer thickness, viz. $\delta = 4.0$,

4.4, and 4.6 nm. Clearly these values are causing too high scattering intensities except for the high- q region. However, the maximum at $q = 0.42 \text{ nm}^{-1}$ and the scattering intensities at lower q are nicely reproduced when the intensities resulting from the model with $\delta = 4.0, 4.4$, and 4.6 nm are multiplied by factors $f = 0.4, 0.34$ and 0.28 , respectively, as seen in Fig. 4.7b. Similar results were obtained for surface concentrations $\frac{3}{4}\Gamma_{\text{mx}}$ and $\frac{1}{2}\Gamma_{\text{mx}}$ with assumed values of the layer thickness of 3.6 and 2.8 nm , respectively. For the surface concentration $\frac{1}{4}\Gamma_{\text{mx}}$ the maximum in the scattering curve at $q = 0.42 \text{ nm}^{-1}$ is rather weak and not well-reproduced with any value of the layer thickness (results not shown). However, in all cases the core-shell model curves fail to fit the high- q regions of the scattering profiles when multiplied by any factor $f < 1$. Figure 4.7b indicates that the core-shell model adjusted to the maximum at $q = 0.42 \text{ nm}^{-1}$ also fits the behaviour at lower q but strongly underestimates the surface area of the total adsorbed surfactant (behaviour at high q). The large difference between core-shell model and experiment at large q (see Fig. 4.7b) cannot be removed by changes in the subtracted incoherent background within the limits of experimental uncertainty. Since the background is known to $\pm 0.003 \text{ cm}^{-1}$ in the present study, errors here are never sufficient to catch up the differences between the models at high- q (cf. Fig. 4.7).

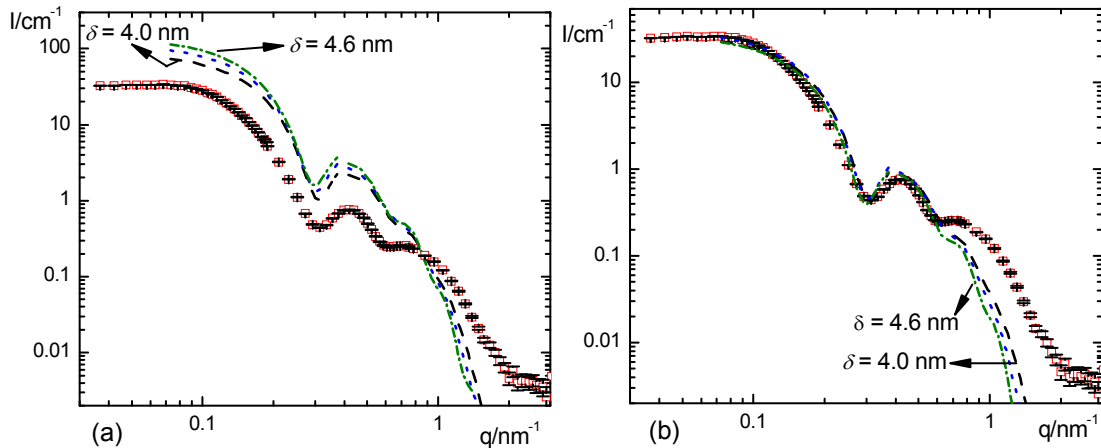


Figure 4.7. SANS profile for surface concentration Γ_{mx} of C_{12}E_5 on silica in contrast matching $\text{H}_2\text{O}/\text{D}_2\text{O}$: (a) Experimental data and intensities predicted by the spherical core-shell model with shell thicknesses $\delta = 4.0, 4.4$ and 4.6 nm ; (b) same as in (a) but predicted intensities multiplied by factors $f = 0.4, 0.34$ and 0.28 , respectively.

The effect of background subtraction on the data analysis in terms of the present models is demonstrated in Fig. 4.8. In order to verify the influence of the incoherent background's subtraction in the improvement of the fit at large q obtained either by core-shell model or by micelle decorated silica model, the incoherent background value has been changed slightly (Figure 4.8) resulting no negligible improvement in both models, due to that the Porod Law constant A_p has the same value for any incoherent background value, as can be seen in Figure 4.8. The best agreement with the Porod Law is given by the scattering profile with an incoherent background value of 0.404 cm^{-1} for the surface concentration Γ_{mx} of C_{12}E_5 on silica in contrast matching $\text{H}_2\text{O}/\text{D}_2\text{O}$, such values are typical for $\text{H}_2\text{O}/\text{D}_2\text{O}$ mixtures. At lower background's values than 0.404 cm^{-1} the constant intensity at high- q is present like in the raw data with background, which disappear by increasing background's value. By subtracting too high background values, arbitrarily high and non physical apparent power law exponents can be generated over a very limited q -range.

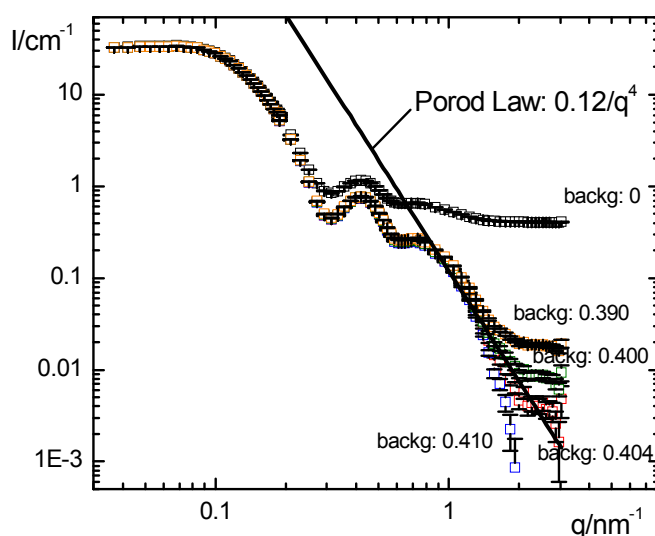


Figure 4.8. SANS profile for surface concentration Γ_{mx} of C_{12}E_5 on silica in contrast matching $\text{H}_2\text{O}/\text{D}_2\text{O}$ with different incoherent background's subtraction.

Hence the differences between core-shell model and experiment at high q imply that the surfactant is not forming a uniform layer but a different type of aggregate, e.g., surface micelles, which have a higher surface area at a given total adsorbed volume. Surfactant surface areas and volumes and

numbers of adsorbed aggregates were estimated for different types of surface aggregates. It was found that the model of micelle-decorated silica beads [4.8. 4.21], with spherical surface aggregates as sketched in Figure 2.16B, gives a good representation of the data.

4.2.3.2 Micelle- Decorated Silica Model

In applying the model of micelle-decorated colloidal silica beads the first step was to determine how much adsorbed surfactant volume is in excess ($l, q \rightarrow 0$), and how much surface is missing in the core-shell model ($l, q \rightarrow \infty$). The real adsorbed surfactant volume was estimated by introducing the effective core-shell volume fraction of the surfactant, $X = \sqrt{f}$, based on a fixed layer thickness of 4.0 nm. For example, at 100% surface coverage the intensities estimated by the core-shell model had to be multiplied by a factor $f = 0.40$ to match the measured intensities at low and intermediate q values, which implies that $X = 0.63$, i.e. only 63% of the layer volume is occupied by $C_{12}E_5$. The total surface area of the adsorbed surfactant, A_{tot} , was calculated from the specific surface area S/V as determined by Porod's law ($S/V = A_p/2\pi\Delta\rho^2$, where A_p is the Porod constant) and from the number density of silica particles, $N/V = 3.72 \times 10^{-6} \text{ nm}^{-3}$, by the relation $A_{\text{tot}} = (S/V)_{\text{surf}}/(N/V)_S$. The fitting of the scattering curves with this model was based on the film thickness as obtained in the spherical core-shell model, which reproduces very well the maximum at intermediate q . As seen in Figure 4.7, the predicted intensities for the core-shell model with layer thicknesses δ of 4.0, 4.4 and 4.6 nm are very similar. We have calculated the surface area and volume of the adsorbed surfactant based on these three values of δ , and with these two new parameters it was possible to estimate the number and dimensional parameters of surface aggregates of different geometry. Calculations were performed for individual spherical, patchlike, and wormlike micelles (see Fig. 4.9A-9C). They were made for an assumed layer thickness of 4.0 nm and full surface coverage (Γ_{mx}). The resulting geometrical parameters (radius R , length or height L) are given in Table 4.4. It was found

that spherical aggregates adsorbed as separate entities represent the most acceptable geometry of the surface aggregates. The samples with surface concentrations $\frac{1}{4}\Gamma_{\text{mx}}$, $\frac{1}{2}\Gamma_{\text{mx}}$, and $\frac{3}{4}\Gamma_{\text{mx}}$ conform to a similar behaviour. The respective model parameter are summarized in Table 4.5. The maximum in the scattering curves at low q which is due to silica-silica interactions is not accounted for in the model in its present form but could in principle be included by a structure factor, as proposed by Despert et al [4.8].

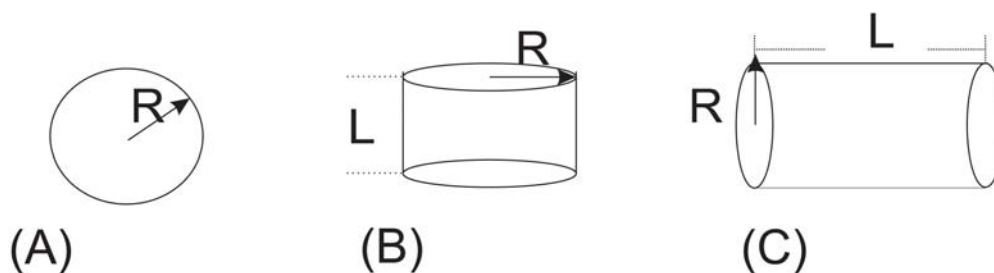


Figure 4.9. Cartoons of different shapes of surfactant self-assembly structures on silica beads: spheres (A); patch (B), and wormlike (C).

Table 4.4. Parameters of the micelle-decorated silica model for different geometries of the micellar surface aggregates of C_{12}E_5 at 100% surface coverage (Γ_{mx}).

Geometry	R (nm)	L (nm)	N_{mic}
Spherical	2.0	-	98
Patchlike	1.7	-	93
Wormlike	2.0	2.9	114

Table 4.5. Parameters of the micelle-decorated silica model for spherical surface aggregates of C_{12}E_5 on silica particles: A_p , Porod constant, S/V , specific surface area, A_{tot} , total surface area of the adsorbed surfactant, R_{mic} , N_{mic} , radius and number of surface aggregates per particle.

Surf. Conc.	A_p ($10^{-2} \text{ cm}^{-1} \text{ nm}^{-4}$)	S/V (10^{-3} nm^{-1})	A_{tot} (10^3 nm^2)	δ (nm)	R_{mic} (nm)	N_{mic}
$\frac{1}{4}\Gamma_{\text{mx}}$	3.32	6.24	1.69	4	2.2	28
$\frac{1}{2}\Gamma_{\text{mx}}$	6.23	11.7	3.17	4	2.1	52
$\frac{3}{4}\Gamma_{\text{mx}}$	9.73	18.3	4.94	4	2.1	73
Γ_{mx}	12.00	22.6	6.10	4	2.0	98

The position of this interaction peak at 0.09 nm^{-1} does not change due to the constant silica volume fraction used in our experiments. The position and amplitude of the maximum at $q = 0.42 \text{ nm}^{-1}$ is very well reproduced by the model without any arbitrary factor, but some discrepancies between the experimental and predicted $I(q)$ appear in the high- q Porod regime at each surface coverage, where the model overestimates ($\frac{1}{4}\Gamma_{\text{mx}}$, $\frac{1}{2}\Gamma_{\text{mx}}$) or underestimates ($\frac{3}{4}\Gamma_{\text{mx}}$, Γ_{mx}) the surface area of the adsorbed surfactant aggregates, as seen in Figure 4.10.

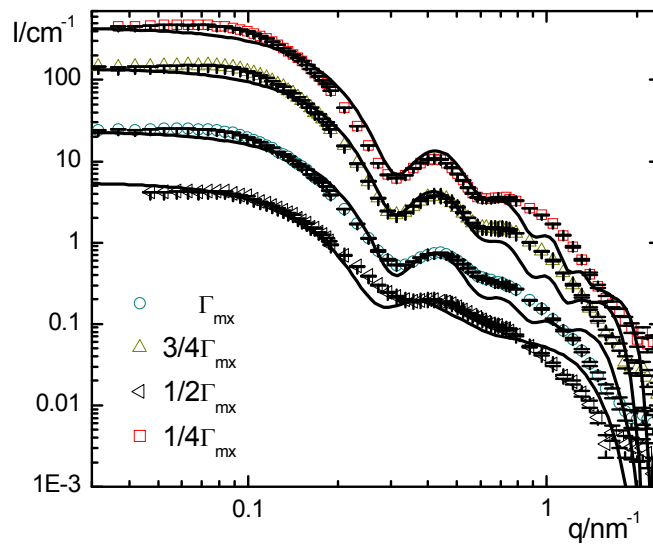


Figure 4.10. SANS profiles for surface concentrations Γ_{mx} , $\frac{3}{4}\Gamma_{\text{mx}}$, $\frac{1}{2}\Gamma_{\text{mx}}$ and $\frac{1}{4}\Gamma_{\text{mx}}$ of C_{12}E_5 on silica in contrast matching $\text{H}_2\text{O}/\text{D}_2\text{O}$ (same data as in Fig. 4.6), and fits by the micelle-decorated silica model (full curves). Results for higher surface concentrations are shifted relative to those for $\frac{1}{4}\Gamma_{\text{mx}}$ by factors of 2 ($\frac{1}{2}\Gamma_{\text{mx}}$), 6 ($\frac{3}{4}\Gamma_{\text{mx}}$), and 14 (Γ_{mx}).

The quality of the fits was not significantly improved when in the former case ($\frac{1}{4}\Gamma_{\text{mx}}$, $\frac{1}{2}\Gamma_{\text{mx}}$) the radius of the micelles was increased at fixed number of adsorbed aggregates ($N_{\text{mic}} = 28$ for $\frac{1}{4}\Gamma_{\text{mx}}$, or $N_{\text{mic}} = 52$ for $\frac{1}{2}\Gamma_{\text{mx}}$), nor in the latter case ($\frac{3}{4}\Gamma_{\text{mx}}$, Γ_{mx}) when the radius of the aggregates was decreased at fixed N_{mic} . Such discrepancies may be due to the low surface coverage, possibly leading to the coexistence of populations of aggregates or unimers, which is not captured by our model because the adsorbed surfactant micelles have been modeled as monodisperse spheres, which induce strong oscillations in the high- q region.

4.3 Discussion

The present study builds on the early work of Cummins et al. [4.6] who indicated that the SANS scattering profiles of C_nE_m surfactants on Ludox silica could result from surface micelles, and on the first detailed description of the geometry of such surface micelles by one of the present authors [4.21]. The experiments were made with the home-made silica instead of commercial Ludox in order to attain a better control of the mean particle size, a lower polydispersity and a better colloidal stability of the samples. The surface chemistry of these samples may be somewhat different from that of Ludox, but this point is considered not important. A prominent feature of the scattering profiles of silica with adsorbed $C_{12}E_5$ is the maximum in $I(q)$ at $q = 0.42 \text{ nm}^{-1}$ which can be taken as a measure of the amount of surfactant forming the adsorbed layer. The analysis of the scattering profiles has shown, however, that the spherical core-shell model adjusted to this maximum in $I(q)$ strongly underestimates the surface area of the adsorbed surfactant as extracted from the high- q regime of the scattering profiles. This result suggests that the adsorbed surfactant is not forming a uniform bilayer but a different type of aggregate. On the basis of the micelle-decorated silica model, assuming spherical micellar surface aggregates, it is found that the number of adsorbed aggregates N_{mic} increases as the concentration of surfactant in the system is increased (Table 4.5 and Fig. 4.10). The model also predicts that the micelle radius R_{mic} somewhat decreases as the surfactant loading is increased. However, this predicted trend is probably not significant due to the limited resolution of the experimental data. The resulting mean value of R_{mic} is similar to the cross-sectional radius of the wormlike micelles of $C_{12}E_5$ formed in aqueous solutions ($R \approx 2.4 \text{ nm}$) as obtained from Guinier expression for cylindrical micelles.

For spherical surface aggregates the micelle-decorated silica model predicts that the number of surface aggregates per silica particle, N_{mic} , can be as high as about one hundred (Table 4.5). This large number corresponds to a dense layer of surface micelles, as can be seen from graphical

representations of model results (not shown), or by a simple estimation of the maximum number of spheres of radius R_{mic} in contact with a central sphere of radius R_{Si} . Assuming that the smaller spheres arrange on a hexagonal lattice at a distance $(R_{\text{S}} + R_{\text{mic}})$ from the centre, then $N^{\text{max}} = (2\pi/\sqrt{3})(s + 1)^2$, where $s = R_{\text{S}}/R_{\text{mic}}$. With $R_{\text{S}} = 8.2$ nm and $R_{\text{mic}} = 2.0$ nm we find $N^{\text{max}} = 94$. Hence at the highest surface concentration, the layer geometry consistent with the scattering data is a dense layer of micelles. Admittedly, the exact geometry of this layer may differ from the one proposed here, *e.g.* the micelles might form bridges and build an undulating bilayer. In this case, however, high bending energy of the surfactant monolayer, forcing it to deviate from its preferred globular arrangement, would have to be accounted for. In summary, the micelle-decorated silica bead model accounts simultaneously for the high coverage, and the high specific surface area as measured (model-free) in the high- q range.

The finding that C₁₂E₅ is adsorbed in the form of small surface micelles at the silica beads is remarkable in view of the fact that aggregates of smaller mean curvature (*e.g.*, wormlike micelles) are favoured in aqueous solutions and bilayer films are formed in the adsorption onto flat surfaces. We conjecture that the preference for small surface aggregates is a consequence of the high surface curvature of the silica nanoparticles which prevents an effective packing of the surfactant molecules in a bilayer film. Note that for particles of radius 8 nm and a bilayer thickness of 4 nm the mean area per molecule at the mid-plane of the bilayer is 50% greater than the respective area directly at the surface. Accordingly, an effective packing of the hydrophobic tails is not possible in a bilayer configuration (even if more molecules are accommodated in the outer layer than in the inner layer). Instead, small (roughly spherical) aggregates will be favoured, as these aggregates allow the most effective packing of the hydrophobic tails on small spherical particles. This argument applies not only to the region of low surface concentrations but also to the plateau region of the isotherm. Further work with silica particles of different size and surfactants of different packing parameters is needed to corroborate these findings.

References of Chapter 4

- [4.1] McDermott, D. C.; Lu, J. R.; Lee, E. M.; Thomas, R. K.; Rennie, A. R. *Langmuir*, **1992**, *8*, 1204-1210.
- [4.2] Böhmer, M. R.; Koopal, L. K.; Janssen, R.; Lee, E. M.; Thomas R. K.; Rennie, A. R. *Langmuir*, **1992**, *8*, 2228-2239.
- [4.3] (a) Tiberg, F.; Jönsson, B.; Tang J.; Lindman, B. *Langmuir*, **1994**, *10*, 2294-2300. (b) Tiberg, F. *J. Chem. Soc., Faraday Trans. II*, **1996**, *92*, 531-538.
- [4.4] Howse, J. R.; Steitz, R.; Pannek, M.; Simon, P.; Schubert, D. W.; Findenegg, G. H. *Phys. Chem. Chem. Phys.*, **2001**, *3*, 4044-4051.
- [4.5] Matsson, M. K.; Kronberg, B.; Claesson, P. M. *Langmuir*, **2004**, *20*, 4051-4058.
- [4.6] (a) Cummins, P. G.; Staples, E.; Penfold, J. *J. Phys. Chem.*, **1990**, *94*, 3740-3745. (b) Cummins, P. G.; Penfold, J.; Staples, E. *J. Phys. Chem.*, **1992**, *96*, 8092-8094. (c) Penfold, J.; Staples, E.; Tucker, I.; Cummins, P. *J. Phys. Chem.*, **1996**, *100*, 18133-18137.
- [4.7] Giordano-Palmino, F.; Denoyel, R.; Rouquerol, J. *J. Colloid Interface Sci.*, **1994**, *165*, 82-90.
- [4.8] Despert, G.; Oberdisse, J. *Langmuir*, **2003**, *19*, 7604-7610.
- [4.9] (a) Levitz, P.; van Damme, H.; Keravis, D. *J. Phys. Chem.*, **1984**, *88*, 2228-2235. (b) Levitz, P.; van Damme, H. *J. Phys. Chem.*, **1986**, *90*, 1302-1310. (c) Ström, C.; Hansson, P.; Jönsson, B.; Söderman, O. *Langmuir*, **2000**, *16*, 2469-2474.
- [4.10] Qiao, Y.; Schönhoff, M.; Findenegg, G. H. *Langmuir*, **2003**, *19*, 6160-6167.
- [4.11] Findenegg, G. H.; Eltekov, A. Y. *J. Chromatogr. A*, **2007**, *1150*, 236-240.
- [4.12] Dietsch, O.; Eltekov, A.; Bock, H.; Gubbins, K. E.; Findenegg, G. H. *J. Phys. Chem. C*, **2007**, *111*, 16045-16054.
- [4.13] Manne, S.; Gaub, H.E. *Science*, **1995**, *270*, 1480-1482.
- [4.14] Dong, J.; Mao, G. *Langmuir*, **2000**, *16*, 6641-6647.
- [4.15] Patrick, H. N.; Warr, G. G.; Manne, S.; Aksay, I. A. *Langmuir*, **1997**, *13*, 4349-4356.
- [4.16] Grant, L. M.; Tiberg, F.; Ducker, W. A. *J. Phys. Chem. B*, **1998**, *102*, 4288-4294.
- [4.17] (a) Tiberg, F.; Brinck, J.; Grant, L. M. *Current Opin. Colloid Interface Sci.*, **1999**, *4*, 411-419. (b) Warr, G. G. *Current Opin. Colloid Interface Sci.*, **2000**, *5*, 88-94.
- [4.18] (a) Király, Z.; Börner, R. H. K.; Findenegg, G. H. *Langmuir*, **1997**, *13*, 3308-3315. (b) Király, Z.; Findenegg, G. H. *Langmuir*, **2000**, *16*, 8842-8849.
- [4.19] Schulz, J. C.; Warr, G. G.; Hamilton, W. A.; Butler, P. D. *J Phys Chem B*, **1999**, *103*, 11057-11063.
- [4.20] Steitz, R.; Müller-Buschbaum, P.; Schemmel, S.; Cubitt, R.; Findenegg, G. H. *Europhys. Lett.*, **2004**, *67*, 962-968.
- [4.21] Oberdisse, J. *Phys. Chem. Chem. Phys.*, **2004**, *6*, 1557-1561.
- [4.22] Stoeber, W.; Fink, A.; Bohn, E. *J. Colloid Interface Sci.*, **1968**, *26*, 62-69.

- [4.23] (a) Hayter, J. B.; Penfold, J. *Mol. Phys.*, **1981**, *42*, 109-118. (b) Hansen, J. P.; Hayter, J. B. *Mol. Phys.*, **1982**, *46*, 651-656.
- [4.24] Gellan, A.; Rochester, C. H. *J. Chem. Soc., Faraday Trans. 1*, **1985**, *81*, 2235-2245.
- [4.25] Gu, T.; Zhu, B.-Y. *Colloids Surf.*, **1990**, *44*, 81-87.
- [4.26] Lugo, D.; Prévost, S.; Findenegg, G. H. unpublished work.
- [4.27] (a) Menge, U.; Lang, P.; Findenegg, G. H. *J. Phys. Chem. B*, **1999**, *103*, 5768-5774. (b) Menge, U.; Lang, P.; Findenegg, G. H.; Strunz, P. *J. Phys. Chem. B* **2003**, *107*, 1316-1320.

5 Effect of Nanoparticle Size on the Morphology of Adsorbed Surfactant Layers*

5.1 Introduction

Surfactants play an important role in many industrial processes involving colloidal dispersions, as their adsorption onto the particles often leads to enhanced colloid stability. A structural characterization of this adsorbed layer is a prerequisite for gaining a better understanding of its mode of operation in stabilizing or flocculating dispersion. Adsorption isotherms of nonionic surfactants on hydrophilic (oxide) surfaces commonly exhibit a pronounced sigmoidal shape, i.e., a low-affinity initial region followed by a region in which the adsorption increases steeply and reaches a plateau near the critical micelle concentration (CMC) [5.1]. This behavior suggests that adsorption represents a surface aggregation similar to micelle formation in solution. Scanning probe microscopy (AFM) studies at planar surfaces indicated that either laterally uniform surfactant bilayers or small surface micelles may be formed, depending on the nature of the surfactant head group and the degree of hydrophilicity of the solid surface [5.2]. The nature of the surfactant layers adsorbed on colloidal particles in aqueous dispersions was studied by small-angle neutron scattering (SANS), which allows to highlight the adsorbed layer against a uniform scattering background by matching the colloidal particles with a partially deuterated aqueous solvent [5.3-5.7]. In the earlier of these studies the adsorbed surfactant was modeled as a laterally uniform layer [5.3, 5.4], but the existence of discrete micellar aggregates at the surface of the silica particles ('micelle-decorated silica beads') has been reported more recently [5.5-5.7]. Recently we reported that the surfactant penta(ethyleneglycol) monododecyl ether ($C_{12}E_5$) is adsorbed in the form of individual spherical surface aggregates on silica nanoparticles of 16 nm diameter [5.7], in agreement with earlier

*modified from published article in *J. Phys. Chem. B*: Lugo, D.M.; Oberdisse, J.; Lapp, A.; Findenegg, G.H. *J. Phys. Chem. B* **2010**, 114, 4183-4191.

findings for the surfactant Triton X-100 on Bindzilttype silica particles of similar size [5.5, 5.6]. This finding is remarkable in view of the fact that $C_{12}E_5$ prefers aggregates of lower mean curvature, viz., worm-like micelles in aqueous solutions [5.8, 5.9], and a laterally homogeneous bilayer on planar hydrophilic silica surfaces [5.2a]. We conjectured that the preference for small surface micelles is a consequence of the high surface curvature of the silica nanoparticles, which prevents an effective packing of the hydrophobic tails in an adsorbed bilayer, whereas a favorable packing of the tails is possible in a spherical micelle. In order to test this concept and to find out to what extent the structure of the adsorbed layer at the surface of the silica nanoparticles depends on the size and chemical nature of the surfactant head group it was of interest to extend this study to a different class of nonionic surfactants. On the other hand, it was of interest to study the influence of size of the silica nanoparticles on the surface aggregate structure of the surfactant.

The present study was performed with dimethyldodecylamine-*N*-oxide ($C_{12}DAO$), an amphoteric surfactant that exists in a zwitterionic (net non-ionic) form at pH above 7, but in a cationic form at low pH due to a protonation of the head group. $C_{12}DAO$ has a much smaller head group of less hydrophilic character than $C_{12}E_5$ [5.10]. Phase diagrams, thermodynamics and self-assembly structures of aqueous systems of alkyl dimethylamine oxides have been extensively studied [5.11], and the interaction of alkyl DAO systems with hydrophilic and hydrophobic surfaces was investigated by adsorption calorimetry [5.12, 5.13a] and streaming potential measurements [5.13b]. Based on the adsorption enthalpy results, Pettersson and Rosenholm [5.13a] concluded that the adsorption mechanism at the solution/silica interface of $C_{12}DAO$ in its nonionic form is different from that in the protonated form, and they speculated that in the nonionic form $C_{12}DAO$ forms ellipsoidal aggregates; while in the protonated form $C_{10}DAO$ and $C_{12}DAO$ are likely to form spherical surface micelles. The conclusion about the formation of spherical surface micelles by $C_{10}DAO$ on silica was consistent with the sorption enthalpy results of Király and Findenegg [5.12]. However, in neither of these studies direct information about the surface aggregate structures was obtained. In the present

work we use SANS to clarify the structure of the adsorbed layer of $C_{12}DAO$ on silica nanoparticles of three different sizes (16 to 42 nm diameter), with a focus on the effect of particle size on the type of surface aggregate formed.

5.2 Results and Discussion

5.2.1 Characterization of the silica particles

The silica samples were characterized by transmission electron microscopy (TEM), small-angle neutron scattering (SANS), zeta potential and nitrogen adsorption measurements. TEM images indicate that silica I and II, which were obtained by silica deposition on Ludox, have a wider size distribution than silica III, which was prepared by direct Stöber synthesis [5.14] (Figure 5.1). The average particle radius, R_{TEM} , and its standard deviation, SD_{TEM} , were determined by Gaussian fits to the histograms in Fig. 5.1 (see Table 5.1).

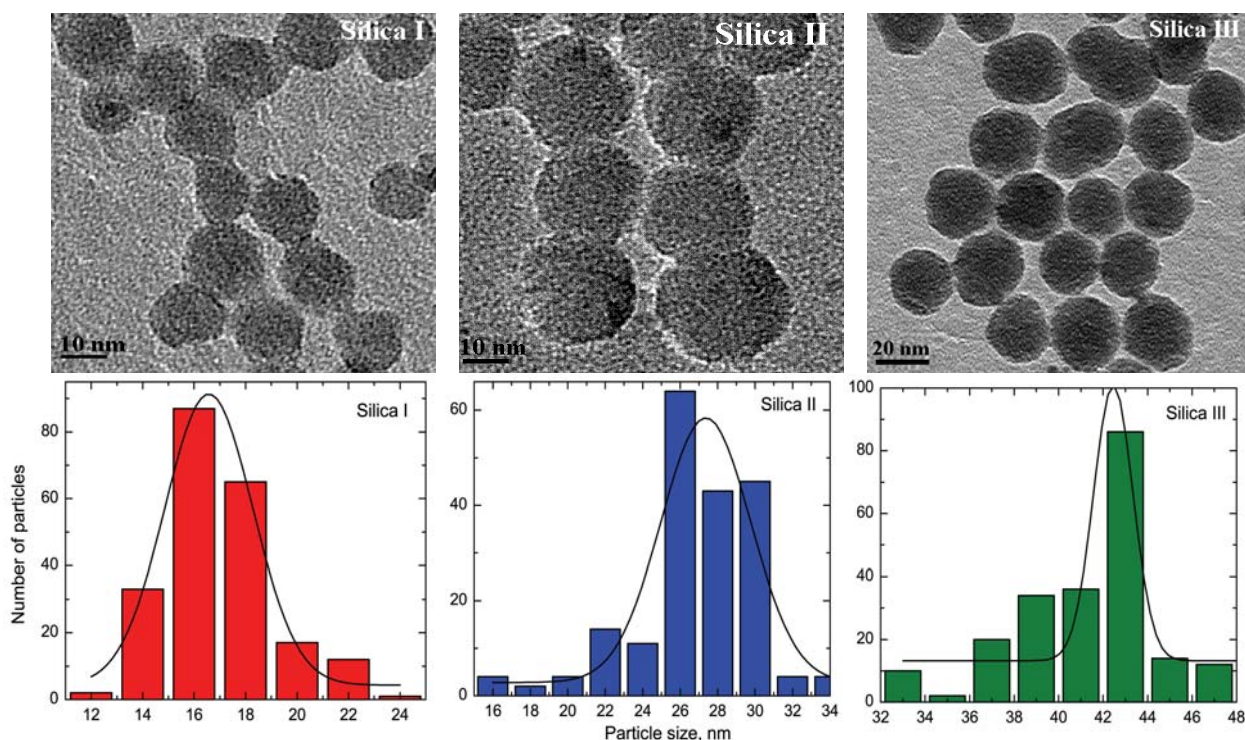


Figure 5.1. TEM images and particles size distribution histograms for silica I, silica II and silica III. The histograms are based on the diameters of at least of 200 different particles from different TEM images.

The silica particles prepared by overgrowth of Ludox (silica I and II) have

a higher zeta potential than silica III at pH 9 (see Table 5.1), indicating a somewhat different surface-chemical behavior of the two types of silica. The zeta potentials suggest that all silica dispersions are electrostatically stabilized.

Table 5.1. Characterization of the silica nanoparticles.*

Silica Sol	R_{TEM} nm	SD_{TEM}	ζ mV	κ $\mu\text{m cm}^{-1}$
I	8.3	0.126	-45.6	121
II	13.7	0.104	-43.2	66
III	21.3	0.027	-32.7	69

*average particle radius R and size distribution SD from TEM, zeta potential ζ and conductivity κ of the silica dispersion

Quantitative information about the mean particle size and size distribution of the silica sols was obtained by SANS. The form factor of the particles, $F(q)$, was measured in dilute (0.4 - 1.5 vol.-%) aqueous suspensions of D₂O-rich water (scattering length density ρ_D in the range 5.0 - 5.2x10¹⁰ cm⁻²). The scattering profiles $I(q)$ shown in Figure 5.2 exhibit features of scattering from slightly polydisperse spheres. The characteristic oscillation in $I(q)$ at intermediate q , which relates to the radius of the beads, is located at $q \approx 0.7$ nm⁻¹ (silica I), $q \approx 0.4$ nm⁻¹ (silica II), and $q \approx 0.25$ nm⁻¹ (silica III). As a first step, a model-free analysis of the low- q (Guinier) and high- q (Porod) scattering regimes was performed [5.15, 5.16], assuming monodisperse spheres. The Guinier approximation, $I(q) = I_0 \exp(-R_g^2 q^2/3)$, was used to estimate the limiting scattered intensity $I_0 = I(q \rightarrow 0)$ and the gyration radius R_g , which is related to the particle radius R_G by $R_g / R_G = \sqrt{3/5}$. The Porod law, $I(q) = A_P \cdot q^{-4} + C$, where $A_P = 2\pi\Delta\rho_D^2(S/V)$ is the Porod constant, was used to determine the volume-related surface area S/V , which yields a nominal particle radius of monodisperse spheres by $S/V = 3\phi / R_P$, where ϕ is the volume fraction of the particles. As can be seen in Table 5.2, the values of R_G are significantly larger than those of R_P for the present silica samples. This difference may be due to polydispersity and/or deviations from spherical geometry, or surface roughness of the particles.

Table 5.2. Characterization of the silica dispersions by SANS.*

Silica Sol	R_G (nm)	R_P (nm)	R_S (nm)	σ	$\langle R_S \rangle$ (nm)	$\langle A_S \rangle$ (nm ²)	$\langle V_S \rangle$ (nm ³)
I	10.70	5.18	8.20	0.10	8.24	$8.62 \cdot 10^2$	$2.42 \cdot 10^3$
II	15.79	11.76	13.50	0.10	13.57	$2.34 \cdot 10^3$	$1.08 \cdot 10^4$
III	23.04	13.94	21.00	0.10	21.11	$5.65 \cdot 10^3$	$4.06 \cdot 10^4$

*Guinier radius R_G , Porod radius R_P , parameters R_S and σ of the log-normal size distribution, average radius $\langle R_S \rangle$, average surface area $\langle A_S \rangle$, and average volume $\langle V_S \rangle$ of the silica beads.

The quantities R_G , I_0 , R_P were used as input for determining the parameters of a log-normal size distribution of spherical particles, *i.e.*, polydispersity σ and average radius R_S of the silica particles [5.17] by using the eqs. (5.1), (2.33) and (2.34):

$$I_0 = \phi \Delta \rho^2 \frac{4\pi}{3} \frac{\langle R^6 \rangle}{\langle R^3 \rangle} = \phi \Delta \rho^2 \frac{4\pi}{3} R_S^3 e^{27\sigma^2/2} \quad (5.1)$$

The resulting values of σ and R_S from the model-free analysis (*i.e.*, without a complete form factor fit) agree within 5 to 15% with the values obtained by the nonlinear fit for spherical particles with a log-normal size distribution (*cf.* Section 2.4.2) Deviations in this order of magnitude can be attributed to the limited accuracy of the Guinier approximation in a q -range where $qR_g \approx 1$, and to errors caused by the highly dilute samples [5.18].

As can be seen in Figure 5.2, the measured intensities $I(q)$ of each silica dispersion are well reproduced by a spherical form factor model with a log-normal size distribution. The scattering profile of silica III (largest particle size) attains a plateau in the low- q limit, indicating negligible inter-particle structure factor. In the case of the silica I, an interaction peak at $q_0 \approx 0.095 \text{ nm}^{-1}$ appears, indicating repulsive electrostatic interactions between the silica particles. This interaction peak can be reproduced by standard theory [5.19], as was shown in previously studies [5.20]. Since interactions between the particles are not at the focus of the present study, no attempt was made to reproduce this maximum in $I(q)$ at low q . However, we checked the consistency of the particle radius \tilde{R} that can be calculated from the position of the peak maximum, as explained

elsewhere [5.7]. This check yields a value $\tilde{R} = 8.6$ nm, which is about 5% higher than the value obtained by the log-normal size distribution (Table 5.2). For silica sol II, no $I(q)$ data at sufficiently low q have been obtained and thus it is not clear if an interaction peak appears in the dilute regime of the present study.

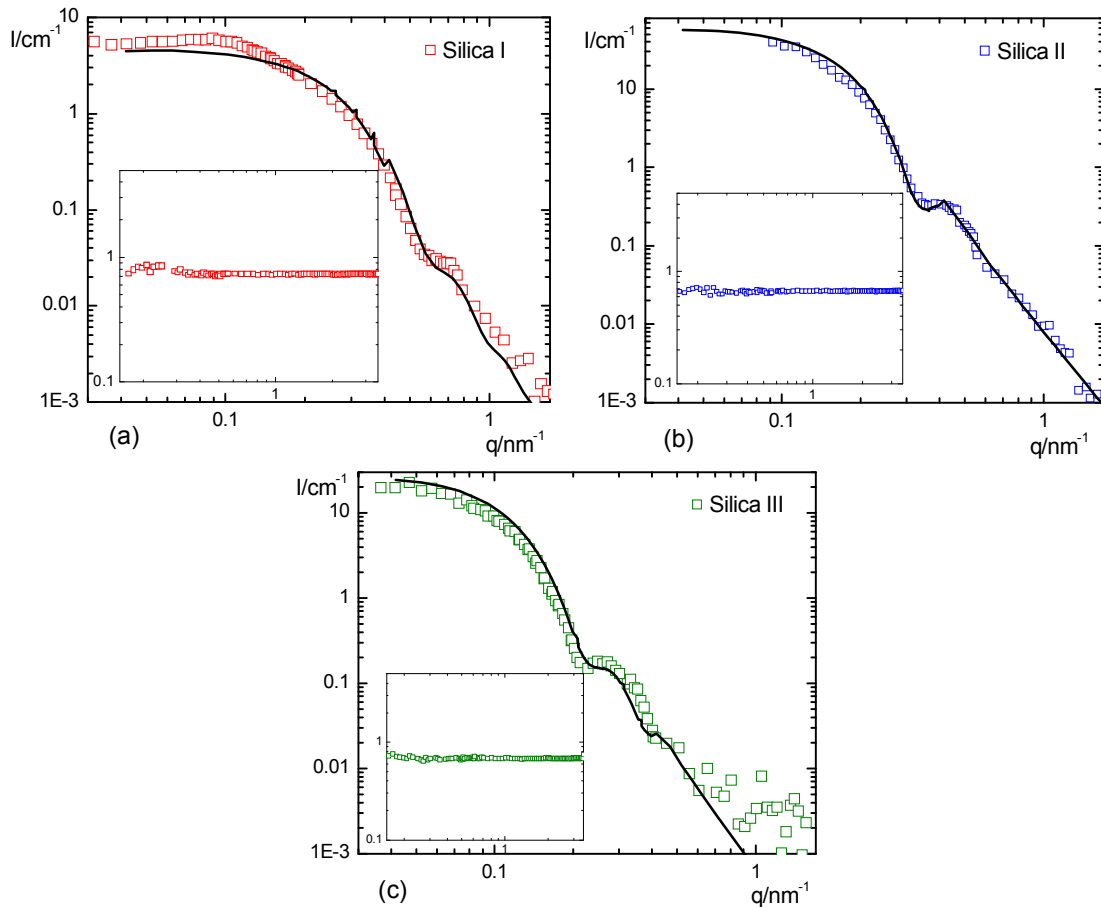


Figure 5.2. Characterization of the silica nanoparticles by neutron small-angle scattering (SANS). Experimental scattering profiles $I(q)$ of dilute silica dispersions in nearly pure D_2O at pH 9 (298 K): (a) Silica I, (b) Silica II and (c) Silica III. The solid line represents a fit with the log-normal size distribution function. The inset shows $I(q)$ of the silica in contrast-matching $\text{H}_2\text{O}/\text{D}_2\text{O}$ to indicate the quality of the contrast match.

The specific surface area a_s of the dried and outgassed silicas sols was determined from the nitrogen adsorption isotherms by the BET method [5.21]. Linear BET plots (correlation coefficient ≥ 0.9996) were found for relative pressures p/p_0 from 0.05 to 0.3 for the three samples. The resulting BET plots

are shown in Figure 5.3. The insets in Figure 5.3 show the adsorption isotherm over the entire range of relative pressures. The features at $p/p_0 > 0.5$ seen in these graphs are caused by capillary condensation of nitrogen in the voids between close-packed silica beads in the dried sample. These features are of no relevance for the present work.

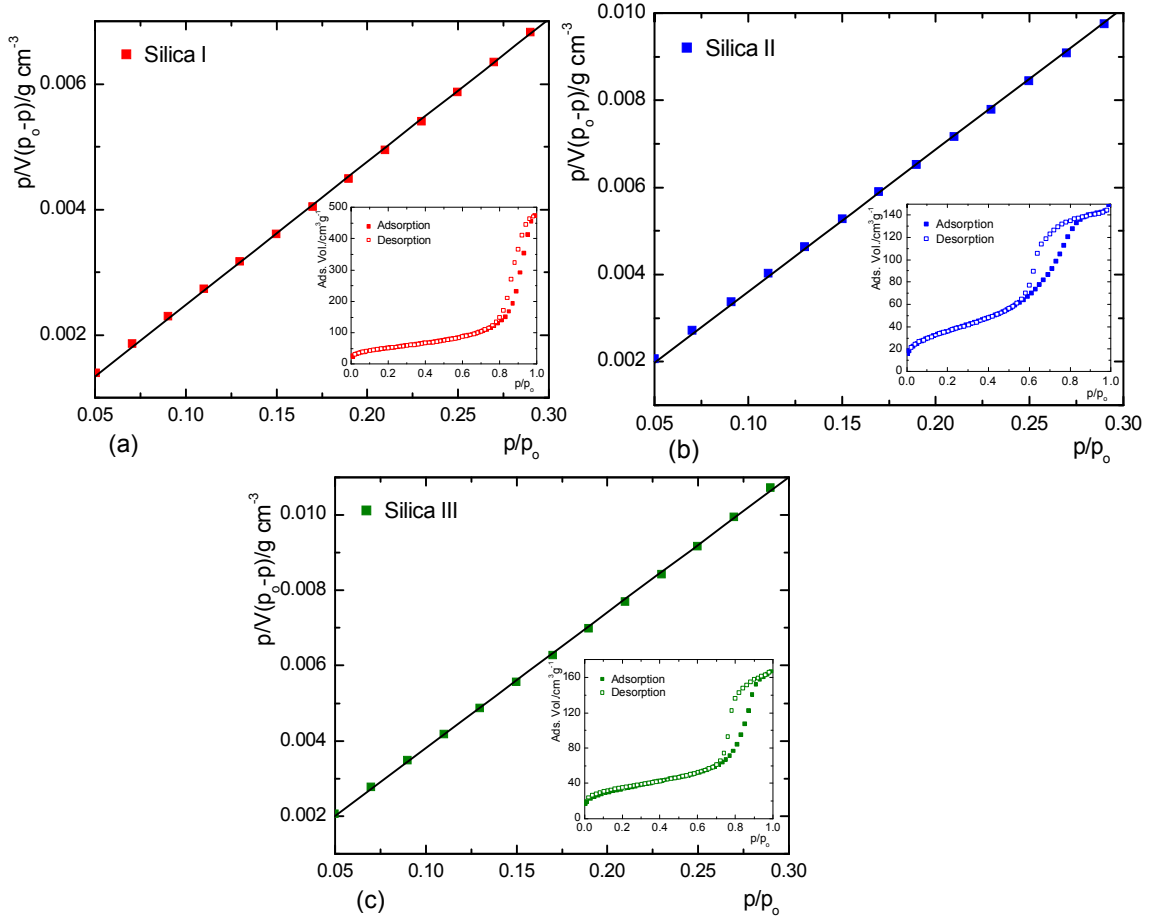


Figure 5.3. Characterization of the silica samples by nitrogen adsorption: BET plots of the isotherms (a) Silica I, (b) Silica II and (c) Silica III. The insets show the entire adsorption isotherm.

Values of the specific surface area a_s , the adsorption constant C_{BET} , and the correlation coefficient of the fits are given in Table 5.3, as well as the values of the geometric surface area $a_{\text{geom}} = 3/\rho_s R_s$ derived from the particle radius R_s (from SANS) and the mass density of silica ρ_s (2.20 g cm^{-3}). Values of a_s/a_{geom} between 1 and 2 are obtained, increasing with the particle radius. This trend indicates that the surface roughness of the particles increases with size. Silica I

($a_s/a_{\text{geom}} = 1.14$) has a very low surface roughness, while the value $a_s/a_{\text{geom}} = 1.85$ for silica III indicates significant roughness (surface corrugations at a periodicity $l \approx 1$ nm and profile depth $d \approx l$). Alternatively, the result for silica III may be explained by a moderate degree of microporosity.

Table 5.3. Surface characterization of the silicas by nitrogen adsorption.*

Silica Sol	a_s , $\text{m}^2 \text{g}^{-1}$	C_{BET}	Corr. Coeff.	a_{geom} , $\text{m}^2 \text{g}^{-1}$	a_s/a_{geom}
I	190	97	0.9997	166	1.14
II	134	70	0.9999	101	1.33
III	120	175	0.9996	65	1.85

*Specific surface area a_s from the BET analysis; geometrical surface area a_{geom} from the particle radius and mass density of silica.

5.2.2 SANS study of adsorbed C₁₂DAO layer

Scattering profiles $I(q)$ for C₁₂DAO in the absence and presence of silica particles are shown in Figure 5.4. These SANS measurements (and those presented in the later figures) were made in contrast-matching H₂O/D₂O, so that the scattering contrast is solely due to the surfactant. Accordingly, the difference in the scattering profiles obtained in the absence and presence of silica in Fig. 5.4 must be due to a different organization of the surfactant. As discussed later, the scattering profile in the absence of silica is indicative of surfactant micelles of ellipsoidal shape, while the scattering profile in the presence of silica indicates that the surfactant forms an adsorbed layer on the silica particles. Figure 5.4 also shows that addition of an electrolyte (0.1 M NaBr) to the silica-containing system is causing no significant changes of the scattering profile, indicating that the electrolyte does not affect the adsorption at the silica surface. The profiles in Fig. 5.4 were obtained with silica II at a surfactant concentration corresponding to a nearly complete adsorbed layer ($7/8 \Gamma_{\text{mx}}$), but analogous results were found with silica I in the absence and presence of 0.1 M NaBr. The absence of a salt effect on the adsorption is expected because at the given pH C₁₂DAO behaves as a nonionic surfactant with negligible degree of protonation [5.13].

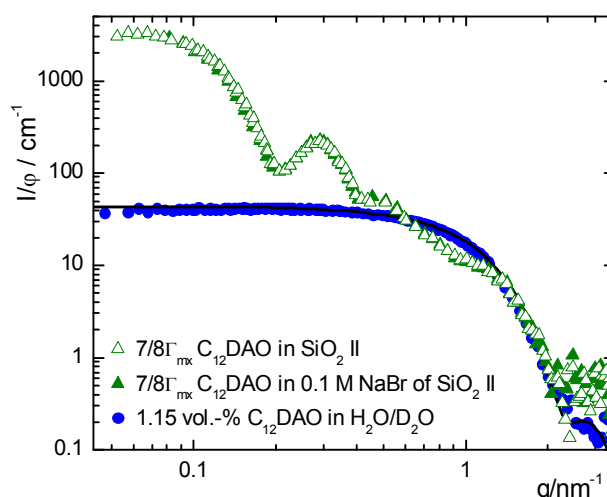


Figure 5.4. SANS profiles $I(q)$ for C_{12} DAO in the contrast matching H_2O/D_2O in the absence and presence of silica II. Also shown is the scattering profile for the silica containing system with added 0.1 M NaBr. The scattered intensities were normalized with volume fraction ϕ of the surfactant in the system.

Scattering profiles for different surface concentrations of the surfactant ($\frac{1}{4}\Gamma_{mx}$, $\frac{1}{2}\Gamma_{mx}$, $\frac{3}{4}\Gamma_{mx}$ and $\frac{7}{8}\Gamma_{mx}$) on silica I and II, and for $\frac{7}{8}\Gamma_{mx}$ on silica III are presented in Fig. 5.5. The concentrations of the silica in the aqueous dispersions is 0.77 vol-% (silica I); 1.52 vol-% (silica II); and 0.36 vol-% (silica III). Values of the surface concentration Γ of surfactant on the silica are based on the adsorption isotherm of C_{12} DAO on Davisil silica gel reported by Pettersson and Rosenholm [5.13]. According to that work, the adsorbed amount reaches a plateau value of the surface concentration, $\Gamma_{mx} = 7.5 \mu\text{mol m}^{-2}$, at a concentration of the solution somewhat above the CMC ($CMC \approx 2 \times 10^{-3} \text{ M}$), and the surface concentration at the CMC is $\frac{7}{8}\Gamma_{mx}$. This value was chosen as the highest surface concentration of the surfactant on the silicas, in order to avoid free micelles in the solution. Therefore, most of the surfactant in the system is adsorbed and only a small fraction exists in solution in monomeric form.

Qualitatively, all scattering profiles are similar to those for C_{12} DAO on silica II shown in Fig. 5.4, but significant differences in detail can be found, as will be shown below. Figure 5.5 shows that the position of the local maximum (q_{max}) in the scattering profiles (indicated by the vertical lines) is not affected by the surface concentration of the surfactant but moves to lower q as the particle size increases from silica I to silica III ($q_{max} \approx 0.42 \text{ nm}^{-1}$ for silica I, 0.30 nm^{-1} for silica

II, and 0.20 nm^{-1} for silica III). For silica I and silica II it can also be seen that the overall scattering intensity as well as the relative height of the maximum at q_{max} increases with the surface concentration of C_{12}DAO . In all cases, the behaviour at the high- q end of the scattering profiles conforms to Porod's law.

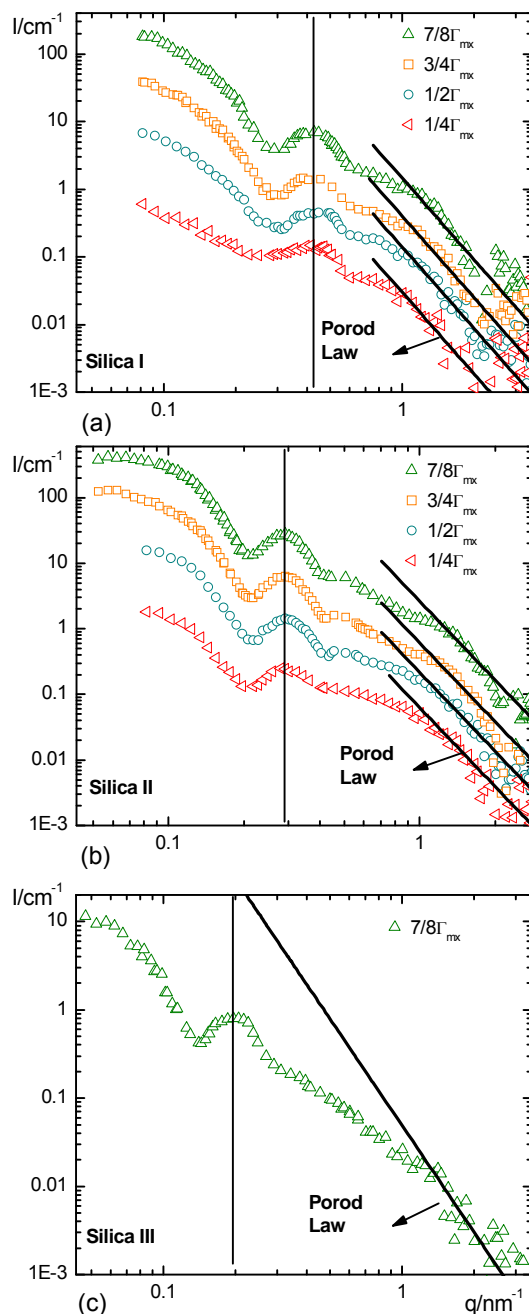


Figure 5.5. SANS profiles for silica sols of different particle sizes in contrast-matching $\text{H}_2\text{O}/\text{D}_2\text{O}$ (pH 9, 298 K) in the presence of different amount of C_{12}DAO , corresponding to surface concentration $\frac{7}{8}\Gamma_{\text{mx}}$, $\frac{3}{4}\Gamma_{\text{mx}}$, $\frac{1}{2}\Gamma_{\text{mx}}$ and $\frac{1}{4}\Gamma_{\text{mx}}$: (a) silica I; (b) silica II; (c) silica III. In (a) and (b) the curves for higher surface concentrations are shifted vertically relative to that of $\frac{1}{4}\Gamma_{\text{mx}}$ by factors of 2 ($\frac{1}{2}\Gamma_{\text{mx}}$), 4 ($\frac{3}{4}\Gamma_{\text{mx}}$) and 14 ($\frac{7}{8}\Gamma_{\text{mx}}$).

The analysis of the SANS profiles was made in two steps: Initially, simple geometrical modelling was used to estimate the volume, effective layer thickness and volume-based surface area of the adsorbed C₁₂DAO. In the second step, nonlinear least-squares fitting of the scattering data to appropriate structure factor models was employed in order to extract information about the size and shape of the surface aggregates.

5.2.3 Geometric Modelling

A model-free analysis of the Guinier and Porod regimes of $I(q)$ in terms of the dry volume, layer thickness, and volume-based surface area of the adsorbed surfactant was performed as a basis for simple geometrical models of the surface aggregates.

The Guinier expression $I(q) = I_0 \exp(-R_g^2 q^2/3)$ can be used to fit the data in the low- q region. For example, for silica II ($R_G = 15.8$ nm) we find a radius of gyration $R_g = 17.3$ nm at the highest surface concentration ($7/8 \Gamma_{mx}$). In the contrast-match scenario of our experiment, R_g must have a value between the silica radius R_G and $R_G + \delta$, depending on the surfactant density profile. Assuming for simplicity that R_g is half-way between these two values, a typical layer thickness of the adsorbed surfactant is $\delta = 2 \cdot (17.3 - 15.8) = 3$ nm. From the high- q region (Porod regime) we obtain the volume-based surface area S/V of the surface aggregates, since the concentration of free micelles in solution is negligible at the chosen surfactant concentrations. The respective value for free micelles can be derived from the scattering profile of the surfactant in the absence of silica (Fig. 5.4). One finds that S/V for the free micelles is about 10% lower than for the surface aggregates. The similar magnitude of the two values implies similar morphologies of the surfactant aggregates in solution and on the surface. This excludes adsorbed half-micelles [5.13], which would require considerably more surface area.

For non-interacting particles, the dry volume of adsorbed C₁₂DAO per silica bead, V_{dry} , can be derived from the scattering cross section at zero angle by the relation $I_0 = \varphi \Delta \rho^2 V_{dry}$, where $\varphi = 0.00891$ is the volume fraction of C₁₂DAO in the dispersion and $\Delta \rho = 3.72 \times 10^{-4}$ nm⁻² is the scattering contrast between

surfactant and background. From V_{dry} and the mean particle radius $\langle R_S \rangle$ (Table 5.2) one can determine the effective layer thickness δ of dry surfactant. Values of V_{dry} and δ derived from the SANS data in this way are given in Table 4. They are compared with values estimated from the adsorption isotherm of Pettersson [5.13], using the mass densities 0.88 g cm^{-3} (pure C_{12}DAO) and 2.20 g cm^{-3} (silica), and the values of the mean surface area per silica particles $\langle A_S \rangle$ (Table 5.2). Reasonable agreement between the two sets of values is found for most samples, but large deviations appear for the sample with silica III. The results in Table 5.4 indicate that at surface concentrations up to $\frac{1}{2}\Gamma_{\text{mx}}$, the effective layer thickness δ is significantly smaller than the extended tail length of C_{12}DAO ($l_c = 1.67 \text{ nm}$) [5.22] while at surface concentrations above $\frac{1}{2}\Gamma_{\text{mx}}$, the layer thickness approaches l_c . This suggests the existence of either a monolayer (which is physically implausible at hydrophilic surfaces) or patches of bilayer [5.23]. Simple geometric modeling based on surface area and volume of adsorbed surfactant (from the Porod constant and l_0 , respectively) indicates that these patches must have dimensions close to micelles. The possibility of discrete surface micelles as reported recently [5.5, 5.6, 5.7] thus appears plausible. On the assumption that the volume of such surface micelles is similar to that of micelles in solution, the number of surface micelles N_{mic} can be estimated by dividing the dry volume of adsorbed surfactant by the volume of a free micelles. Values of N_{mic} obtained in this way are given in Table 5.4.

5.2.4 Core-Shell Model

The spherical core-shell model [5.3, 5.7, 5.24] was adopted to see if the scattering profiles are consistent with a laterally homogeneous surfactant layer. Three different values of the layer thickness (1.6, 3.2, and 4.0 nm) were tested in the modeling of the data for high surface concentrations of C_{12}DAO : The first value corresponds to the effective thickness, δ_{eff} , as obtained for high surface concentrations from the simple geometric analysis (Table 5.4); the second value is the expected bilayer thickness, *i.e.* twice the monolayer thickness, and the third value represents the mean thickness of a bilayer of C_{12}E_5 at the surface of silica I [5.7]. A fit of the data for the surface concentration $\frac{7}{8}\Gamma_{\text{mx}}$ on silica II with

the three values of layer thickness is shown in Figure 5.6. In these fits the polydispersity in radius of the silica particles is taken into account as explained in our earlier work [5.7].

Table 5.4. Characteristics of the surfactant layer adsorbed at the silica nanoparticles derived from the SANS data and from the adsorption isotherm*.

Sample	SANS			Adsorption Isotherm	
	$V_{dry} (10^3 \text{ nm}^3)$	$\delta(\text{nm})$	N_{mic}	$V_{dry} (10^3 \text{ nm}^3)$	$\delta(\text{nm})$
Silica I					
$\frac{1}{4}\Gamma_{mx}$	0.16	0.18	4	0.42	0.47
$\frac{1}{2}\Gamma_{mx}$	0.70	0.76	17	0.84	0.90
$\frac{3}{4}\Gamma_{mx}$	1.51	1.50	36	1.26	1.28
$\frac{7}{8}\Gamma_{mx}$	1.74	1.69	42	1.47	1.47
Silica II					
$\frac{1}{4}\Gamma_{mx}$	0.91	0.39	22	1.14	0.48
$\frac{1}{2}\Gamma_{mx}$	2.29	0.93	55	2.28	0.93
$\frac{3}{4}\Gamma_{mx}$	3.28	1.34	81	3.43	1.36
$\frac{7}{8}\Gamma_{mx}$	3.98	1.55	101	4.00	1.56
Silica III					
$\frac{7}{8}\Gamma_{mx}$	6.20	1.06	150	9.67	1.62

*dry volume V_{dry} and effective thickness δ of the adsorbed C_{12} DAO layer; N_{mic} is the number of surface micelles

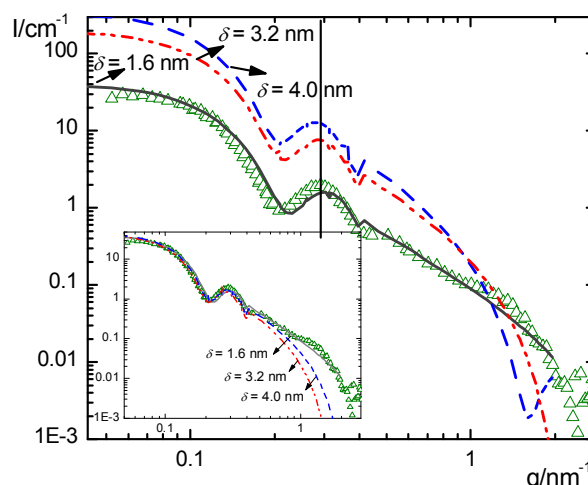


Figure 5.6. Experimental SANS profiles $I(q)$ and intensities predicted by the spherical core-shell model with shell thicknesses $\delta = 1.6, 3.2$ and 4.0 nm for surface concentration $\frac{7}{8}\Gamma_{mx}$ of C_{12} DAO on silica II in contrast matching H_2O/D_2O . The inset shows the predicted intensities with thickness 3.2 and 4.0 nm multiplied with scale factors $f = 0.22$ and 0.12 , respectively.

The fits based on the expected layer thickness δ (3.2 nm) or a greater thickness (4.0 nm) exhibit similar features as noted in the preceding studies with the surfactants Triton X-100 [5.5] and $C_{12}E_5$ [5.7]: The model gives a good fit to the scattering data in the low- q regime including the maximum at intermediate q , if the theoretical intensities are multiplied by a scale factor $f = 0.22$ ($\delta = 3.2$ nm) or $f = 0.12$ ($\delta = 4.0$ nm) (*cf.* inset Fig. 5.6). As the scattered intensity is proportional to the surfactant volume on each bead, this implies that the core-shell model with such a film thickness considerably overestimates the adsorbed surfactant volume. On the other hand, a fit with the layer thickness $\delta_{\text{eff}} = 1.6$ nm reproduces all features of $I(q)$ without any scale factor f , except for the shoulder at $q \approx 1.0 \text{ nm}^{-1}$, causing some underestimate of the specific surface area of adsorbed surfactant. In addition, the maximum in $I(q)$ appears at somewhat too high q , indicating that the real value of the average layer thickness should be greater than 1.6 nm. The agreement with the experimental data for the film thickness 1.6 nm is of course related to the fact that in this case the volume of adsorbed surfactant is conserved. However, although the core-shell model with a layer thickness 1.6 nm gives a good representation of the scattered intensities, the result is unrealistic because this value of δ corresponds to only about half the thickness expected for a bilayer of $C_{12}\text{DAO}$ at the solid/solution interface. Results similar to those shown in Fig. 5.6 were also obtained for lower surface concentrations of $C_{12}\text{DAO}$ on silica II and for the adsorption of $C_{12}\text{DAO}$ on silica I.

The shortcomings of the core-shell model suggest that the adsorbed surfactant does not form a laterally uniform layer but smaller surface aggregates, such as spherical or ellipsoidal surface micelles, which have a higher surface area at a given total adsorbed volume. Accordingly, models of silica particles decorated with such small surface micelles were applied to the present data, as described below.

5.2.5 Micelle-Decorated Silica Model

In previous publications [5.5-5.7] we have developed and applied a form factor model for objects made of small spherical micelles adsorbed on an indexed-

matched silica bead. Parameters of the model are the radius of the silica bead R_S , the radius of spherical surface micelles R_{mic} , and number of surface micelles N_{mic} per silica particle, as well as a polydispersity parameter. Polydispersity of the silica bead is accounted for by performing the calculation for silica radii drawn from a distribution function, and averaging. For a given silica bead of radius R_S , the micelle centers are supposed to sit on a spherical shell of radius $R_S + R_{mic}$. The excluded volume of the spherical micelles is determined by their radius R_{mic} , which also acts as a lateral interaction parameter for spheres. It is assumed that the number density of spheres in the layer is independent of bead radius and that N_{mic} corresponds to the number of micelles on a bead of average radius. The algorithm consists of the following steps: (i) positioning the micelles in a random manner on the shell, possibly allowing for lateral reorganization following a Monte Carlo motion; (ii) calculation of the micelle-micelle structure factor using the Debye formula; (iii) calculation of the scattered intensity in absolute units; and (iv) convolution with the resolution function of the spectrometer.

In order to check if a model of *spherical* micelles is consistent with the data, their radius and number was estimated directly from the scattering curves. The micellar radius must be approximately half the thickness of the layer, and N_{mic} and R_{mic} are related by volume conservation to the amount of adsorbed surfactant as determined either by the adsorption isotherm or by the low- q fit of the core-shell model with factor f . Similarly, the amount of surface produced by N_{mic} spheres of radius R_{mic} must match the volume-related surface area determined from Porod's law. This constrains the model considerably, and parameters can only be varied in a narrow range.

Fitting of the scattered intensities with this model and the estimation of the real adsorbed surfactant volume, V_{tot} , was based on the results of the core-shell model for the layer thicknesses $\delta = 3.2$ and 4.0 nm. The real adsorbed surfactant volume was determined by introducing the effective volume fraction of surfactant in the shell, X (*i.e.*, fraction of the layer volume occupied by the surfactant), which is related to the scale factor f by $X = \sqrt{f}$. For example, for silica II at the surface concentration $\frac{7}{8}\Gamma_{mx}$, the scale factor $f = 0.22$ introduced

for the layer thickness 3.2 nm implies that only 47% of the layer volume is occupied by C₁₂DAO. The total surface area of the adsorbed surfactant, A_{tot} , was calculated from the volume-related surface area of adsorbed surfactant as determined by Porod's law, $(S/V)_{\text{surf}} = A_P/2\pi\Delta\rho^2$, and the number density of silica beads, $(N/V)_S = \phi/\langle V_S \rangle$, by the relation $A_{\text{tot}} = (S/V)_{\text{surf}}/(N/V)_S$.

The number and dimensional parameters of surface aggregates of different morphologies were estimated from the real volume, V_{tot} , and total surface area, A_{tot} , of adsorbed surfactant. The dimensional parameters of surface aggregates of given shapes depend strongly on the layer thickness δ used to calculate V_{tot} . At first we assumed the formation of isolated spherical aggregates of radius R_{mic} and number of micelles N_{mic} . In most cases a fits with a layer thickness $\delta = 4.0$ nm (*i.e.*, a value similar to that found by the Guinier approximation, Section 5.2.3) gave a somewhat better fit than with $\delta = 3.2$ nm, although the difference was within a 5% in most cases. Results for fixed $\delta = 4.0$ nm are summarized in Table 5.5. A noteworthy finding is that the number of surface aggregates estimated by this model (N_{mic}) is similar to that obtained by the simple geometrical analysis (N_{mic} , *cf.* Section 5.2.3). This indicates that the simple geometric analysis gives reliable information about the morphologies of the surface aggregates.

Table 5.5. Parameters of the micelle-decorated silica model for C₁₂DAO on silica particles.*

Sample	R_{mic} (nm)	N_{mic}
Silica I (spherical)		
$\frac{1}{2}\Gamma_{\text{mx}}$	1.63	38
$\frac{3}{4}\Gamma_{\text{mx}}$	1.97	36
$\frac{7}{8}\Gamma_{\text{mx}}$	1.97	42
Silica II (oblate)		
$\frac{1}{4}\Gamma_{\text{mx}}$	1.47 / 2.20	26
$\frac{1}{2}\Gamma_{\text{mx}}$	1.47 / 2.20	55
$\frac{3}{4}\Gamma_{\text{mx}}$	1.47 / 2.20	87
$\frac{7}{8}\Gamma_{\text{mx}}$	1.47 / 2.20	94
Silica III (oblate)		
$\frac{7}{8}\Gamma_{\text{mx}}$	1.47 / 2.20	155

* Silica I: Best-fit values of R_{mic} and N_{mic} for spherical surface micelles. Silica II and silica III: best-fit values of N_{mic} for oblate ellipsoidal surface micelles of fixed values of R_n and R_{lat}

C₁₂DAO on silica I. Figure 5.7 shows the scattering data for C₁₂DAO on silica I at the surface concentrations $\frac{3}{4}\Gamma_{\text{mx}}$ and $\frac{7}{8}\Gamma_{\text{mx}}$, and fits with the micelle-decorated silica model. In this case, a good fit of the scattering profile was obtained by assuming that C₁₂DAO is adsorbed in form of isolated spherical surface micelles of radius $R_{\text{mic}} = 2.0$ nm. The good representation of the data in the high- q region supports the conjectured uniform size of the surface aggregates, and the fit of the data at intermediate q indicates that the increasing amplitude of the maximum at q_{max} can be explained by an increasing number of surface aggregates as the surface concentration is increased (*cf.* Table 5.5). Some deviations between the experimental and predicted $I(q)$ appear in the q regime just below q_{max} , where the model somewhat overestimates the total volume of the adsorbed surfactant aggregates (see Fig. 5.5). The strong increase of $I(q)$ at the lower end of the experimental q range is a hint of a maximum in $I(q)$ at lower q , which was not captured because measurements at smaller angles were not performed for this silica. Such a maximum indicates repulsive interaction between the silica beads coated with small surface aggregates of C₁₂DAO. The quality of the fit of the low- q region could not be improved by decreasing N_{mic} , the number of surface micelles, at fixed radius $R_{\text{mic}} = 2.0$ nm (*cf.* Table 5.5), since this implies a decrease in the surfactant volume fraction in the layer and thus lowers the amplitude of the maximum at q_{max} , which is inconsistent with the experimental $I(q)$. Similarly, no better fit was found when R_{mic} was increased at a fixed value of N_{mic} .

C₁₂DAO on silica II and III. The scattering data for C₁₂DAO on silica II and III were also analysed in terms of the model of spherical surface aggregates. However, for these silicas reasonable fits with spherical surface micelles could be obtained only by adopting unrealistic values of the micelle radius R_{mic} . Specifically, with silica II a surface micelle radius $R_{\text{mic}} = 0.85$ nm was obtained for low surface concentrations ($\frac{1}{4}\Gamma_{\text{mx}}$, and $\frac{1}{4}\Gamma_{\text{mx}}$) and an even lower value ($R_{\text{mic}} = 0.66$ nm) for higher surface concentrations ($\frac{3}{4}\Gamma_{\text{mx}}$, and $\frac{7}{8}\Gamma_{\text{mx}}$). These values of R_{mic} are physically unrealistic as they are less than half the length of an extended surfactant molecule. For this reason, model calculations similar to those described above were also made for surface aggregates of different

geometries, viz., patch-like, ellipsoidal and wormlike micelles. The most acceptable morphology was oblate ellipsoids, with now two structural parameters, R_n and R_{lat} , which also define the orientation of the micelle on the surface: the minor semi-axis R_n is the axis in the direction perpendicular to the surface and defines the height of the micelle center above the silica surface. The major semi-axis R_{lat} characterizes the lateral extension of the oblate surface micelles on the surface. It is assumed that the surface aggregates interact only through excluded volume interactions. The positioning of the micelles is then performed as with the spherical micelles, and again the Debye formula is employed to determine the micelle-micelle structure factor.

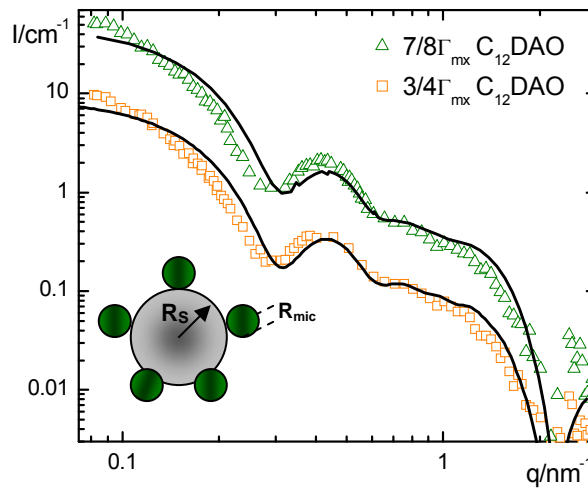


Figure 5.7. SANS profiles $I(q)$ for silica I with adsorbed $C_{12}DAO$ (surface concentrations $7/8\Gamma_{mx}$ and $3/4\Gamma_{mx}$) and fits by the micelle-decorated silica model (solid curves) for spherical surface micelles of radius 2 nm (parameters see Table 5.5). Results for surface concentration $7/8\Gamma_{mx}$ are shifted relative to that for $3/4\Gamma_{mx}$ by factor of 4.

A subtlety of this procedure is that at first sight it seems to be incorrect, as it uses the formalism of separation into form factor and structure factor which is valid only for monodisperse objects of spherical symmetry. We show in Section 5.2.6 that it can be used in our case to calculate the scattered intensity, as before with resolution function.

The evidence for non-spherical surface micelles of $C_{12}DAO$ on silica nanoparticles suggested a comparison with the micelle shape in solution. A comparison of the scattering curves of $C_{12}DAO$ in H_2O/D_2O in the absence and presence of silica II is shown in Figure 5.4. The data for the aqueous solution of

C₁₂DAO can be represented by a model of oblate ellipsoids, with $a = 1.41$ nm and $b = 2.15$ nm (where a is the rotational semi-axis and b the equatorial semi-axis of the ellipsoid core). The model of oblate micelles fits the data at high q somewhat better than the prolate ellipsoidal model (fit not shown), as indicated by the lower residual, which was ~ 1.2 for the oblate ellipsoid, but ~ 1.6 for the prolate ellipsoid. Figure 5.4 also shows that the scattering curves of C₁₂DAO in the absence and presence of the silica overlap in the high- q region, indicating that the shape of the micelles in solution and at the surface is similar. Accordingly, the parameters R_n and R_{lat} of the surface micelle model were set to 1.5 nm and 2.2 nm, respectively, for all surface concentrations and the number of micelles, N_{mic} was taken as the only adjustable parameter. Fits for C₁₂DAO on silica II and silica III are shown in Figure 5.8. The good fit of the data in the entire q range supports the chosen model of isolated oblate surface micelles. Furthermore, the values of N_{mic} derived from the fits (Table 5.5) are similar to those found in the simple geometric analysis (Table 5.4).

To gain a better understanding of the way in which the calculated scattering function is influenced by the structural parameters R_n and R_{lat} we have varied them in a systematic manner, keeping one of them (and N_{mic}) fixed and varying the value of the other in a range from 0.5 to 3.5 nm, as shown in Figure 5.9 for the scattering profile of $\frac{7}{8}\Gamma_{mx}$ of C₁₂DAO on silica II. Figure 5.9a shows the effect of a variation of R_n , at fixed $R_{lat} = 2.2$ nm and $N_{mic} = 94$. As can be seen, R_n is directly related to the size of the ellipsoidal aggregates because decreasing its value to 0.5 nm or increasing its value to 3.5 nm causes a shift of q_{max} to higher or lower values. R_{lat} is related to the ordering of the micelles on the surface. This is indicated in Fig. 5.9b by the fact that a decrease of R_{lat} from 2.2 to 0.5 nm causes a deformation of the size of the surface aggregates as their shell is no longer well defined. By increasing R_{lat} to 3.5 nm a strong oscillation appears at $q \approx 1.3$ nm⁻¹, indicating intermicellar repulsion between the adsorbed surface aggregates (see also Figs. 6 and 7 in ref. 5.6).

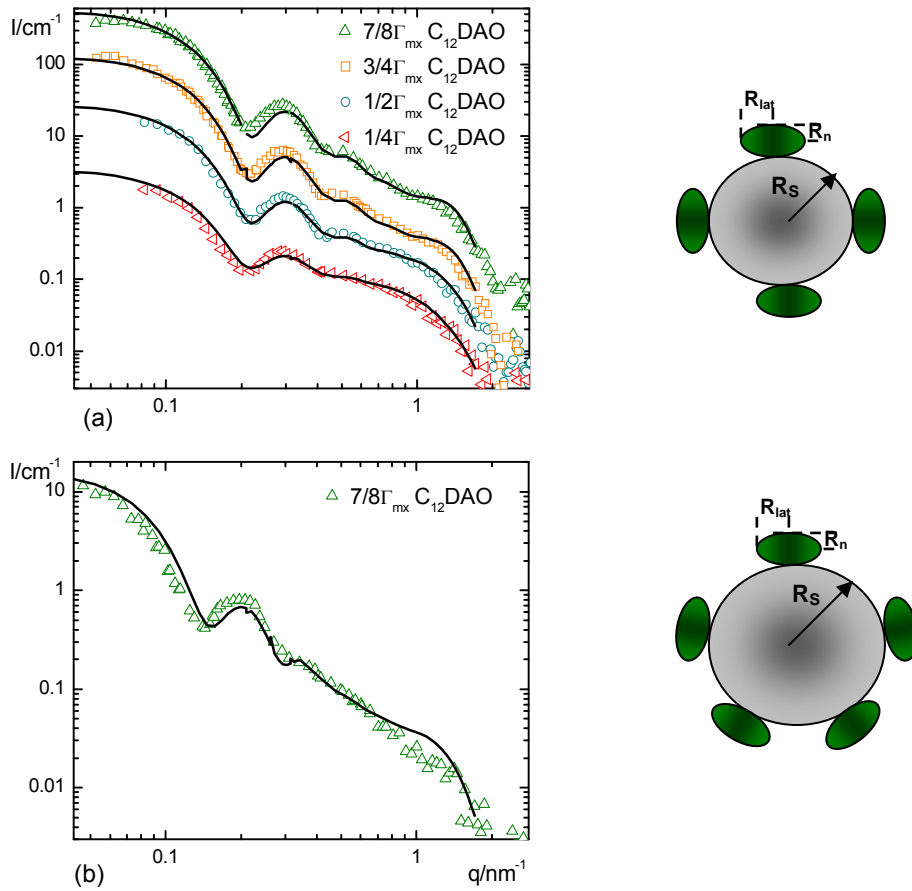


Figure 5.8. SANS profiles $I(q)$ for silica II and silica III with adsorbed $C_{12}DAO$ in contrast-matching H_2O/D_2O and fits by the micelle-decorated silica model for ellipsoidal micelles (solid curves): (a) silica II at surface concentrations $1/4\Gamma_{mx}$, $1/2\Gamma_{mx}$, $3/4\Gamma_{mx}$ and $7/8\Gamma_{mx}$; (b) silica III with surface concentrations $7/8\Gamma_{mx}$ of $C_{12}DAO$ (parameters see Table 5.5). In (a) the curves for higher surface concentrations are shifted vertically relative to that of $1/4\Gamma_{mx}$ by factors of 2 ($1/2\Gamma_{mx}$), 4 ($3/4\Gamma_{mx}$) and 14 ($7/8\Gamma_{mx}$). On the right side is shown a schematic representation of a silica bead decorated with oblate ellipsoidal micelles

5.2.6 Scattering from index-matched silica particles decorated with ellipsoidal micelles

Micelles adsorbed on the surface of a sphere are confined to a spherical shell. Correlations between their centers of mass are generated by excluded volume and possibly other interactions between the micelles. In our experiments, silica nanoparticles are index-matched, *i.e.*, they do not contribute to the signal. Scattering from interacting spherical micelles can be factorized in a product of form and structure factor:

$$I(q) = \frac{N}{V} S(q) P(q) \quad (5.2)$$

where $P(q)$ is the form factor related to the scattering amplitude $F(q)$, which is the Fourier transform of the scattering length density distribution, by

$$P(q) = \langle |F(q)|^2 \rangle = |\langle F(q) \rangle|^2 \quad (5.3)$$

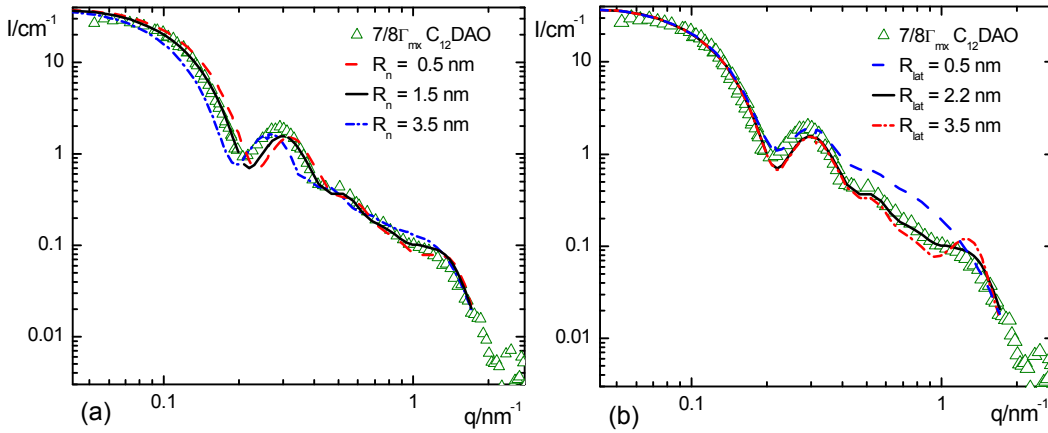


Figure 5.9. Scattering profile for C_{12}DAO (surface concentration $7/8\Gamma_{\text{mx}}$) on silica II and results predicted by the micelle-decorated silica model for ellipsoidal surface micelles: (a) varying the normal semi-axis R_n , at fixed $R_{\text{lat}} = 2.2 \text{ nm}$ and $N_{\text{mic}} = 94$; (b) varying the lateral semi-axis R_{lat} , at fixed $R_n = 1.5 \text{ nm}$ and $N_{\text{mic}} = 94$.

The last equality is a direct consequence of spherical symmetry, the average being (also) a rotational one. The case of interacting ellipsoidal micelles can be deduced in the same way as equation (5.2) by simply keeping $\langle |F(q)|^2 \rangle$ and $|\langle F(q) \rangle|^2$ separate:

$$I(q) = \frac{N}{V} \left[S(q) |\langle F(q) \rangle|^2 + \langle |F(q)|^2 \rangle - |\langle F(q) \rangle|^2 \right] \quad (5.4)$$

In order to see if the simpler factorization can be used, it is thus necessary to calculate $\langle |F(q)|^2 \rangle$ and $|\langle F(q) \rangle|^2$. In the Figure 5.10, the result for an isolated oblate ellipsoid at 1 vol.-%, with a contrast of $\Delta\rho_D = 5.1 \times 10^{10} \text{ cm}^{-2}$, is shown.

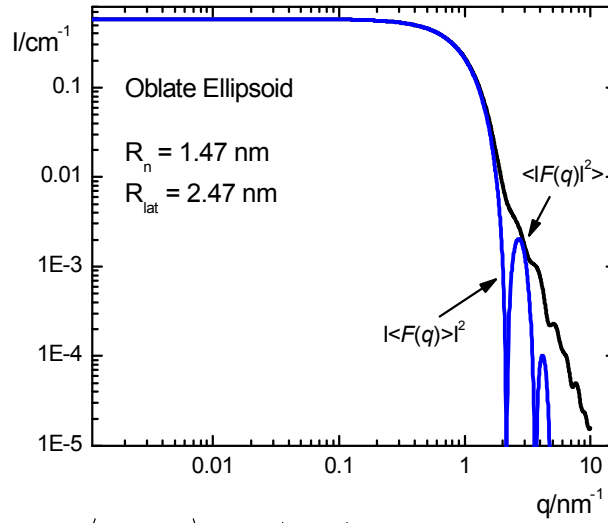


Figure 5.10. Comparison of $\langle |F(q)|^2 \rangle$ and $|\langle F(q) \rangle|^2$ for isolated oblate ellipsoids.

As can be seen in Figure 5.10, $\langle |F(q)|^2 \rangle$ and $|\langle F(q) \rangle|^2$ coincide for small angles ($q < 1.5 \text{ nm}^{-1}$), but differences appear at $q > 1.5 \text{ nm}^{-1}$ due to stronger oscillations of the square of the average of the amplitude $F(q)$. One thus has to discuss the low- q and high- q regions separately:

- At low q , the two functions are the same, and equation (5.4) reduces to (5.2).
- At high q , the structure factor tends to one, and equation (5.4) reduces to the measured form factor scattering $P(q) = \langle |F(q)|^2 \rangle$.

Given that the maxima of $S(q)$ in our experimental case are located well below 1 nm^{-1} , and Porod surface (*i.e.* form factor) scattering is observed above 1.5 nm^{-1} , it is clear that $S(q) = 1$ in this high- q range. Thus, equation (5.2) can be safely used with the experimentally measured form factor for ellipsoidal micelles of typical size 1.5 to 2.5 nm, adsorbed and interacting on the surface of an indexed-matched silica sphere of much larger radius. Limits of this approach may be a weaker separation in length scales, *e.g.* caused by a very high surface density of ellipsoidal micelles, which is not the case here. Note that we have applied such calculations to the similar case of interacting cylindrical (albeit non adsorbed) micelles [5.25].

5.2.7 Influence of the surfactant head group

Aggregate structures of surfactants in solution can often be predicted on the basis of the critical packing parameter $V/l_c a_0$, which expresses the preferred interface curvature of the aggregate in terms of molecular parameters alkyl chain volume V , the alkyl chain length l_c and the head group area a_0 [5.26]. C₁₂DAO in its cationic form at low pH is expected to have a higher effective head group area than in its nonionic form at high pH where the absence of electrostatic head group repulsion allows a closer packing of the head groups. Hence it should be possible to study the effect of head group size on the shape of surface aggregates simply by changing pH. However, this is not possible in the present case because pH has to be fixed near pH 9 to prevent flocculation of the silica dispersion. We have checked that added electrolyte has no effect on the morphology of the adsorbed layer of C₁₂DAO (Figure 5.4) under the experimental conditions, as expected for nonionic surfactants. It would be of interest to study the effect of electrolyte on the surfactant aggregates in the cationic form of the surfactant, but again this is not possible at the given pH of the system.

In our earlier study [5.7], spherical surface aggregates were observed for the surfactant C₁₂E₅ on silica I, in line with the large head-group size of this molecule. Since C₁₂DAO has a much smaller head group than C₁₂E₅, one expects that surface aggregates of smaller curvature are preferred for this surfactant. This conjectured behavior is indeed found for C₁₂DAO on silica II and III, where we find oblate-shaped surface aggregates. On the other hand, spherical surface aggregates of C₁₂DAO are found on silica I, and they have similar dimensions as those of C₁₂E₅ on silica I. These findings suggest that the head group size (or packing parameter) of the surfactant is not the dominating factor for the *shape* of surface aggregates on the silica particles. However, the nature of the surfactant head group may have a pronounced influence on *the number of surface aggregates* per particle (N_{mic}). This is suggested by a comparison of the results for C₁₂DAO on silica I with the earlier results for C₁₂E₅ on the same silica [5.7]. For instance, at a surface concentrations $\frac{3}{4}\Gamma_{\text{mx}}$ we find $N_{\text{mic}} = 36$ for C₁₂DAO (Table 5.4), but $N_{\text{mic}} = 72$ for C₁₂E₅ [5.7]. The larger

number for $C_{12}E_5$ may be attributed to its ability to form more than one strong hydrogen bond to surface silanol groups. However, other factors may also affect the number of surface aggregates, as is suggested by the fact that rather small numbers of surface aggregates (N_{mic} up to 15) were found in the study of Triton X-100 (a technical-grade alkylphenyl polyoxyethylene surfactant) on a commercial silica sol (Bindzil B30). Since Triton X-100 is similar to $C_{12}E_5$ and the mean particle size of Bindzil B30 ($R_S = 7.7$ nm) is similar to that of silica I, the large difference in N_{mic} between these two systems is not clear.

5.2.8 Influence of the nanoparticle size

An interesting finding of this study is the morphological transition from spherical to ellipsoidal shape of the surface aggregates. This transition must be caused by some property of the silica particles, either their surface chemistry or surface roughness, or the particle size. Since silica I and silica II were prepared by the same method, their surface properties are similar, as indicated by the similar zeta potentials (Table 5.1) and surface roughness (a_s/a_{geom} in Table 5.3) of these two samples, when compared to silica III. Because the transition in surface aggregate shape occurs from silica I to silica II, we may conclude that it is not induced by changes in surface properties but by the increase in particle size. In the preceeding study we conjectured that the formation of spherical surface aggregates of $C_{12}E_5$ on silica I was caused by the high surface curvature of the silica nanoparticles, which prevents an effective packing of the hydrophobic tails of the molecules in a bilayer configuration. This argument may be generalized by noting that the formation of surface aggregates at concentrations below the *CMC* depends on favorable interactions of the surfactant heads with the solid surface, and that the morphology of the surface aggregates will be determined by a balance of amphiphile-amphiphile (A-A) and amphiphile-surface (A-S) interactions. At weakly convex surfaces (large silica particles), micellar aggregates of relatively low mean curvature can have favourable A-S interactions without significant changes in aggregate structure, *i.e.* without sacrificing A-A interaction energy. This appears to be the situation for the oblate-shaped surface micelles of $C_{12}DAO$ on silica II and silica III. On

the other hand, at highly convex surfaces (small silica particles), optimization of the A-A and A-S interactions may favor smaller surface aggregates, if that leads to a larger number of surface contacts per unit area of the solid particle – even at the cost of a higher A-A bending energy. This seems to be the situation for C₁₂DAO on silica I. The transition from spherical to oblate shape of the surface aggregates can then be seen as a relaxation from a strained to an unstrained curvature of the surface aggregates, since oblate micelles represent the favored aggregate shape of C₁₂DAO in the bulk solution. The present work suggests that this morphological transition occurs at a particle radius $R_S \approx 10\text{--}12\text{ nm}$, *i.e.* $R_{\text{mic}}/R_S \approx 0.2$. To our knowledge, no theoretical model for this morphological transition exists in the literature, but such a model would be most valuable for gaining a better understanding of this phenomenon.

References of Chapter 5

- [5.1] Dietsch, O.; Eltekov, A.; Bock, H.; Gubbins, K.E.; Findenegg, G.H. *J. Phys. Chem. C* **2007**, *111*, 16045–16054.
- [5.2] (a) Grant, L.M.; Tiberg, F.; Ducker, W.A. *J. Phys. Chem. B* **1998**, *102*, 4288–4294. (b) Grant, L. M.; Ederth, T.; Tiberg, F. *Langmuir* **2000**, *16*, 2285–2291. (c) Blom, A.; Duval, F. P.; Kovács, L.; Warr, G. G.; Almgren, M.; Kadi, M.; Zana, R. *Langmuir* **2004**, *20*, 1291–1297.
- [5.3] (a) Cummins, P.G.; Staples, E.; Penfold, J. *J. Phys. Chem.* **1990**, *94*, 3740–3745. (b) Cummins, P.G.; Staples, E.; Penfold, J. *J. Phys. Chem.* **1991**, *95*, 5902–5905. (c) Cummins, P.G.; Penfold, J.; Staples, E. *J. Phys. Chem.* **1992**, *96*, 8092–8094.
- [5.4] Penfold, J.; Staples, E.; Tucker, I.; Cummins, P.G. *J. Phys. Chem.* **1996**, *100*, 18133–18137.
- [5.5] Despert, G.; Oberdisse, J. *Langmuir* **2003**, *19*, 7604–7610.
- [5.6] Oberdisse, J. *Phys. Chem. Chem. Phys.* **2004**, *6*, 1557–1561.
- [5.7] Lugo, D.; Oberdisse, J.; Karg, M.; Schweins, R.; Findenegg, G.H. *Soft Matter* **2009**, *5*, 2928–2936.
- [5.8] Li, X.; Lin, Z.; Cai, J.; Scriven, L.A. Davis, H,T *J. Phys. Chem.* **1995**, *99*, 10865–10878.
- [5.9] Menge, U.; Lang, P.; Findenegg, G.H.; Strunz, P. *J. Phys. Chem. B* **2003**, *107*, 1316–1320.
- [5.10] Sterpone, F.; Marchetti, G.; Pierleoni, C.; Marchi, M. *J. Phys. Chem. B* **2006**, *110*, 11504–11510.
- [5.11] (a) Chernik, G. G.; Sokolova, E. P. *J. Colloid Interface Sci.* **1991**, *141*, 409–414. (b) Benjamin, L. *J. Phys. Chem.* **1964**, *68*, 3575–3581. (c) Kresheck, G. C. *J. Am. Chem. Soc.*

- 1998**, 120, 10964-10969. (d) Timmins, P. A.; Hauk, J.; Wacker, T.; Welte, W. *Febs Letters* **1991**, 280, 115-120. (e) Timmins, P. A.; Leonhard, M.; Weltzien, H. U.; Wacker, T.; Welte, W. *Febs Letters* **1988**, 238, 361-368. (f) Barlow, D. J.; Lawrence, M. J.; Zuberi, T.; Zuberi, S. *Langmuir* **2000**, 16, 10398-10403.
- [5.12] Király, Z.; Findenegg, G. H. *Langmuir* **2000**, 16, 8842-8849.
- [5.13] (a) Pettersson, A.; Rosenholm, J. B. *Langmuir* **2002**, 18, 8436-8446. (b) Pettersson, A.; Rosenholm, J. B. *Langmuir* **2002**, 18, 8447-8454.
- [5.14] Stöber, W.; Fink, A.; Bohn, E. *J. Colloid Interface Sci.* **1968**, 26, 62-69.
- [5.15] Pusey, P.N. in *Neutrons, X-rays and Light: Scattering Methods Applied to Soft Condensed Matter*, **2002**, 1st edn. ed. P. Lindner and Th. Zemb, Elsevier, Boston, chap. 1 pp. 3-21.
- [5.16] Brûlet, A.; Lairez, D.; Lapp, A.; Cotton, J.-P. *J. Appl. Cryst.* **2007**, 40, 165-177; Lindner, P. in *Neutrons, X rays and Light: Scattering Methods Applied to Soft Condensed Matter* **2002**, 1st ed., ed. P. Lindner and Th. Zemb, Boston, chap. 2, pp 23-48.
- [5.17] Oberdisse, J.; Deme, B. *Macromolecules* **2002**, 35, 4397-4405.
- [5.18] Milano-Brusco, J.; Prévost, S.; Lugo, D.; Gradzielski, M.; Schomäcker, R. *New J. Chem.* **2009**, 33, 1726-1735.
- [5.19] Hansen, J.-P.; Hayter, J. B. *Mol. Phys.* **1982**, 46, 651-656; Hayter, J. B.; Penfold, J. *Mol. Phys.* **1981**, 42, 109-118.
- [5.20] Oberdisse, J.; Hine, P.; Pyckhout-Hintzen, W. *Soft Matter* **2007**, 3, 476-485.
- [5.21] Lowell, S.; Shields, J.E.; Thomas, M.A.; Thommes, M. *Characterization of Porous Solids and Powders: Surface Area, Pore Size and Density*, **2004**, Kluwer Academic Publishers, Dordrecht.
- [5.22] Tanford, C. *J. Phys. Chem.* **1972**, 76, 3020-3024.
- [5.23] Holmberg, K.; Jönsson, B.; Kronberg, B.; Lindman, B. *Surfactants and Polymers in Aqueous Solution* **2003**, 2nd ed., John Wiley & Sons.
- [5.24] Pusey, P.N. in *Neutrons, X-rays and Light: Scattering Methods applied to Soft Condensed Matter* **2000**, ed. B.J. Gabrys, Gordon and Breach Science Publishers, Netherlands, 1st ed., chap. 4, pp. 77-102.
- [5.25] Oberdisse, J.; Regev, O.; Porte, G. *Journal of Physical Chemistry B* **1998**, 102, 1102-1108.
- [5.26] Israelachvili, J.N.; Mitchell, D.J.; Ninham, B.W. *J. Chem. Soc. Faraday Trans. 2* **1976**, 72, 1525-1568.

6 Surface Aggregate Structure of Mixtures of Sugar-Based Surfactants with an Amphoteric Surfactant on Silica Beads

6.1 Introduction

The adsorption of surfactants at solid-liquid interfaces plays a crucial role in many important industrial processes. Most of these applications involve use of *surfactant mixtures*, since in many cases mixtures provide a synergistic enhancement in both surface and bulk properties compared to the individual surfactants. This behaviour is observed when there are favourable interactions between the two types of surfactants. On the other hand, this also makes it possible to control the behaviour of surfactants at interfaces and utilize them more efficiently by varying the composition of such mixtures. Towards this purpose it becomes helpful to understand the adsorption and solution behaviour of surfactant mixtures.

The interpretation of the behaviour of surfactant mixtures in solution and at the solid-liquid interface has been focused in thermodynamic models [6.1], in terms of synergistic and antagonistic effects [6.2], and in studies of the adsorption mechanism which may be looked upon either as the formation of adsorbed mixed surfactant aggregates as in the bulk or as an adsolubilization effect [6.3]. However, many aspects of surfactant mixing are not well understood at a molecular level. This has stimulated a resurgence of interest in recent years and has resulted in the application of new experimental techniques to study the structure of adsorbed monolayers of ionic/nonionic and nonionic/nonionic surfactant mixtures at the air-solution interface, such as neutron reflectivity [6.4], optical probes such as second harmonic generation (SHG) [6.5], sum frequency spectroscopy (SFS) [6.6], and atomic force microscopy (AFM) [6.7], to augment more classical techniques, such as surface tension measurements. More recently, these structural studies have been extended to surfactant mixtures at the hydrophilic solid-solution interface, in particular, to study the adsorption of cationic/nonionic and anionic/nonionic mixtures on hydrophilic solid surface by neutron reflectivity [6.8]. Brinck and

Tiberg [6.9] have used ellipsometry to study the adsorption of binary mixtures of nonionic surfactants at the silica/water interface. This technique can provide information about both equilibrium and kinetic aspects of surfactant adsorption at solid surfaces, but is relatively insensitive to the detailed structure of the surface layers. In neither of these studies direct information about the surface aggregate structures formed by binary nonionic surfactant mixtures on colloidal solids has been obtained. Small-angle neutron scattering (SANS) is a powerful tool for studying surfactant adsorption on nanoparticles at a length-scale below 100 nm by using isotopic labeling, through deuterium/hydrogen substitution, and in this way, provides information about adsorbed amount and the structure of the adsorbed layer, as has been demonstrated in previous chapters.

The focus of this chapter is to clarify the nature of mixed surfactant aggregates formed by mixtures of two nonionic surfactants of different adsorption affinity on a colloidal silica sol by using SANS. This study was made with dimethyldodecylamine-*N*-oxide (C_{12} DAO) as the strongly adsorbed surfactant and two alkyl maltosides (β - $C_{10}G_2$) and (β - $C_{12}G_2$) as the weakly adsorbed surfactant. Measurements were made at room temperature (298 K) and at pH 9, where C_{12} DAO behaves as a nonionic surfactant, in order to preserve the colloidal stability of the silica dispersion. The SANS study of the structure of adsorbed surfactant layers on colloidal silica was made in a concentration regime, in which the amount of the preferred surfactant (C_{12} DAO) is not sufficient to cover the silica particles with a complete adsorbed bilayer. In this 'surfactant-deficient' regime the amount adsorbed could be controlled simply by adjusting the overall amount of surfactants in the system. Under these conditions it is possible that the adsorbed C_{12} DAO will incorporate the non-adsorbing maltoside surfactant into the adsorbed layer through hydrophobic interactions, in this way covering the nanoparticles with an *asymmetric surfactant bilayer*, or forming mixed surface aggregates like the mixed micelles formed in aqueous solutions.

6.2 Results and Discussion

6.2.1 Characterization of the silica particles

The surface charge of the silica particles at pH 9 was highly negative and the aqueous silica dispersion at pH 9 was stable due to its large negative zeta potential (-46.9 mV) and high conductivity ($168 \mu\text{S cm}^{-1}$), which implies that the silica particles in suspension will tend to repel each other and the dispersion is electrically stabilized.

The silica nanoparticles were prepared using the Stöber synthesis [6.10]. A first characterization was done by transmission electron microscopy (TEM). The TEM images show that the nanoparticles are nearly spherical, and somewhat monodisperse (Figure 6.1, left). From a Gaussian fit of the particle size distribution histogram of the silica particles it is found that most particles have sizes in a range from 22 to 32 nm with an average particle diameter of 28.5 nm and a standard deviation of 0.053 (Fig. 6.1, right). These values are consistent with the mean particle size obtained from small-angle neutron scattering (SANS, see Table 6.1). TEM and SANS were taken to characterize the silica nanoparticles, because they provide useful complementary information to estimate the particle size distribution.

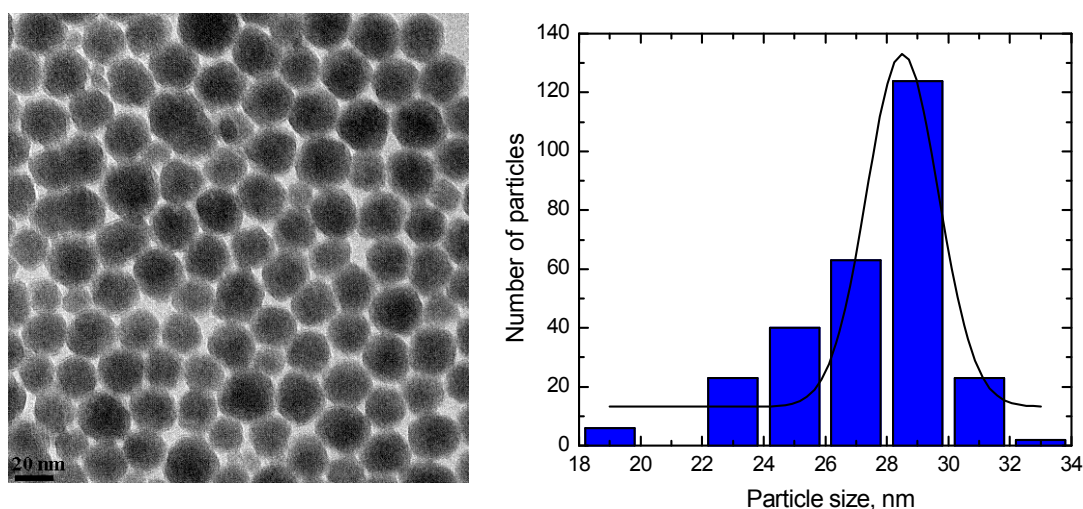


Figure 6.1. TEM image (left) and particles size distribution histograms for silica particle (right). For the histogram the diameter at least of 200 different particles was determined from different TEM images.

TEM enables direct observation of individual particles, giving information not only about the particle size but also about their morphology. Analysis of the size distribution is direct and requires no fitting or modeling. A disadvantage of this method is that the samples must be dried, which can cause the formation of aggregates that may not have existed in the original colloidal suspension. On the other hand, with SAXS or SANS technique, it is possible to identify aggregates in the system through observation of the low- q scattering behavior. These methods give no information about individual particles but about the entire ensemble of particles, containing details about the size of the particles as well as on the interactions between them. However, the analysis of the SAXS and SANS data is dependent on the model used to fit the data, and different models are often capable of producing equally good fits to the experimental data. The choice of model and the parameters used then become critical to the quality of the quantitative results.

Table 6.1. Characterization of the silica dispersion by SANS.*

$(10^{10} \rho \text{ cm}^{-2})$	R_G (nm)	R_P (nm)	R_S (nm)	σ	$\langle R_S \rangle$ (nm)	$\langle A_S \rangle$ (nm ²)	$\langle V_S \rangle$ (nm ³)
3.54	14.95	10.52	13.30	0.11	13.38	$2.28 \cdot 10^3$	$1.04 \cdot 10^4$

*Guinier radius R_G , Porod radius R_P , parameters R_S and σ of the log-normal size distribution, average radius $\langle R_S \rangle$, average surface area $\langle A_S \rangle$, and average volume $\langle V_S \rangle$ of the silica beads.

In Fig. 6.2 the coherent scattering cross section $I(q)$ of a dilute silica dispersion in D₂O-rich water ($\rho_D = 5.74 \times 10^{10} \text{ cm}^{-2}$) is plotted as a function of wave-vector q . The inset shows the scattering profile of the same silica dispersion in a mixture of H₂O/D₂O, which matches the scattering length density of the silica particles and make them invisible in neutron scattering. At the high dilution (0.567 vol.-%) of the silica sol only the form factor contributes to the scattering intensity, since the repulsive interparticle interactions are negligible at this dilution. This is seen from the fact that $I(q)$ becomes horizontal in the low q region of the scattered intensity in Fig. 6.2. The position of the local maximum in $I(q)$ at intermediate q defines the size of the particles and suggests that the particles have a rather narrow size distribution. The scattering profile was found

to be consistent with a log-normal size distribution of polydisperse spheres with a mean particle radius $R_s = 13.30$ nm and a polydispersity, $\sigma = 0.11$ (solid lines). The value of the parameters R_s and σ were calculated with the eqs. (2.33), (2.34) and (5.1) described in chapter 2 and 5 respectively, using the equivalent sphere radius obtained from the Guinier and Porod regime (*cf.* Fig. 2.15 and Section 2.4.2). The results are summarized in Table 6.1. As can be seen the value of R_G is significantly larger than that of R_P for the silica sample. This difference may be due to polydispersity and/or deviations from spherical geometry, or surface roughness of the particles, as has been previously discussed in chapter 5.

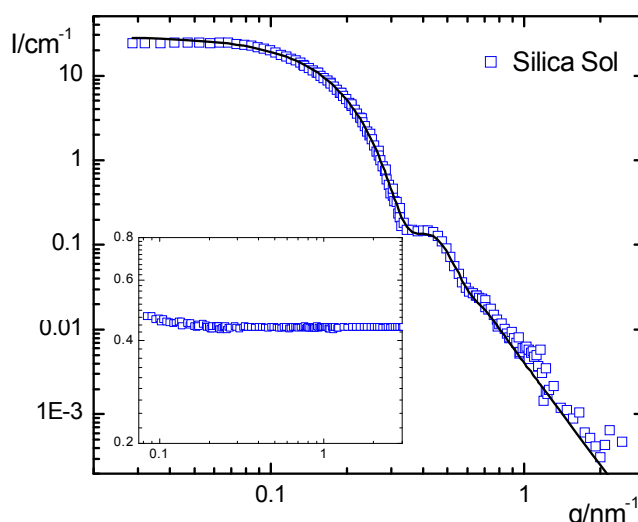


Figure 6.2. Scattering profile of dilute silica dispersions in nearly pure D_2O at pH 9 (298 K). The solid line represents the best fit with the log-normal size distribution function. The SANS profile showing mainly incoherent background for the silica dispersion in contrast matching H_2O/D_2O is shown in the inset.

The nitrogen adsorption isotherm of the dried silica was analyzed by the BET method in a range of relative pressures p/p_0 from 0.05 to 0.3 (Fig. 6.3). The specific surface area obtained in this way, $a_s = 135$ m² g⁻¹, is greater than the geometric surface area $a_{geom} = 103$ m² g⁻¹ derived from the particle radius R_s of 13.3 nm obtained by SANS and the mass density of silica ρ_s (2.20 g cm⁻³). The ratio $a_s/a_{geom} = 1.31$ can be attributed to surface roughness of the particles (according with the differences of the values between R_G and R_P from SANS analysis) and indicates a low porosity of the silica particles. In the inset of

Fig. 6.3 the nitrogen adsorption isotherm of the dried silica is shown. It exhibits the same feature at relative pressures $p/p_0 > 0.5$ as the silica used in the study presented in chapters 4 and 5. As has been mentioned there, this feature can be attributed to pore condensation in the voids between close-packed silica particles in the dried sample and is thus of no significance for the present work.

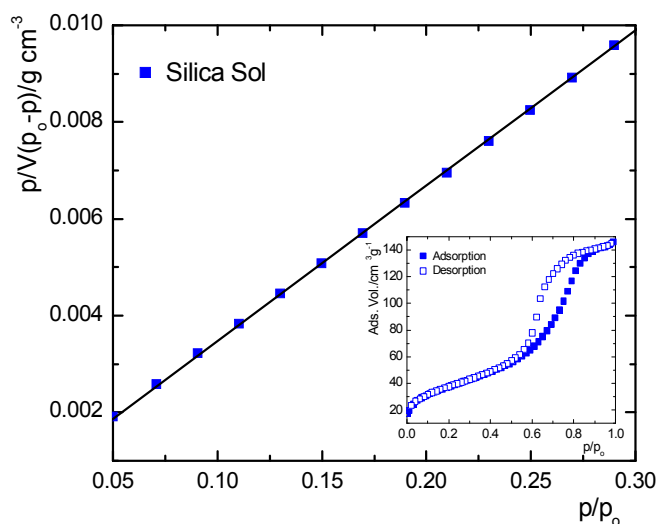


Figure 6.3. BET plot of the nitrogen adsorption on the dried silica particles; the full adsorption isotherm is shown in the inset.

6.2.2 Adsorption of the binary surfactant mixtures at the air/liquid interface

Surface tension isotherms of the binary systems $C_{12}DAO:\beta\text{-}C_{10}G_2$ and $C_{12}DAO:\beta\text{-}C_{12}G_2$ at three different mass ratios (3:1, 1:1, 1:3), at pH 9 and 298 K are displayed in Figure 6.4, together with those of $C_{12}DAO$, $\beta\text{-}C_{10}G_2$ and $\beta\text{-}C_{12}G_2$ alone. The value of the *CMC* were calculated from these plots as the concentration of the intersection point of the two linear sections on the curve of γ vs. $\text{Log } C$ [6.11]. The resulting *CMC* values are given in Table 6.2, together with the values of other properties (γ_{\min} , Γ , A_{\min}) obtained from the surface tension isotherms. The lines drawn through the points in the maximum slope region represent linear least squares regression fits to the data and the straight lines sketched in after the break are provided for visual continuity of the data. The respective break point concentrations of the pure $\beta\text{-}C_{12}G_2$ surfactant (*CMC*

$= 1.70 \times 10^{-4}$ M) is in good agreement with the respective *CMC* values determined in previous studies using surface tension method, e.g. Rosen et. al. [6.12] reported a value of *CMC* = 1.62×10^{-4} M for β -C₁₂G₂. However, the *CMC* values at pH 9 for pure β -C₁₀G₂ (*CMC* = 1.00×10^{-3} M) and pure C₁₂DAO (*CMC* = 1.46×10^{-3} M) are relative lower than the values reported in the literature. For example, in the case of β -C₁₀G₂, Rosen et. al. [6.12] found a value of *CMC* = 1.95×10^{-3} M, and in the case of C₁₂DAO solutions, Rathman et al. [6.13a] found that the *CMC* = 1.9×10^{-3} M in 0.06 M NaBr at pH 8 and Maeda et al. [6.13b] reported a *CMC* = 1.6×10^{-3} M in 0.1 M NaCl and a *CMC* = 1.4×10^{-3} M in 0.2 M NaCl at pH 10. From the surface tension data (see Fig. 6.4 and Table 6.2), it is seen that the *CMC* decreases from the value of pure C₁₂DAO when adding maltoside surfactant (β -C_nG₂) to the solution. A minimum value of the *CMC* of the surfactant mixture is met for the mixture C₁₂DAO: β -C₁₂G₂ = 1:3, suggesting a strong interaction between the two surfactant molecules at this composition. In addition, somewhat lower values of the surface tension at the *CMC* are found for the mixtures relative to the pure surfactant, but this lowering is rather weak and not statistically significant. It seems that the mixed micelles is C₁₂DAO dominant over the whole concentration range, except in the case of the mixtures with 50% in weight of each component (mixture ratio 1:1), where a strong competitive domain between the two surfactants occurs, because the behavior of the surface tension of the mixed solution before to reach the *CMC* is very close to the behavior of the maltoside surfactant, being more pronounced this behavior of the mixture with the same hydrophobic group, C₁₂DAO: β -C₁₂G₂ (see Fig. 6.4), but on the another hand, the minimum surface tension, γ_{\min} , value is lower but similar to those of the pure C₁₂DAO. From these results, one can conclude, qualitatively, that each mixture presents synergistic effect, which this effect is stronger for the mixtures with higher amount of β -C_nG₂ (mixture ratio 1:3), because the *CMC* is lower than those of either pure component of the mixture. The minimum surface area of the head groups A_{\min} , and the surface density Γ at the air/water interface are similar to the values of pure C₁₂DAO indicating that this surfactant dominates at each mixture composition.

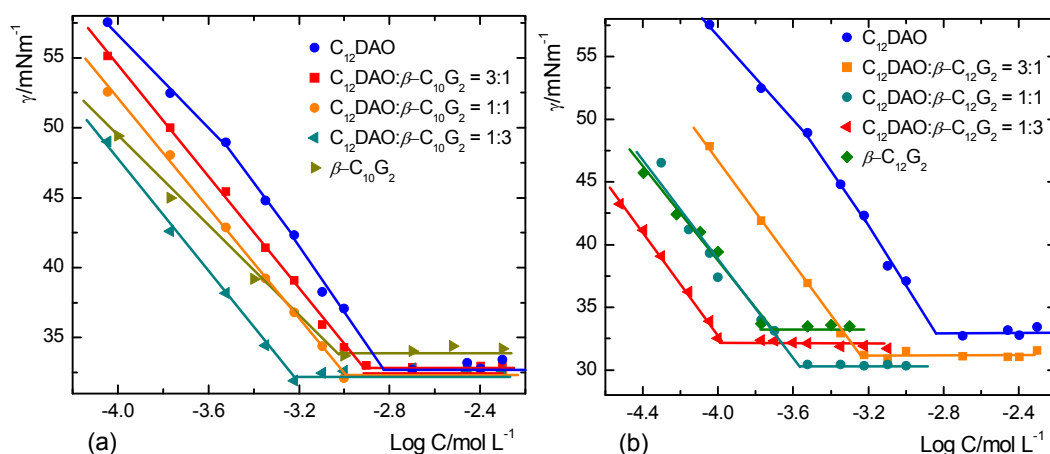


Figure 6.4. Surface tension isotherms of binary surfactant mixtures as function of $\log C_{total}$: (a) $C_{12}DAO:\beta-C_{10}G_2$; (b) $C_{12}DAO:\beta-C_{12}G_2$.

Table 6.2. Surface properties of $C_{12}DAO:\beta-C_{10}G_2$ and $C_{12}DAO:\beta-C_{12}G_2$ mixtures and individual surfactants.*

Sample	CMC (10^{-3} mol L ⁻¹)	γ_{min} (mN m ⁻¹)	Γ (μ mol m ⁻²)	A_{min} (nm ²)
$C_{12}DAO:\beta-C_{10}G_2$				
1 : 0	1.46 ± 0.037	33.0	3.46	0.48
3 : 1	1.25 ± 0.017	33.0	3.49	0.48
1 : 1	1.00 ± 0.012	32.4	3.45	0.48
1 : 3	0.60 ± 0.015	32.5	3.59	0.46
0 : 1	1.00 ± 0.042	34.0	3.00	0.55
$C_{12}DAO:\beta-C_{12}G_2$				
1 : 0	1.46 ± 0.037	33.0	3.46	0.48
3 : 1	0.60 ± 0.029	31.2	3.60	0.46
1 : 1	0.30 ± 0.034	30.4	3.42	0.49
1 : 3	0.10 ± 0.030	32.1	3.57	0.47
0 : 1	0.17 ± 0.024	33.6	3.29	0.51

* Minimum surface tension γ_{min} , adsorbed amount at the air/water interface Γ , minimum surface area occupied by the head groups of the surfactants at the air/water interface A_{min} .

Based on the pseudo-phase separation model (PPS), the value of the mixed CMC is related to the non-ideality parameter for the formation of mixed micelles β^M , which measures the nature and extent of the interaction between the two different surfactant molecules in the mixed micelles and can be evaluated using the eq. (2.6). The values of β^M derived by this means at each composition are given in Table 6.3, together with values of the predicted micellar composition. If mixing in the micelle is ideal, β^M should be zero as is common in the nonionic-

nonionic mixtures or nonionic-zwitterionic mixtures at $\text{pH} \geq 7$ [6.12, 6.14], but it is evidently that in both surfactant systems at each mixture ratio all values of β^M are negative, which value increases with increasing the amount of $\beta\text{-C}_n\text{G}_2$ in the solution, suggesting that C_{12}DAO mixes non-ideally with any of the maltoside surfactants ($\beta\text{-C}_{10}\text{G}_2$ or $\beta\text{-C}_{12}\text{G}_2$) and the attractive interaction between the head groups of these surfactants is stronger at higher amounts of $\beta\text{-C}_n\text{G}_2$, increasing thus, the synergistic effect as can previously deduced from analysis of the surface properties of these mixtures (see Fig. 6.4 and Table 6.2). The non-ideality of each surfactant mixture is confirmed by the comparison of the observed values of the mixed CMC 's with the calculated values according to the ideal mixing model (eq. (2.1)), which are shown as a solid line in Figure 6.5.

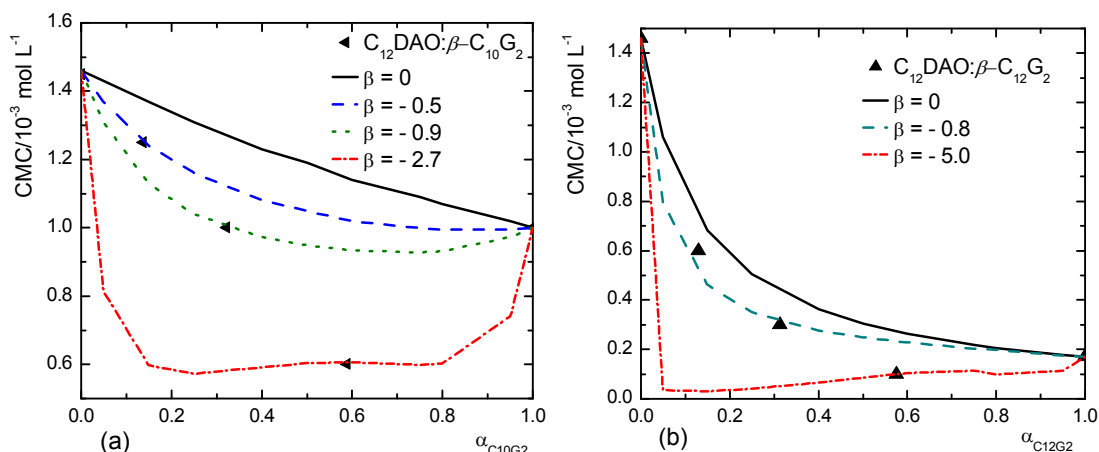


Figure 6.5. Critical micelle concentrations of the surfactant mixtures as a function of composition: (a) $\text{C}_{12}\text{DAO}:\beta\text{-C}_{10}\text{G}_2$; (b) $\text{C}_{12}\text{DAO}:\beta\text{-C}_{12}\text{G}_2$. The solid lines are calculated for ideal mixing of both systems and the dashed lines are predicted from the non-ideal pseudo-phase separation model (PPS).

Table 6.3. Molecular interaction in the bulk and at the air/water interface, and predicted micellar and interfacial composition of $\text{C}_{12}\text{DAO}:\beta\text{-C}_{10}\text{G}_2$ and $\text{C}_{12}\text{DAO}:\beta\text{-C}_{12}\text{G}_2$ mixtures.*

Sample	$\text{C}_{12}\text{DAO}:\beta\text{-C}_{10}\text{G}_2$				$\text{C}_{12}\text{DAO}:\beta\text{-C}_{12}\text{G}_2$			
	β^M	X_1^M	β^σ	X_1^σ	β^M	X_1^M	β^σ	X_1^σ
3 : 1	-1.62	0.65	-1.44	0.69	-1.37	0.42	-2.13	0.46
1 : 1	-1.66	0.51	-1.63	0.54	-2.42	0.32	-4.22	0.39
1 : 3	-3.28	0.40	-3.61	0.43	-6.17	0.33	-6.42	0.36

* X_1^M and X_1^σ denotes the molar fraction of C_{12}DAO in the total mixed micelle and monolayer at the air/liquid interface, respectively.

The non-ideality mixing of the $C_{12}DAO:\beta-C_{10}G_2$ and $C_{12}DAO:\beta-C_{12}G_2$ mixtures suggests that the degree of protonation of $C_{12}DAO$ is somehow affected by adding maltoside surfactant to the solution, resulting in a lowering of the pH of the system. The β^M range value from -1.6 to -2.5 of mixtures at ratios 3:1 and 1:1 is of the same order as those found by Matsson et al. [6.3c], in the study of the adsorption of mixtures of $C_{12}DAO:\beta-C_{12}G_2$ at the air/liquid interface and on silicon wafers at neutral pH. They suggest that at natural pH (~ 7), $C_{12}DAO$ is present both as nonionic and as cationic species, where the major part in bulk is nonionic and the degree of ionization decreases from 0.11 at low concentrations (pH 5.8) to 0.008 at CMC (pH 7). Suddenly, the molecular interaction parameter β^M increases drastically at higher amounts of $\beta-C_nG_2$ being more evident this behavior in the mixture with the same hydrocarbon group, indicating that $C_{12}DAO$ behaves like a cationic surfactant because the value of $\beta^M = -6$ is even stronger than the values of cationic-nonionic mixtures [6.12] being comparable with those values for strong electrostatic interactions presented in anionic-nonionic systems [6.14].

In Table 6.3 is also shown the molecular interaction parameters for mixed adsorption film formation at the air/water interface β^s , which was calculated by eq. (2.4). In general, the values of β^s and of β^M of each surfactant mixture are similar, indicating same magnitude of interaction on the monolayer as in the mixed micelles, except for $C_{12}DAO:\beta-C_{12}G_2$ mixtures at ratios 3.1 and 1:1, where the values of β^s are somewhat larger than those of β^M . This effect may be due to the greater difficulty of incorporating the hydrophobic group in the interior of a convex micelle than at the planar air/aqueous solution interface, being this effect stronger for the micelles with same chain length.

6.2.3 Structure of Surfactant Aggregates in Aqueous Solutions

SANS data on mixed micelles of $C_{12}DAO:\beta-C_{10}G_2$ and $C_{12}DAO:\beta-C_{12}G_2$ mixtures and on the individual components were obtained in a H_2O/D_2O solvent mixture of a scattering length density equal to that of the silica ($\rho_{HD} = 3.54 \times 10^{10} \text{ cm}^{-2}$) at pH 9 and at 298 K. Most of the SANS curves show a horizontal regime

at low q (Figure 6.6), suggesting formation of small aggregates, such as globular or ellipsoidal micelles. The absence of a correlation peak is expected at the chosen low concentrations of the surfactants in solution (0.9-1.0 vol.-%), and indicates negligible intermicellar interactions between the micelles. This has been verified by comparison of the experimental zero angle scattering intensity I_0 , and that obtained by the Guinier approximation ($I_{0\text{exp}}/I_{0\text{G}} \approx 1$; Table 6.4). On the basis of this conclusion, the structure factor was not taken into account in the model fitting of the experimental data. However, a different behavior is observed for the $\text{C}_{12}\text{DAO}:\beta\text{-C}_{12}\text{G}_2$ 1:3 mixture. In this case the slope of $I(q)$ at intermediate q obeys a q^{-1} regime, indicating formation of cylindrical or rod-like micelles [6.15]. In spite of that other kind of aggregates are forming under these conditions, the intermicellar interactions are still negligible, as is suggested by the ratio $I_{0\text{exp}}/I_{0\text{G}} \approx 1$.

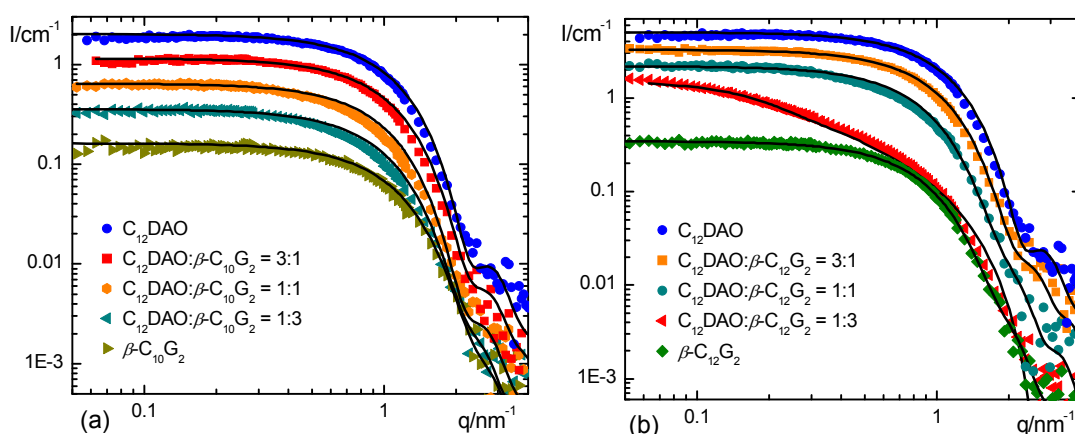


Figure 6.6. SANS profiles of the surfactant mixtures and individual components in the contrast matching $\text{H}_2\text{O}/\text{D}_2\text{O}$ (pH 9, 298 K): (a) $\text{C}_{12}\text{DAO}:\beta\text{-C}_{10}\text{G}_2$; the curves with higher amounts of C_{12}DAO are shifted vertically relative to that of mixture with ratio 1:3 by factors of 1.5 (ratio 1:1), 2.5 (ratio 3:1) and 4 (ratio 1:0). (b) $\text{C}_{12}\text{DAO}:\beta\text{-C}_{12}\text{G}_2$; the curves with higher amounts of C_{12}DAO are shifted vertically relative to that of mixture with ratio 1:3 by factors of 3.5 (ratio 1:1), 6 (ratio 3:1) and 10 (ratio 1:0). The total surfactant concentrations (vol.-%) is approximately 1. Solid lines represent fits by the ellipsoidal core shell model; except for $\text{C}_{12}\text{DAO}/\beta\text{-C}_{12}\text{G}_2$ 1:3 mixture, where the lines represent fits with the cylindrical core shell model.

6.2.3.1 Geometric Modelling

In order to get some preliminary information about the micellar dimensions of the surfactant aggregates prior to performing fits by an appropriate form factor model, a model-free analysis of the Guinier and Porod regimes of $I(q)$ in terms

of the micelle dry volume was performed as a basis for simple geometrical models of the surfactant aggregates. These results are summarized in Table 6.4. The Guinier expression for spheres $I(q) = I_0 \exp(-R_g^2 q^2/3)$ was used to fit the data in the low- q region for the scattering profiles with flat regime at this region. In the case of the C₁₂DAO:β-C₁₂G₂ 1:3 mixture, formation of cylinders was assumed as the simplest shape to represent elongated aggregates. Accordingly, the Guinier expression for cylinders $I(q) = I_0 \exp(-R_g^2 q^2/4)$ was used to fit these data in the low- q region.

Table 6.4. Geometrical parameters for the individual and mixed surfactant aggregates obtained from Guinier and Porod regime.*

Sample	$\varphi_{exp}/\%$	R_g (nm)	R_G (nm)	I_{0G} (cm ⁻¹)	I_{0exp}/I_{0G}	n_{agg}	A_p (10 ⁻⁹ nm ⁻⁵)	S/V (10 ⁵ cm ⁻¹)
C₁₂DAO:β-C₁₀G₂								
1:0	1.14	1.63	2.10	0.49	0.84	73	14.07	1.67
3:1	1.07	1.72	2.23	0.46	0.94	78	9.24	1.24
1:1	0.99	1.92	2.48	0.43	0.92	87	9.04	1.45
1:3	0.92	1.96	2.53	0.35	0.97	93	7.04	1.51
0:1	0.81	1.64	2.12	0.16	1.03	70	6.86	2.60
C₁₂DAO:β-C₁₂G₂								
1:0	1.14	1.63	2.10	0.49	0.84	73	14.07	1.67
3:1	1.10	1.85	2.38	0.55	1.02	89	13.36	1.77
1:1	1.03	2.42	3.12	0.64	0.99	118	7.88	1.22
1:3	0.95	6.94	n.a.	1.52	1.05	346	7.88	1.58
0:1	0.87	2.02	2.61	0.35	0.92	118	6.86	2.30

*experimental volume fraction φ_{exp} , gyration radius R_g , Guinier radius R_G , scattering angle zero experimental and from Guinier I_{0exp} and I_{0G} , respectively; aggregation number n_{agg} obtained from micelle dry and monomer volume, porod constant A_p , specific surface area of the micelles S/V .

As can be seen in Table 6.4, the values of gyration radius for pure C₁₂DAO and β-C₁₀G₂ are similar, and similarly for the values of Guinier radii and the aggregation number n_{agg} , which suggests formation of small aggregates of similar size. As is expected, these values are lower than those of pure β-C₁₂G₂, because the head group of the maltoside surfactant is somewhat bigger than that of the alkyl amino oxide surfactant (*c.f.* Table 6.2). All these values are consistent with previous studies made with SANS and SAXS for the same surfactants [6.16, 6.17], and the aggregation number n_{agg} of C₁₂DAO of 73 is comparable with that of 70 for nonionic micelles in solutions with no added salt

[6.18], indicating that the degree of ionization α_M of the C₁₂DAO solutions is zero, *i.e.* C₁₂DAO is in a non-ionized state in the micelles. Adding maltoside surfactant (β -C₁₀G₂ or β -C₁₂G₂) to the C₁₂DAO solution, a weak increase of the size of the micelles occurs, which is reflected in the n_{agg} values. This increase of size and n_{agg} is most pronounced at the higher concentrations of β -C₁₂G₂ in the system (*c.f.* Table 6.4 and Fig. 6.6), suggesting a transition from small aggregates formed with small amount of β -C₁₂G₂ to elongated (cylindrical or rod-like) mixed micelles.

From the high- q region (Porod regime) one can obtain information about the volume-based surface area S/V of the surfactant aggregates. This value may be compared with the S/V values of the mixed surfactants adsorbed on the silica nanoparticles, if formation of surface aggregates on the silica beads occurs.

6.2.3.2 Form Factor Models

SANS data from pure surfactants and their mixtures have been analyzed in terms of the existence of only one type of micellar aggregate present in the solution, in agreement with studies of pure maltoside surfactants (β -C₁₀G₂ and β -C₁₂G₂) [6.16, 6.19] and C₁₂DAO solutions at pH values higher than 7 [6.20, 6.21].

In order to choose the best micelle model for representing the SANS data for the samples with a flat regime at low q region (except C₁₂DAO: β -C₁₂G₂ 1:3 mixture), we have first fitted the data by using the simplest spherical model assuming monodisperse or polydisperse spherical micelles containing dried and hydrated shell. In all cases a good representation of the measured SANS data requires core radii greater than the fully extended length of a surfactant tail, which implies an unphysical hole at the center of the micelle or that the hydrated head groups are pulled into the micelle interior. Another shortcoming of this model is that the accurate between the experimental and the fitted volume fraction of total surfactant in the solution, as well as the experimental (obtained from micelle dry and monomer volume) and the theoretical aggregation number (results not shown) is greater than 31%, which accurate should be less than 10%. Because of those shortcomings the spherical model

was ruled out and it was decided to model the data assuming monodisperse, core-plus-shell ellipsoids with a shell containing a hydrated head group and a core containing the hydrocarbon chain. The fitting parameters were the number density of micelles N/V , the rotational semi axis a and the equatorial semi axis b of the ellipsoid core, the polar head layer of constant thickness d (assumed to be the same along the short and long axes) and the scattering length density of the polar head layer (*cf.* Table 6.5). The fixed parameters were the scattering length density of the hydrocarbon chain and of the solvent (assuming that aqueous solvent molecules cannot permeate in the hydrophobic core). The quality of the fit was improved when hydration of the surfactant head group was taken into account.

The data obtained for micelles of the individual surfactants ($C_{12}DAO$, β - $C_{10}G_2$, β - $C_{12}G_2$) as well as for the mixed micelles ($C_{12}DAO:\beta$ - $C_{10}G_2$ and $C_{12}DAO:\beta$ - $C_{12}G_2$) were consistent with the formation of small aggregates, such as oblate ellipsoids; in agree at least for the pure maltoside surfactants with previous studies [6.16, 6.19a,b]. In the case of aqueous solutions of pure $C_{12}DAO$, the data is better represented with the oblate ellipsoids model than with the prolate ellipsoids model, as mentioned in chapter 5, which agree with the fits obtained by Båverbäck [6.21]. Model fits are shown as solid lines in Fig. 6.6 and some of the corresponding fit parameters are given in Table 6.5.

As can be observed in Table 6.5 the rotational semi-axes a decreases when β - $C_{10}G_2$ is added to the $C_{12}DAO$ aqueous solution, while in the case of the mixed micelles formed by surfactants with the same hydrocarbon chain, *i.e.* $C_{12}DAO:\beta$ - $C_{12}G_2$, “ a ” scarcely changed when increases the amount of β - $C_{12}G_2$ in the mixture. On the other hand, the equatorial semi axis b as well as the shell thickness d increases in both systems with addition of β - C_nG_2 . The thickness of the polar head of the $C_{12}DAO:\beta$ - $C_{12}G_2$ mixtures at ratios 1:1 and 1:3 is nearly equal as for the pure maltoside surfactants, indicating that the mixed micelles are dominated by β - C_nG_2 at these compositions. This value of d agrees with that found by Dupuy et. al. [6.19b] ($d \sim 0.62$ nm), who speculate that there is not a rigid alignment of the two sugar rings with the hydrophobic tail, but rather a bending of the outer sugar ring toward the inner ring.

Table 6.5. Fit parameters for the individual and mixed surfactant aggregates obtained from form factor models.*

Sample	a (nm)	b (nm)	d (nm)	R_c (nm)	L (nm)	A_{\min}^{\ddagger} (nm ²)	$n_{\text{agg}}^{\ddagger}$	$n_{\text{H}_2\text{O}}^{\ddagger}$
C₁₂DAO:β-C₁₀G₂								
1:0	1.41	2.15	0.31	n.a.	n.a.	0.44	78	4
3:1	1.35	2.19	0.32	n.a.	n.a.	0.42	79	3
1:1	1.37	2.20	0.49	n.a.	n.a.	0.40	83	6
1:3	1.30	2.30	0.49	n.a.	n.a.	0.36	90	3
0:1	1.25	2.22	0.60	n.a.	n.a.	0.35	87	2
C₁₂DAO:β-C₁₂G₂								
1:0	1.41	2.15	0.31	n.a.	n.a.	0.44	78	4
3:1	1.42	2.38	0.32	n.a.	n.a.	0.39	96	3
1:1	1.41	2.68	0.60	n.a.	n.a.	0.34	122	8
1:3	n.a.	n.a.	0.61	1.36	23.77	0.52	393	5
0:1	1.45	2.87	0.60	n.a.	n.a.	0.31	142	1

* rotational semi-axis a and equatorial semi-axis b of the ellipsoid core, head group thickness d , core radius R_c and length of a cylindrical L micelle, respectively; minimum surface area A_{\min} of the head group of the surfactants occupied at the core/shell interface, aggregation number n_{agg} , number of molecules of water in the shell $n_{\text{H}_2\text{O}}$. [‡]Values calculated from the fitted parameters.

The aggregation number for all samples of both systems is in good agreement with the values found by the model-free analysis obtained from the micelle dry and monomer volume. On the other hand, the number of molecules of water $n_{\text{H}_2\text{O}}$, reaches a maximum value at the surfactant ratio 1:1, suggesting that the head groups are accommodated in a way that favours the formation of hydrogen bonds with the water molecules of the aqueous medium. The minimum surface area A_{\min} occupied by the head group at the core/shell interface follows the same trend as at the air/liquid interface, but their values are lower, which is attributed to the more compact or rigid accommodation of the surfactant head groups in the micelles than at the air/liquid interface. The lowest value of the maltoside head group area ($A_{\min} \sim 0.31\text{-}0.35$ nm) is consistent with the value found by Dupuy et. al. [6.19b], which is also comparable to the values found in lamellar phases.

An interesting finding of the SANS study of these systems is the drastically higher values of all structural parameters in the C₁₂DAO:β-C₁₂G₂ mixture with high content of β-C₁₂G₂ (i.e. ratio 1:3), which indicate elongation of the ellipsoidal micelles. This result is surprising, considering that the pure sugar

surfactants as well as C_{12} DAO forms small micelles at pH 9. The best representation of these data was obtained with a cylindrical core-shell form factor [6.22]. In this case, the fit parameters were the number density of micelles N/V , the length L and the core radius R_c of the cross-sectional area of the cylindrical micelles, the shell thickness d and the scattering length density of the shell layer (cf. Table 6.5). The fixed parameters were the same as the ellipsoidal model.

The structure of micelles of this mixture is in good agreement with those morphologies found for C_{12} DAO solutions with salt [6.18b] and in aqueous solutions fully ionized tetradecyldimethylamine oxide (TDAO) in the presence of 0.1 M NaCl [6.23]. The reason of this growth behavior of micelles of that composition is not clear. One possibility is could be the formation of hydrogen bonds between the two head group types, which is favored by the same length of the hydrocarbon tail. In combination with the decrease of the head-group repulsion between the amino oxide groups in β - $C_{12}G_2$ rich mixtures, this may lead to micelle growth. In this case β - $C_{12}G_2$ would behave like a salt in aqueous solution of ionic surfactants.

6.2.4 SANS study of the adsorbed layer of surfactant mixtures on the surface of silica nanoparticles

The main aim of performing the SANS study of these systems is to elucidate the nature of mixed surfactant aggregates formed by two nonionic surfactants (C_{12} DAO and β - C_nG_2) of different adsorption affinity on silica sols and to find out whether the non-adsorbing maltoside surfactant is incorporated in the adsorbed layer of C_{12} DAO through hydrophobic interactions, or whether the maltoside surfactant is not incorporated in the adsorbed layer.

SANS measurements were made a low concentration (1.5 vol.-%) of the silica sol in a H_2O/D_2O mixture ($\rho_{HD} = 3.54 \times 10^{10} \text{ cm}^{-2}$) which matches the scattering length density of silica such that only surfactant aggregates are visible, and at pH 9 to avoid particle aggregation and to assure that C_{12} DAO behaves as non-ionic surfactant. For each binary system (C_{12} DAO: β - $C_{10}G_2$ and C_{12} DAO: β - $C_{12}G_2$), a 1:1 mixture of the surfactants was added at 5

concentrations based on the $C_{12}DAO$ adsorption value, *viz.* $\frac{1}{4}\Gamma_{mx}$, $\frac{1}{2}\Gamma_{mx}$, $\frac{3}{4}\Gamma_{mx}$, $\frac{7}{8}\Gamma_{mx}$, and Γ_{mx} (at a $C \gg CMC$) of $C_{12}DAO$ (where Γ_{mx} is the plateau value of the adsorption isotherm of $C_{12}DAO$ on silica). In addition, in order to test the effect of the surfactant composition on the adsorption, other ratios were prepared for the samples at $\frac{1}{2}\Gamma_{mx}$ of $C_{12}DAO$, keeping the concentration of $C_{12}DAO$ constant and varying the concentration of $\beta-C_nG_2$, and varying the concentration of both surfactants. And in order to study the excess of both surfactants in the mixture samples at 1 vol.-% were prepared at different ratios by varying the amount of both components (*i.e.* mixture ratios $x:y$). The set of samples prepared for the SANS measurements in both systems are summarized in Table 6.6.

Table 6.6. Set of samples prepared for each binary system ($C_{12}DAO:\beta-C_nG_2$) in silica sol for the SANS measurements.

	Set A*	Set B [†]	Set C	Set D
	$\frac{1}{2}\Gamma_{mx}$ $C_{12}DAO:\beta-C_nG_2$	$\frac{1}{2}\Gamma_{mx}$ $C_{12}DAO:\beta-C_nG_2$	$Z\Gamma_{mx}$ $C_{12}DAO:\beta-C_nG_2$	1 vol.-% $C_{12}DAO:\beta-C_nG_2$
	1 : 0	7 : 3	$Z = \frac{1}{4}$; 1:1	3 : 1
Mixture	1 : 0.07	6 : 4	$Z = \frac{1}{2}$; 1:1	1 : 1
Ratio	1 : 0.33	4 : 6	$Z = \frac{3}{4}$; 1:1	1 : 3
	1 : 1	3 : 7	$Z = \frac{7}{8}$; 1:1	-
	1 : 3	-	$Z = 1$; 1:1	-

*keeping the concentration of $C_{12}DAO$ constant and varying the concentration of $\beta-C_nG_2$; [†]varying the concentration of $C_{12}DAO$ and of $\beta-C_nG_2$.

Figure 6.7 shows the scattering profiles $I(q)$ for all $C_{12}DAO:\beta-C_{10}G_2$ and $C_{12}DAO:\beta-C_{12}G_2$ surfactant mixtures in silica sol corresponding to the samples of set A. In this set, the concentration of $C_{12}DAO$ was kept constant at a value corresponding to a surface concentration $\frac{1}{2}\Gamma_{mx}$. And the concentration of $\beta-C_nG_2$ was varied in order to get four different surfactant ratios (1:0.07, 1:0.33, 1:1, 1:3), together with pure $C_{12}DAO$ at $\frac{1}{2}\Gamma_{mx}$. Set B, C and D exhibit a similar behaviour in the scattering profiles $I(q)$ as shown in Figures A.1 and A.2 in Appendix and in Fig. 6.11, respectively.

Qualitatively, most of the scattering profiles are similar to that of $C_{12}DAO$ at without maltoside surfactant, but significant differences in detail can be found, as will be shown below. All scattering profiles exhibit a local maximum (q_{max}) at $q \approx 0.32 \text{ nm}^{-1}$, which is attributed to the existence of a surfactant layer on the

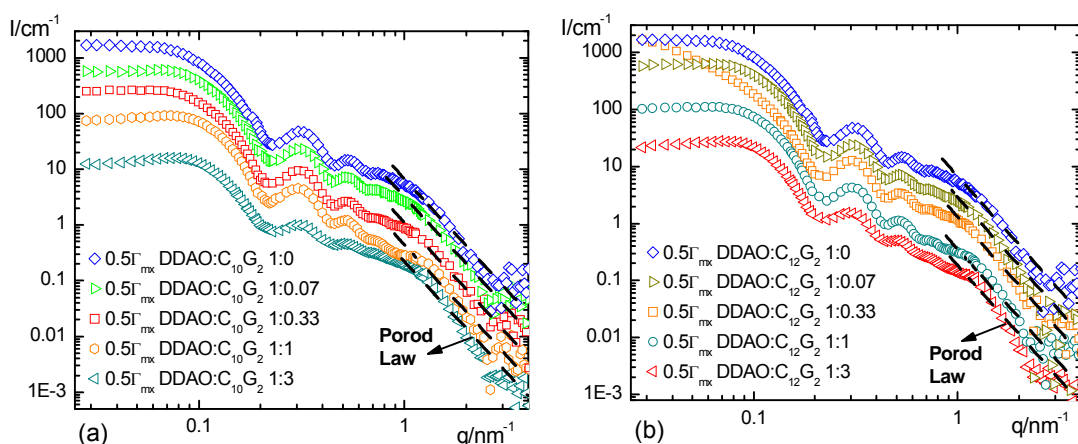


Figure 6.7. SANS profiles $I(q)$ for silica with adsorbed surfactant mixtures based on the surface concentration $\frac{1}{2}\Gamma_{\text{mx}}$ of C_{12}DAO in the contrast matching $\text{H}_2\text{O}/\text{D}_2\text{O}$ (pH 9, 298 K) : (a) $\text{C}_{12}\text{DAO}:\beta\text{-C}_{10}\text{G}_2$; the curves with higher amounts of C_{12}DAO are displaced vertically by factors of 4 (1:1), 12 (1:0.33), 40 (1:0.07) and 85 (1:0) relative to that of the mixture with ratio 1:3. (b) $\text{C}_{12}\text{DAO}:\beta\text{-C}_{12}\text{G}_2$; the curves with higher amounts of C_{12}DAO are displaced vertically by factors of 4 (1:1), 18 (1:0.33), 40 (1:0.07) and 85 (1:0) relative to that of the mixture with ratio 1:3. The dashed lines represent the Porod regime.

surface of the particles. The position of this maximum is not affected by addition of the maltoside surfactant to the silica sol with C_{12}DAO , as to be expected, because the position only depends on the size of the silica beads. The relative height of this maximum scarcely changes by addition of $\beta\text{-C}_n\text{G}_2$, but drastically decreases when the amount of $\beta\text{-C}_n\text{G}_2$ higher than that of C_{12}DAO (*i.e.* in a mixture ratio 1:3). A second local maximum at $q \approx 0.52 \text{ nm}^{-1}$ is also present in the SANS spectra, which apparently is related to the adsorbed surfactant layer because it decreases in pace with the maximum at $q \approx 0.32 \text{ nm}^{-1}$ when increases the amount of $\beta\text{-C}_n\text{G}_2$ in the system. At the same time, the shoulder after this second peak becomes less pronounced. In all cases, the behaviour at the high- q end of the scattering profiles conforms to Porod's law. The reason of the pronounced increase of the intensities in the low q regime for the profile of the ratio mixture $\text{C}_{12}\text{DAO}:\beta\text{-C}_{12}\text{G}_2$ 1:0.33 is not clear. In particular we do not know if this behaviour can be attributed to strong interactions between the coated silica particles, because the set of these measurements at other mixture ratios exhibits a horizontal plateau at low q .

The analysis of the SANS profiles was performed in two steps as for the

data in chapter 5: First, a simple geometrical modelling was used to estimate the volume, effective layer thickness and volume-based surface area of the adsorbed surfactant mixtures. In the second step, nonlinear least-squares fitting of the scattering data to appropriate form factor models was employed in order to extract more detailed information about the size and shape of the surface aggregates.

6.2.4.1 Geometric Modelling

The model-free analysis was based on the Guinier and Porod regimes of $I(q)$ in terms of the dry volume, effective layer thickness, and volume-based surface area of the adsorbed surfactant mixtures as described in chapter 5. This analysis was made on the basis for simple geometrical models of the surface aggregates.

The Guinier expression for spheres, $I(q) = I_0 \exp(-R_g^2 q^2/3)$, was used to fit the data in the low- q region. In order to reduce the effect of interparticle interactions on the determination of the apparent gyration radius R_g , data in the q range from 0.058 to 0.173 nm⁻¹ were used. The effective layer thickness δ_{eff} of the adsorbed surfactants can be estimated from the silica radius R_G and the apparent gyration radius R_g in presence of the surfactant mixture, which was obtained from the Guinier approximation. For example, we find a radius of gyration $R_g = 16.18$ nm for the surfactant mixture C₁₂DAO:β-C₁₂G₂ 1:1 at ½Γ_{mx} of C₁₂DAO in the silica sol ($R_G = 14.95$ nm). In the contrast-match scenario of our experiment, R_g must have a value between the silica radius R_G and $R_G + \delta_{\text{eff}}$, depending on the surfactant density profile. Assuming for simplicity that R_g is half-way between these two values, a typical layer thickness of the adsorbed surfactant is $\delta_{\text{eff}} = 2 \cdot (16.18 - 14.95) = 2.5$ nm. This value is somewhat lower than the values found in the study of the adsorption of pure C₁₂DAO on silica nanoparticles (see chapter 5) [6.24].

From the high- q region (Porod regime) we obtain the volume-based surface area S/V of the surface aggregates, since the concentration of free mixed micelles in solution is negligible at the chosen surfactant concentrations. The respective value for free mixed micelles can be derived from the scattering

profile of the surfactant in the absence of silica (Fig. 6.6). For example, for the surfactant mixture $C_{12}DAO:\beta-C_{12}G_2$ 1:1 at $\frac{1}{2}\Gamma_{mx}$ of $C_{12}DAO$ in the silica sol, $S/V = 1.37 \times 10^5 \text{ cm}^{-1}$. When comparing this value with that found for $C_{12}DAO:\beta-C_{12}G_2$ 1:1 in the H_2O/D_2O mixture in absence of silica ($S/V = 1.22 \times 10^5 \text{ cm}^{-1}$), one finds that S/V for the free mixed micelles is about 11% lower than for the surface aggregates. The similar magnitude of the two values implies similar morphologies of the surfactant aggregates in solution and on the surface, indicating that somehow the maltoside surfactant is incorporated in the adsorbed layer of $C_{12}DAO$. This excludes adsorbed half-micelles, which would require considerably more surface area.

The structural parameters of the surfactant adsorbed layer of both surfactant mixtures, based on the surface concentration of $\frac{1}{2}\Gamma_{mx}$ of $C_{12}DAO$ in the silica sol (obtained from Guinier and Porod regime), are summarized in Table 6.7. Also shown in the Table are values of dry volume of adsorbed surfactants per silica bead, V_{dry} , which is derived from the scattering cross section at zero angle I_0 (see eq. (2.31)) and the number of surface micelles adsorbed on the silica beads N_{mic} , which can be estimated by dividing the dry volume of adsorbed surfactant by the volume of a free mixed micelles, on the assumption that the surface micelles adsorbed on the silica beads are similar to micelles in solution, as has been demonstrated in the Porod regime.

Reasonable agreement between the sets δ_{eff} values for $C_{12}DAO:\beta-C_{12}G_2$ mixtures is found for most mixture ratios, but large deviations appear for $C_{12}DAO:\beta-C_{10}G_2$ mixtures. The results in Table 6.7 indicate that for most mixture ratios the effective layer thickness δ_{eff} is significantly smaller than the extended tail length of $C_{12}DAO$ ($l_c = 1.67 \text{ nm}$) or $\beta-C_{10}G_2$ ($l_c = 1.42 \text{ nm}$) [6.25]. However, for both surfactant systems at mass ratio 1:0.33, where the amount of $C_{12}DAO$ is three times higher than that of the maltoside surfactant, significantly higher values of the gyration radius R_g and effective layer thickness δ_{eff} than for other mass ratios are observed. This behavior is more pronounced in the system with $\beta-C_{12}G_2$, where the two surfactants have the same hydrocarbon group. In this case the value of R_g could be affected by the drastic increase of the scattered intensities $I(q)$ at the low- q region, which behaviour is not clear

and for this reason the value of R_g at the mixture ratio 1:0.33 is not reliable, causing an unreasonably high value of the δ_{eff} , which is almost twice the value of the layer thickness δ of an adsorbed bilayer of $\beta\text{-C}_{12}\text{G}_2$ on titania or alumina [6.26] or the layer thickness δ of adsorbed surface aggregates of C_{12}DAO on silica [6.24].

The model-free analysis results obtained for the sets of samples B, C and D in silica sol are summarized in Tables A.1- A.3 in Appendix.

Table 6.7. Characteristics of the surfactant layer adsorbed on the silica nanoparticles derived from the SANS data of the set of samples A.*

Sample	R_g (nm)	δ_{eff} (nm)	S/V (10^5 cm^{-1})	V_{dry} (10^3 nm^3)	N_{mic}
$\frac{1}{2}\Gamma_{\text{mx}} \text{C}_{12}\text{DAO}:\beta\text{-C}_{10}\text{G}_2$					
1 : 0	16.21	2.52	0.94	2.86	88
1 : 0.07	15.58	1.24	0.96	2.51	70
1 : 0.33	16.74	3.59	1.23	3.59	100
1 : 1	15.37	0.85	1.77	3.39	78
1 : 3	15.32	0.73	4.77	1.69	33
$\frac{1}{2}\Gamma_{\text{mx}} \text{C}_{12}\text{DAO}:\beta\text{-C}_{12}\text{G}_2$					
1 : 0	16.21	2.52	0.94	2.86	88
1 : 0.07	16.26	2.62	0.88	3.72	90
1 : 0.33	18.55	7.20	0.95	4.96	119
1 : 1	16.18	2.46	1.37	5.49	90
1 : 3	16.16	2.42	3.70	4.33	21

*gyration radius R_g , effective thickness δ , volume-based surface area S/V and dry volume V_{dry} of the adsorbed surfactant layer; N_{mic} is the number of surface micelles

6.2.4.2 Core-Shell Model

The simple spherical core-shell model [6.27-6.29] was used as first form factor model to determine if the scattering profiles of the surfactant mixtures can be described with a *complete surfactant bilayer* formed by the two surfactants, with the possibility of an asymmetrical bilayer, *i.e.* C_{12}DAO forming the inner half layer pointing toward the surface and $\beta\text{-C}_n\text{G}_2$ forming the outer half-layer pointing towards the solution. Model calculations were performed assuming a homogenous layer thickness, using two different values ($\delta = 3.0 \text{ nm}$ and 4.0 nm). The former value represents the most reasonable value, which approximates to the effective thickness, δ_{eff} , obtained by Guinier approximation.

The latter value was chosen because is due to that in previous studies of adsorption of C₁₂DAO [6.24] or β -C_nG₂ [6.26, 6.30] on hydrophilic surfaces have suggested formation of surface aggregates and a bilayer with a layer thickness of 4.0 nm.

The fit obtained with this model and the assumed layer thicknesses of 3.0 nm and 4.0 nm exhibits a similar behavior as was found previously for the adsorption C₁₂DAO, C₁₂E₅ and TX-100 on silica beads [6.24, 6.29, 6.31]. This is shown in Fig. 6.8 for the surfactant mixture C₁₂DAO: β -C₁₂G₂ 1:1 at $\frac{1}{2}\Gamma_{\text{mx}}$ of C₁₂DAO in the silica sol. This model underestimates the total adsorbed surface area of the C₁₂DAO: β -C₁₂G₂ mixture, as indicated by the deviations at high wave vectors q between the predicted and experimental intensities. A good representation of the data was found in the q range $0.04 < q < 0.22 \text{ nm}^{-1}$ when the calculated intensities obtained for a layer thickness of 4.0 nm were multiplied by a factor $f = 0.50$ (*cf.* inset Fig. 6.8). However, it is evident that the local maximum at $q \approx 0.32 \text{ nm}^{-1}$ is displaced to lower q values, indicating that the real layer thickness of the adsorbed surfactant should be less than 4.0 nm. The intensities predicted with the effective layer thickness of 3.0 nm give a better approximation of the data at low- q and at the local maximum at $q \approx 0.32 \text{ nm}^{-1}$, without any arbitrary factor f , but still the predicted intensities are displaced to lower q . It appears that the real layer thickness of the adsorbed surfactant should be in the range of $2.5 < q < 3.0 \text{ nm}$. Similar results were obtained for the other mass ratios for both systems and for the other sets of samples described in Table 6.6 (results not shown).

The discrepancies observed for the core-shell model in the high- q region these results indicate that the adsorbed surfactant does not form a uniform layer, but rather forms smaller surface aggregates, which have a higher surface area at a given total adsorbed volume. With this supposition two possibilities can be met: (i) that the adsorption is dominated by C₁₂DAO and the maltoside surfactant is not co-adsorbed in the surface aggregates or (ii) that there is formation of mixed surface aggregates are formed, like those in solution (see Section 6.2.3). However, the preliminary result from the core-shell model is in disagreement with the explanation suggested Matsson et. al. [6.3c] on the

adsorption of β -C₁₂G₂ with 0.1 mM C₁₂DAO on polished silica wafers at natural pH, where they conclude that a small adsorbed amount of C₁₂DAO promotes the formation of a dense, mixed bilayer of surfactants, probably dominated by the maltoside surfactant, which is co-adsorbed through hydrophobic bonding with the adsorbed C₁₂DAO. However, the study of Matsson et al. [6.3c] was based on adsorption isotherms which do not provide detailed structural information about the adsorbed layer. In addition, the pH has a marked effect on the structures formed with the surfactant C₁₂DAO [6.21] both in aqueous solutions and at the solid/liquid interface.

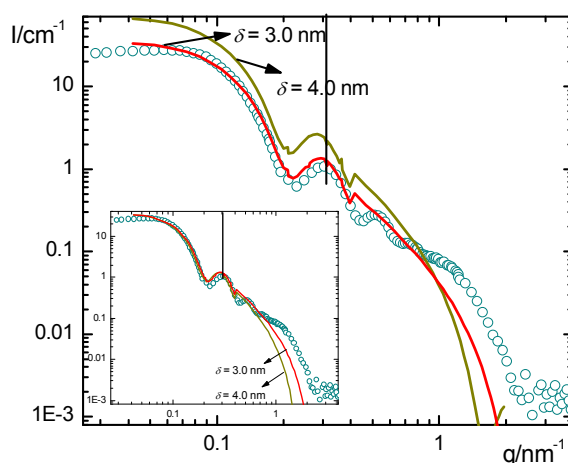


Figure 6.8. Experimental SANS profiles $I(q)$ and intensities predicted by the spherical core-shell model with shell thicknesses $\delta = 3.0$ and 4.0 nm for the surfactant mixture C₁₂DAO: β -C₁₂G₂ 1:1 at the surface concentration $\frac{1}{2}\Gamma_{\text{mx}}$ of C₁₂DAO on silica in contrast matching H₂O/D₂O. The inset shows the predicted intensities with thickness $\delta = 3.0$ and 4.0 nm multiplied with scale factors $f = 1$ and 0.5 , respectively.

6.2.4.3 Micelle-Decorated Silica Model

In preceding studies [6.24, 6.29, 6.31] it was demonstrated that pure nonionic surfactants adsorbed on colloidal silica do not form closed or fragmented bilayers but rather surface micelles of similar structure as in the bulk solution. Instead, these systems have been termed as a surfactant-silica complex and the scattering profiles $I(q)$ of this kind of system can be represented with a micelle-decorated silica model [6.31], which allows to develop calculations for a well-defined number of surface micelles N_{mic} adsorbed on silica beads, together with their dimensional parameters such as radius of spherical surface micelles R_{mic} , and the polydispersity parameter as is explained in reference 6.31 and in

chapter 5 of this Thesis. Here we apply this model to the case of layers formed by surfactant mixtures.

By employing this model, we follow the procedure described in chapter 4 and 5. The fitting of the scattered intensities with this model and the estimation of the real adsorbed surfactant volume, V_{tot} , was based on the layer thicknesses: $\delta = 3.0$ and 4.0 nm. The real adsorbed surfactant volume was calculated by introducing the effective volume fraction of surfactant in the shell, X (i.e. fraction of the layer volume really occupied by the surfactant), which is directly related to factor f , used to rescale the theoretical intensities obtained by the core-shell model to the experimental intensities, by the expression: $X = \sqrt{f}$. For example, for the surfactant mixture $\text{C}_{12}\text{DAO}:\beta\text{-C}_{12}\text{G}_2$ 1:1 at $\frac{1}{2}\Gamma_{\text{mx}}$ of C_{12}DAO in the silica sol with a fixed layer thickness of 4.0 nm, $f = 0.50$, which indicates that only 71% of the layer volume is occupied by the surfactant mixture $\text{C}_{12}\text{DAO}:\beta\text{-C}_{12}\text{G}_2$, on the assumption that $\beta\text{-C}_{12}\text{G}_2$ is incorporated into the adsorbed C_{12}DAO layer. A similar value of X was found for the surfactant system $\frac{1}{2}\Gamma_{\text{mx}}$ $\text{C}_{12}\text{DAO}:\beta\text{-C}_{10}\text{G}_2$ 1:1 (c.f. Table A.4 - A.7 in Appendix). By comparing the values of X of these two binary systems with that of pure C_{12}DAO at the surface concentration $\frac{1}{2}\Gamma_{\text{mx}}$ (where $X = 41\%$) we find that the effective volume fraction of surfactant in the shell X is strongly increased when adding $\beta\text{-C}_n\text{G}_2$ to pure C_{12}DAO . This finding suggests that $\beta\text{-C}_n\text{G}_2$ contributes to the formation of surface micelles by co-adsorption in the adsorbed C_{12}DAO layer. The total surface area of the adsorbed surfactant, A_{tot} , was calculated from the specific surface area of the adsorbed surfactant, S/V as determined by Porod's law ($S/V = A_p/2\pi\Delta\rho^2$) and the number density of silica beads, $(N/V)_S = \phi/\langle V_S \rangle$, by the relation $A_{\text{tot}} = (S/V)_{\text{surf}}/(N/V)_S$.

The total volume, V_{tot} , and surface area, A_{tot} , of the adsorbed surfactant were then used to estimate the number and dimensional parameters of surface aggregates assuming different morphologies. As first approximation, we assumed the formation of isolated spherical surface aggregates with a radius R_{mic} and number of micelles N_{mic} . However, for both surfactant systems at each mass ratio a good representation of the measured SANS data with spherical

surface micelles requires unrealistic values of the micelle radius R_{mic} and of the number of adsorbed surface micelles N_{mic} (≥ 900). The physically unrealistic values of R_{mic} obtained assuming layer thicknesses $\delta = 3.0$ or 4.0 nm are similar with a difference within 10% in most cases. In general, on the assumption of a fixed layer thickness $\delta = 4.0$ nm, the value of R_{mic} for $\frac{1}{2}\Gamma_{\text{mx}}$ of pure C_{12}DAO in silica sol is around 1.0 nm (*i.e.*, less than the length of an extended surfactant molecule) and decreases with increasing amount of $\beta\text{-C}_n\text{G}_2$. For example, for the $\frac{1}{2}\Gamma_{\text{mx}}$ $\text{C}_{12}\text{DAO}:\beta\text{-C}_{12}\text{G}_2$ 1:3 mixture (*i.e.* 75% of $\beta\text{-C}_n\text{G}_2$ in the mixture), $R_{\text{mic}} \approx 0.5$ nm, *i.e.*, less than the half of the length of an extended surfactant molecule. This feature is more pronounced in the mixtures with $\beta\text{-C}_{10}\text{G}_2$. Similar results are obtained for the sets of samples B, C and D in silica sol (results not shown).

For this reason, model calculations similar to those described above were also made for surface aggregates of different geometries, *viz.*, patch-like, ellipsoidal and wormlike micelles. A satisfactory representation of the results was possible with the model of oblate surface micelles (like the surface aggregate structure of pure C_{12}DAO on silica of similar particle size, as described in chapter 5 and reference 6.24). The model involves two structural parameters, R_n and R_{lat} , which also define the orientation of the micelle on the surface (*c.f.* chapter 5 for more details).

This finding agrees with the analysis obtained from Porod regime in Section 6.2.4.1, where were compared the value of the specific surface area of the adsorbed surfactant, S/V , in presence and in absence of the silica for each mixture ratio based on $\frac{1}{2}\Gamma_{\text{mx}}$ C_{12}DAO (*c.f.* Table 6.4 and 6.7). A comparison of the scattering curves of $\text{C}_{12}\text{DAO}:\beta\text{-C}_{10}\text{G}_2$ and $\text{C}_{12}\text{DAO}:\beta\text{-C}_{12}\text{G}_2$ mixtures at the ratio 1:1 in $\text{H}_2\text{O}/\text{D}_2\text{O}$ in the absence and presence of silica is shown in Figure 6.9. The scattering curves of $\text{C}_{12}\text{DAO}:\beta\text{-C}_n\text{G}_2$ 1:1 mixtures in the absence and presence of the silica nearly coincide in the high- q region, suggesting that the surface area S/V and the shape of the mixed surface micelles are not altered in presence of silica nanoparticles.

The data for the aqueous solution of $\text{C}_{12}\text{DAO}:\beta\text{-C}_{10}\text{G}_2$ and $\text{C}_{12}\text{DAO}:\beta\text{-C}_{12}\text{G}_2$ mixture at the ratio 1:1 can be represented by a model of oblate ellipsoids, with $a = 1.37$ and 1.41 nm and $b = 2.20$ and 2.68 nm, respectively (*c.f.* Table 6.5).

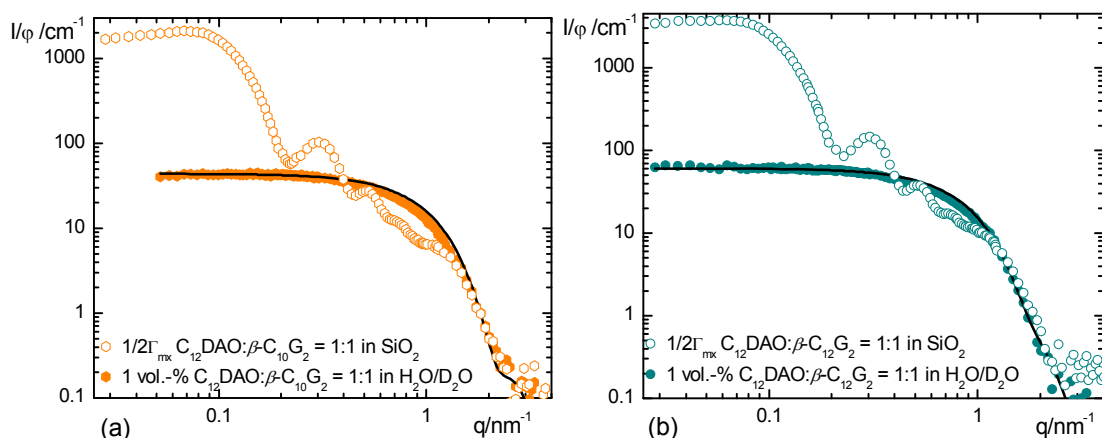


Figure 6.9. SANS profiles $I(q)$ for the surfactant mixtures at ratio 1:1 in the contrast matching H_2O/D_2O in the absence and presence of silica: (a) $C_{12}DAO:\beta-C_{10}G_2$; (b) $C_{12}DAO:\beta-C_{12}G_2$. The scattered intensities were normalized with volume fraction ϕ of the surfactant in the system.

Accordingly, the parameters R_n and R_{lat} of the surface micelle model were first set to these values for all mixing ratios based on the surface concentration $\frac{1}{2}\Gamma_{mx} C_{12}DAO$, and the number of micelles, N_{mic} , was taken as the only adjustable parameter. Figure 6.10 shows the fits for both systems on silica. A good fit of the data in the entire q range was found with a value of R_n similar to R_n for pure $C_{12}DAO$ surface micelles, $R_n = 1.47$ nm (see Table 6.8 and Table 5.5 in chapter 5), which is slightly higher than the parameter a of the mixed micelles in bulk solution, and with values of R_{lat} lower than the parameter b of the mixed micelles in solutions. This is particularly true in the system $C_{12}DAO:\beta-C_{12}G_2$ in the range of small concentrations of $\beta-C_{12}G_2$. It should be mentioned that for this set of mixtures negligible differences between the fits is found when R_n is varied in the range from 1.35 nm to 1.47 nm. The value $R_n = 1.47$ nm was chosen because it gives the representation of the position of the second peak at $q \approx 0.52$ nm⁻¹, which apparently is related to the density of the adsorbed surfactant layer. The values of N_{mic} derived from the fits (Table 6.8) are similar as those found in the simple geometric analysis (Table 6.7) and show the same trends.

The results shown in Figure 6.10 and Table 6.8 are typical for these systems and similar results are obtained for the set of samples B, C and D in silica sol as described in Table 6.6. Figures and Tables summarizing the results for the fits

by the micelle-decorated silica model of these further mixtures are summarized in Appendix. However, the scattering profile for $C_{12}DAO:\beta-C_{12}G_2$ at the mass ratio 1:3 and at 1 vol.-% exhibits features in the q -range after the second peak at $q \approx 0.52 \text{ nm}^{-1}$ which are different from those of the other mixing ratios and from mixtures with $\beta-C_{10}G_2$ (see Figure 6.11). This disagreement with the $C_{12}DAO/\beta-C_{12}G_2$ 1:3 mixture in silica sol is discussed later.

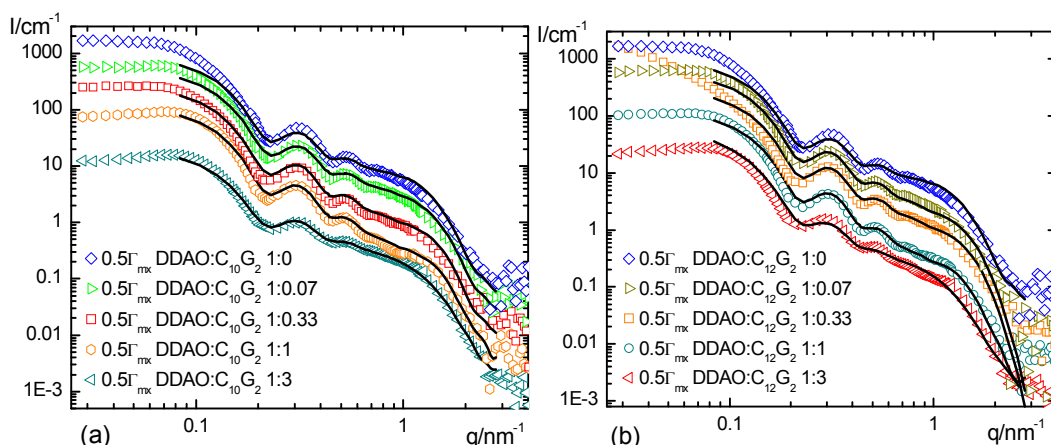


Figure 6.10. SANS profiles $I(q)$ for silica with adsorbed surfactant mixtures based on the surface concentration $\frac{1}{2}\Gamma_{mx}$ of $C_{12}DAO$ in the contrast matching H_2O/D_2O at pH 9 and 298 K (same data as in Fig. 6.7) and fits by the micelle-decorated silica model for oblate ellipsoidal micelles (solid curves): (a) $C_{12}DAO:\beta-C_{10}G_2$; the curves with higher amounts of $C_{12}DAO$ are displaced vertically by factors of 4 (1:1), 12 (1:0.33), 40 (1:0.07) and 85 (1:0) relative to that of the mixture with ratio 1:3. (b) $C_{12}DAO:\beta-C_{12}G_2$; the curves with higher amounts of $C_{12}DAO$ are displaced vertically by factors of 4 (1:1), 18 (1:0.33), 40 (1:0.07) and 85 (1:0) relative to that of the mixture with ratio 1:3.

Table 6.8. Parameters of the micelle-decorated silica model for $\frac{1}{2}\Gamma_{mx}$ $C_{12}DAO:\beta-C_nG_2$ mixtures (set A) on silica particles.*

Sample	$\frac{1}{2}\Gamma_{mx}$ $C_{12}DAO:\beta-C_{10}G_2$			$\frac{1}{2}\Gamma_{mx}$ $C_{12}DAO:\beta-C_{12}G_2$		
	R_n (nm)	R_{lat} (nm)	N_{mic}	R_n (nm)	R_{lat} (nm)	N_{mic}
1 : 0	1.47	2.20	55	1.47	2.20	55
1 : 0.07	1.47	2.00	65	1.47	1.90	82
1 : 0.33	1.47	2.00	85	1.47	1.90	82
1 : 1	1.47	2.00	85	1.47	2.10	84
1 : 3	1.47	2.00	36	1.47	2.40	30

* normal radius R_n , lateral radius R_{lat} , and number N_{mic} of the oblate ellipsoidal surface micelles.

In the case of 1 vol.-% of $C_{12}DAO:\beta-C_nG_2$ mixtures, the best fit is found by fixing the value of R_n to the corresponding value of rotational semi-axis a of

oblate ellipsoidal mixed surfactant aggregates in aqueous solution (see Table 6.5) and adjusting only the values of R_{lat} and N_{mic} . The resulting values of R_{lat} of the surface micelles increase with addition of $\beta\text{-C}_n\text{G}_2$ in the mixture (see Table 6.9), but in general, they remain lower than the corresponding values of the equatorial semi-axis b of the surfactant aggregates in solution, indicating some difference of the oblate micelles adsorbed on silica compared to those in aqueous solution.

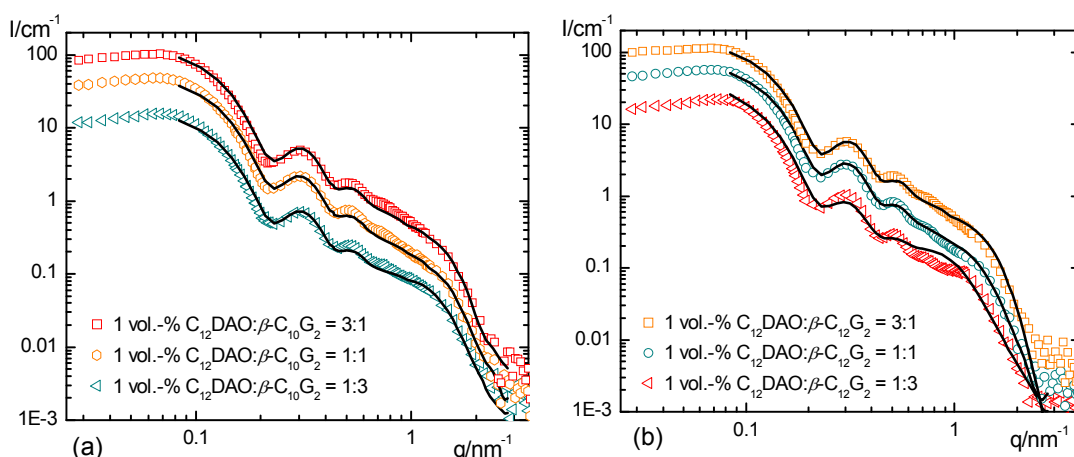


Figure 6.11. SANS profiles $I(q)$ for silica with adsorbed surfactant mixtures with a total concentration of 1 vol.-% in the contrast matching $\text{H}_2\text{O}/\text{D}_2\text{O}$ at pH 9 and 298 K and fits by the micelle-decorated silica model for ellipsoidal micelles (solid curves): (a) $\text{C}_{12}\text{DAO}:\beta\text{-C}_{10}\text{G}_2$; (b) $\text{C}_{12}\text{DAO}:\beta\text{-C}_{12}\text{G}_2$. For both systems the curves with higher amounts of C_{12}DAO are shifted vertically relative to that of mixture with ratio 1:3 by factors of 2 (ratio 1:1), 4 (ratio 3:1).

As can be seen in Fig. 6.11b, the scattering profile of the 1 vol.-% of $\text{C}_{12}\text{DAO}:\beta\text{-C}_{12}\text{G}_2$ 1:3 mixture is not represented well in the q region from 0.43 nm^{-1} to 1.13 nm^{-1} . In this region the fit is directly affected by the value of the structural parameter R_{lat} , as has been explained and demonstrated in chapter 5 (c.f. Fig. 5.9). We have varied this parameter in a range from 0.5 to 5.0 nm, keeping $R_n = 1.41 \text{ nm}$ and $N_{\text{mic}} = 32$ fixed, in order to find an appropriate value of R_{lat} which can best describe the surface micelles formed by the $\text{C}_{12}\text{DAO}:\beta\text{-C}_{12}\text{G}_2$ mixture at ratio 1:3. These fits are shown in Fig. 6.12. A decrease of R_{lat} from 3.0 to 1.5 and 0.5 nm causes a deformation of the size of the surface aggregates as their shell is no longer well defined. An increase of R_{lat} to 5.0 nm causes a strong oscillation at $q \approx 0.78 \text{ nm}^{-1}$, indicating intermicellar strong

oscillation at $q \approx 0.78 \text{ nm}^{-1}$, indicating intermicellar repulsion between the adsorbed surface aggregates.

Table 6.9. Parameters of the micelle-decorated silica model for 1 vol.-% of $\text{C}_{12}\text{DAO}:\beta\text{-C}_{12}\text{G}_2$ mixtures (set D) on silica particles.*

1 vol.-% $\text{C}_{12}\text{DAO}:\beta\text{-C}_{10}\text{G}_2$				1 vol.-% $\text{C}_{12}\text{DAO}:\beta\text{-C}_{12}\text{G}_2$		
Sample	R_n (nm)	R_{lat} (nm)	N_{mic}	R_n (nm)	R_{lat} (nm)	N_{mic}
3 : 1	1.35	1.90	90	1.42	1.90	82
1 : 1	1.37	1.90	80	1.41	2.00	74
1 : 3	1.30	2.20	65	1.41	3.00	32

* normal and lateral radius R_n and R_{lat} , respectively; and number N_{mic} of the oblate ellipsoidal surface micelles.

In this case, the structural parameter R_n was not varied because, as we explained in chapter 5, R_n is directly related to the size of the ellipsoidal aggregates and increasing or decreasing its value causes a shift of the local maximum q_{max} to lower or higher q , respectively. And we found a very nice representation of the data at low- q and at the local maximum q_{max} with $R_n = 1.41 \text{ nm}$.

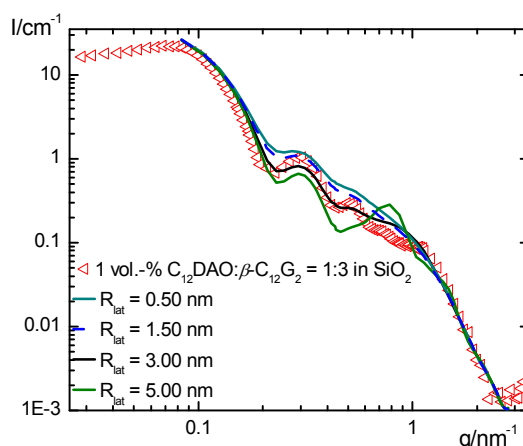


Figure 6.12. Scattering profile for of 1 vol.-% of $\text{C}_{12}\text{DAO}:\beta\text{-C}_{12}\text{G}_2$ mixture at ratio 1:3 on silica and results predicted by the micelle-decorated silica model for ellipsoidal surface micelles varying the lateral semi-axis R_{lat} , at fixed $R_n = 1.41 \text{ nm}$ $N_{\text{mic}} = 32$.

6.2.5 Effect of the maltoside surfactants on the adsorption of C_{12}DAO on silica

Preceding studies have shown that sugar-based surfactants hardly adsorb on hydrophilic silica [6.3c, 6.26, 6.29]. However, Matsson et. al. [6.3c] reported

that adsorption of β -C_nG_m surfactants on silica can be promoted by addition of a second surfactant, leading to a partial or complete coating of the silica. Our SANS study confirms that C₁₂DAO can induce adsorption of β -C_nG₂ on silica through the formation of mixed surface micelles of similar structure and similar or smaller dimensions as those found in aqueous solution. As is seen in Fig. 6.10, the scattering profile of silica sol with C₁₂DAO at a surface concentration of $\frac{1}{2}\Gamma_{\text{mx}}$ is not modified qualitatively by addition of β -C_nG₂, which may suggest that the maltoside surfactant is not incorporated into the adsorbed surface micelle of C₁₂DAO and remains in bulk. However, the quantitative structural information extracted from the fits indicates that additions of small amounts of β -C_nG₂ to the silica sol with $\frac{1}{2}\Gamma_{\text{mx}}$ of C₁₂DAO causes an increase of the number of adsorbed ellipsoidal surface micelles by co-adsorption of β -C_nG₂ into the adsorbed surface micelles of C₁₂DAO, presumably due to through hydrophobic interactions. Presumably the integration of β -C_nG₂ in the ellipsoidal surface aggregates of C₁₂DAO make these surface micelles more stable by reducing the steric repulsion between the head groups of the amino oxide surfactant thus causing a decrease of their effective head group size. However, with increasing the amount of β -C_nG₂ in the mixture the lateral radius R_{lat} of the surface micelles increases. This behaviour is more pronounced in the mixtures with β -C₁₂G₂ than with β -C₁₀G₂, and the number of mixed surface micelles decreases drastically when the amount of β -C_nG₂ is three times that of C₁₂DAO. Tentatively, we explain this trend by decreasing strength of adsorption of the surface micelles when the number of maltoside head group is gradually increased, so that mixed micelles in solution become more favourable than mixed surface micelles. Presumably the reason for this behavior is the stronger hydrophilicity of the maltoside head group compared to the amino oxide group [6.32], so that mixed micelles with high mass ratio of β -C_nG₂, prefer the hydrogen bond formation to water molecules rather than to the silica surface.

In the case of the mixture of 1 vol.-% of C₁₂DAO: β -C₁₂G₂ 1:3 in silica sol, it seems that the surface aggregates have a different morphology than at lower mass ratios of β -C₁₂G₂. This change is hinted by the behaviour in the q range from 0.43 nm⁻¹ to 1.13 nm⁻¹ of the scattering profile, see Fig. 6.11), where we

could not get a good representation of the data with the oblate ellipsoids surface micelles model. It has also been demonstrated in the previous section that the problem to model this kind of morphology is not related to lateral interactions between the surface micelles. We think that at this high concentration of the surfactant mixture (1 vol.-%) and high contents of β -C₁₂G₂ (mass ratio 1:3), larger surface micelles are formed on the silica nanoparticles, possibly in form of cylindrical aggregates. We conjecture that cylindrical surface aggregates are formed, because mixed cylindrical micelles instead of oblate ellipsoidal micelles are formed in aqueous solutions (see Section 6.2.3.1 and 6.2.3.2). However, the driving force for this morphological transition from ellipsoidal to cylindrical shape of the surface aggregates at that composition is not clear. Further work such as rheological investigations are needed to clarify the reason of the growth of these surface micelles when the content of β -C₁₂G₂ in the mixtures increases at an overall surfactant concentration of 1 vol.-%

References of Chapter 6

- [6.1] (a) Nagarajan, R. *Langmuir* **1985**, *1*, 331-341. (b) Hall, D. G.; Huddleston, R. W. *Colloids Surf.* **1985**, *13*, 209-219. (c) Shiloach, A.; Blankschtein, D. *Langmuir*, **1998**, *14*, 7166-7182. (d) Bergström, M.; Eriksson, J. C. *Langmuir*, **2000**, *16*, 7173-7181.
- [6.2] (a) Zhang, L.; Somasundaran P. *J. Colloid Interface Sci.*, **2006**, *302*, 20–24. (b) Zhang, L.; Zhang, R.; Somasundaran P. *J. Colloid Interface Sci.*, **2006**, *302*, 25–31.
- [6.3] (a) Harwell, J. H.; Roberts, B. L.; Scamehorn, J. F. *Colloids Surf. A*, **1988**, *32*, 1-17. (b) Somasundaran, P.; Fu, E.; Xu, Q. *Langmuir* **1992**, *8*, 1065-1069. (c) Matsson, M. K.; Kronberg, B.; Claesson, P. M. *Langmuir* **2005**, *21*, 2766-2772.
- [6.4] Lu, J. R.; Thomas, R. K.; Penfold, J. *Adv. Colloid Interface Sci.* **2000**, *84*, 143-304.
- [6.5] Bain, C. D.; Davies, P. B.; Ward, R. N. *Langmuir* **1994**, *10*, 2060-2063.
- [6.6] (a) McKenna, C. E.; Knock, M. M.; Bain, C.D. *Langmuir* **2000**, *16*, 5853-5855. (b) Watry, M.R.; Brown, M.G.; Richmond, G.L. *Appl. Spectrosc.* **2001**, *55*, 321A-340A.
- [6.7] (a) Manne, S.; Gaub, H.E. *Science*, **1995**, *270*, 1480-1482. (b) Patrick, H. N.; Warr, G. S.; Manne, S.; Aksay, I. A. *Langmuir* **1997**, *13*, 4349-4356. (c) Ducker, W. A.; Wanless, E. J. *Langmuir* **1999**, *15*, 160-168.
- [6.8] (a) Penfold, J.; Staples, E.J.; Tucker, I.; Thompson, L.J. *Langmuir* **1997**, *13*, 6638-6643. (b) Penfold, J.; Tucker, I.; Thomas, R. K. *Langmuir* **2005**, *21*, 6330-6336.
- [6.9] Brinck, J.; Tiberg, F. *Langmuir* **1996**, *12*, 5042-5047.

- [6.10] Stöber, W.; Fink, A.; Bohn, E. *J. Colloid Interface Sci.* **1968**, 26, 62-69.
- [6.11] Phillips, J. N. *Trans. Faraday Soc.* **1955**, 51, 561-569.
- [6.12] Rosen, M. J.; Sulthana, S. B. *J. Colloid Interface Sci.* **2001**, 239, 528-534.
- [6.13] (a) Rathman, J. F.; Christian, S. D. *Langmuir* **1990**, 6, 391-395. (b) Maeda, H.; Muroi, S.; Ishii, M.; Kakehashi^a, R.; Kaimoto, H.; Nakahara, T.; Motomura, K. *J. Colloid Interface Sci.* **1995**, 175, 497-505.
- [6.14] Hines, J. D.; Thomas, R. K.; Garrett, P. R.; Rennie, G. K.; Penfold, J. *J. Phys. Chem. B* **1997**, 101, 9215-9223.
- [6.15] Porte, G. in *Neutrons, X-rays and Light: Scattering Methods Applied to Soft Condensed Matter*, **2002**, 1st edn. ed. P. Lindner and Th. Zemb, Elsevier, Boston, chap. 12 pp. 299-315.
- [6.16] Lipfert, J.; Columbus, L.; Chu, V. B.; Lesley, S. A.; Doniach S. *J. Phys. Chem. B* **2007**, 111, 12427-12438.
- [6.17] Thiagarajan, P.; Tiede, D. M. *J. Phys. Chem.*, **1994**, 98, 10343-10351.
- [6.18] (a) Herrmann K. W. *J. Phys. Chem.* **1962**, 66, 295-300. (b) Garamus, V.; Kameyama, K.; Kakehashi, Rie; Maeda, H. *Colloid & Polymer Science* **1999**, 277, 868-874.
- [6.19] (a) Cecutti, C.; Focher, B.; Perly, B.; Zemb, T. *Langmuir* **1991**, 7, 2580-2585. (b) Dupuy, C.; Auvray, X.; Petipas, C. *Langmuir* **1997**, 13, 3965-3967. (c) Bäverbäck, P.; Oliveira, C. L. P.; Garamus, V. M.; Vargas, I.; Claesson, P. M.; Pedersen, J. S. *Langmuir* **2009**, 25, 7296-7303.
- [6.20] Majhi, P. R.; Dubin, P. L.; Feng, X.; Guo, X.; Leermakers, F. A. M.; Tribet C. *J. Phys. Chem. B*, **2004**, 108, 5980-5988
- [6.21] Bäverbäck, P. Ph.D Thesis **2009**, chap. 4, pp. 39-58.
- [6.22] Kohlbrecher, J., User Guide for the SASfit software package, Paul Scherrer Institute, Laboratory for neutron scattering, **2009** Edition. Available as pdf (SASfit.pdf) from <http://sans.web.psi.ch/SANSSoft/sasfit.pdf>
- [6.23] Garamus, V. M.; Pedersen, J. S.; Maeda, H.; Schurtenberger, P. *Langmuir*, **2003**, 19, 3656-3665.
- [6.24] Lugo, D.; Oberdisse, J.; Lapp, A.; Findenegg, G.H. *J. Phys. Chem. B* **2010**, *accepted*.
- [6.25] Tanford, C. *J. Phys. Chem.* **1972**, 76, 3020-3024.
- [6.26] Zhang, L.; Somasundaran, P.; Maltesh, C. *J. Colloid Interface Sci.*, **1997**, 191, 202-208.
- [6.27] (a) Cummins, P.G.; Staples, E.; Penfold, J. *J. Phys. Chem.* **1990**, 94, 3740-3745. (b) Cummins, P.G.; Staples, E.; Penfold, J. *J. Phys. Chem.* **1991**, 95, 5902-5905. (c) Cummins, P.G.; Penfold, J.; Staples, E. *J. Phys. Chem.* **1992**, 96, 8092-8094.
- [6.28] Pusey, P.N. in *Neutrons, X-rays and Light: Scattering Methods applied to Soft Condensed Matter* **2000**, ed. B.J. Gabrys, Gordon and Breach Science Publishers, Netherlands, 1st ed., chap. 4, pp. 77-102.
- [6.29] Lugo, D.; Oberdisse, J.; Karg, M.; Schweins, R.; Findenegg, G.H. *Soft Matter* **2009**, 5, 2928-2936.

- [6.30] Matsson, M.K.; Kronberg, B.; Claesson, P.M. *Langmuir*, **2004**, *20*, 4051-4058.
- [6.31] (a) Despert, G.; Oberdisse, J. *Langmuir* **2003**, *19*, 7604-7610. (b) Oberdisse, J. *Phys. Chem. Chem. Phys.* **2004**, *6*, 1557-1561.
- [6.32] Zana, R. *J. Phys. Chem. B* **1999**, *103*, 9117-9125.

7 Summary and Outlook

The main motivation of this work was find out if the replacement of a flat surface by a highly curved surface has an effect on the adsorption and on the structure of the adsorbed surfactant layers. Such an effect seems likely when the curvature of the solid surface comes close to the spontaneous curvature of surfactant films. An understanding of the structure of surfactant layers on this kind of surface, *i.e.* colloidal particles, is of vital importance for the fabrication of nano-structured functional surfaces. Specifically, adsorbed surfactant films play an important role as a protection layer for the steric stabilization of colloidal dispersions for the preparation of paints, printing inks, agrochemicals, etc. A further point of interest in this work was to gain a better understanding of the effect of surfactant on the stability of the colloidal dispersion in a surfactant deficient regime, when the amount of surfactant is not enough to attain saturation adsorption.

For this reason, in the present work we have studied the adsorption of three different classes of nonionic surfactants on silica nanoparticles suspended in aqueous solutions (silica sols). The surfactants studied were sugar-based surfactants (C_nG_m), specifically decyl- β -maltoside (β - $C_{10}G_2$) and dodecyl- β -maltoside (β - $C_{12}G_2$); the alkylethoxylate surfactant pentaethylene glycol monododecyl ether ($C_{12}E_5$); and the amine oxide surfactant dodecyldimethylamine N-oxide ($C_{12}DAO$), an amphoteric surfactant that behaves like a cationic surfactant at low pH and as a nonionic surfactant at pH above 7. The choice of the two first classes of surfactants was motivated mainly by their opposite adsorption behavior on hydrophilic silica. The choice of the third one was based on its zwitterionic nature. Silica nanoparticles were used in view of their widespread industrial applications in different fields, such as catalysis, electronics, health care, ceramics and so on. The studies were made with the home-made silica instead of commercial Ludox in order to attain a better control of the mean particle size, a lower polydispersity and a better colloidal stability of the samples. Therefore, the silica nanoparticles were synthesized by two variants of the Stöber synthesis. The preparation of

nanoparticles of smaller size (diameter 16 to 28 nm) was made by particle growth from Ludox SM-30 and Ludox HS-40 dispersions. The larger particles (~40 nm) were prepared by the classical Stöber synthesis.

The study of the self-assembly structures of the nonionic surfactants on colloidal silica was divided into three sections:

1. Surface aggregate structure of nonionic surfactants on small silica nanoparticles.
2. Effect of nanoparticle size on the morphology of adsorbed surfactant layers.
3. Aggregate structure of mixtures of sugar-based surfactants with an amphoteric surfactant in the aqueous phase and on silica beads.

The structural characterization and analysis of the adsorbed surfactant layer was made by using small-angle neutron scattering (SANS), which allows to study structural details at a length-scale of 1 nanometer and below without perturbing the sample.

1. Surface aggregate structure of nonionic surfactants on small silica nanoparticles

The structure of the adsorbed layer of nonionic surfactants on the surface of silica particles of ca. 16 nm of diameter was studied by a combination of different methods. SANS scattering profiles from dilute dispersions of this silica in contrast-matching $\text{H}_2\text{O}/\text{D}_2\text{O}$ solvent mixture containing a concentration of surfactant two orders of magnitude higher than the *CMC* show that the maltoside surfactants $\beta\text{-C}_{10}\text{G}_2$ and $\beta\text{-C}_{12}\text{G}_2$ interacts very weakly with the silica particles and the scattering profiles resemble those of free micelles which have an oblate ellipsoidal shape. This result conforms with earlier findings of low adsorption levels of sugar surfactants at macroscopic silica surfaces [7.1, 7.2], and shows that the adsorption of these surfactants is not enhanced by strong surface curvature. On the other hand, the alkyl ethoxylate surfactant C_{12}E_5 exhibits strong cooperative adsorption onto the silica particles with a surface concentration plateau value Γ_{mx} similar

to that on flat silica surfaces. The SANS profiles from the dilute dispersion in contrast-matching $\text{H}_2\text{O}/\text{D}_2\text{O}$ exhibit a local maximum at intermediate q values, which is a signature of an adsorbed layer on the surface of the particles and becomes more pronounced with increasing surface concentration of the surfactant. A core-shell model corresponding to a uniform surfactant layer at the surface of the silica particles accounts well for the increase in film thickness with increasing surface concentration, but this model underestimates the surface area of the adsorbed surfactant as extracted from the high- q regime of the scattering spectra. The SANS spectra can be represented very well by the model of micelle-decorated silica beads on the assumption that C_{12}E_5 is adsorbed as individual surface aggregates of spherical geometry. This result supports a report of the literature in which oblate ellipsoidal micelles were found for Triton X-100 on silica nanoparticles [7.3]. The present study shows that an increase of the surface concentration of the surfactant leads to an increasing number of surface aggregates, up to a close packing of spherical surface micelles. The preference of such small surface aggregates is attributed to the high surface curvature of the silica nanoparticles which prevents an effective packing of the hydrophobic chains in a bilayer configuration.

2. Effect of nanoparticle size on the morphology of adsorbed surfactant layers

SANS has been used to study the shape of surface aggregates of C_{12}DAO formed at the surface of spherical silica nanoparticles with diameters from 16 to 42 nm. In agreement with the results for C_{12}E_5 it was found that C_{12}DAO does not form a laterally uniform adsorbed layer on the surface of the silica nanoparticles, but rather they form small surface aggregates. The study presented evidence for a morphological transition of the surface micelles as a function of the particle size of the silica nanoparticles. Spherical surface aggregates are formed on particles of 16 nm, but oblate ellipsoidal surface micelles on silica particles of 27 and 42 nm diameter. As in the case of C_{12}E_5 the formation of spherical surface micelles of C_{12}DAO on the surface of the

smallest silica particles is attributed to the high surface curvature of the nanoparticles which prevents an effective packing of the molecules in a bilayer structure. As the surface curvature of the silica particles decreases with increasing particle size, surface aggregates of lower mean curvature, such as oblate ellipsoids, are favored. The dimensions of the ellipsoidal surface aggregates are similar to those of C₁₂DAO micelles in the aqueous solutions. From a comparison of the present results with those of the preceding studies it was concluded that the shape of the surface aggregates (spherical or ellipsoidal) is not determined by the size of surfactants head group. However, for spherical surface micelles it appears that the nature of the head group can have a strong influence on the maximum number of surface aggregates per particle. Specifically, the maximal number of surface micelles of C₁₂DAO is much smaller than for C₁₂E₅ at the same silica, presumably due to its less hydrophilic character. Further systematic work is needed to clarify the role of surfactant head group – surface interactions on the type of surface aggregates and the maximum number of aggregates on the silica particles.

Work presented in Sections 1 and 2 has presented that the micelle-decorated silica model provides a reliable and versatile basis for determining size and shape and the number of surface aggregates of amphiphiles on spherical nanoparticles from SANS scattering data. The results obtained on the basis of this form-factor model are consistent with those derived by a simple geometric analysis of the Guinier and Porod regimes of the SANS data.

3. Aggregate structure of mixtures of sugar-based surfactants with an amphoteric surfactant in the aqueous phase and on silica beads

In this section the binary surfactant systems of C₁₂DAO:β-C₁₀G₂ and C₁₂DAO:β-C₁₂G₂ have been studied in aqueous solutions in absence and presence of silica nanoparticles with diameters of 27 nm. For both surfactant systems synergistic effects were found in mixed adsorbed monolayers at the air/liquid and in mixed micelles in the aqueous phase. In agreement with the two previous sections it was found that the surfactant mixtures do not cover the silica nanoparticles with a laterally uniform bilayer, but rather form discrete and

mixed surface micelles with similar dimension and structure to those formed in the aqueous solution, *i.e.* oblate ellipsoids with a minor semi-axis R_n and a major semi-axis R_{lat} . Co-adsorption of the maltoside surfactant is presumably induced by the adsorbed $C_{12}DAO$, which provides hydrophobic anchoring sites for maltoside surfactant. Co-adsorption of the maltoside surfactants is reflected by the increase of the number of surface micelles when small amounts of this surfactant are added. However, further addition of the maltoside surfactant causes a drastical decrease of the number of surface aggregates, which is interpreted as a desorption of $C_{12}DAO$ from the surface and its integration into the micelles of the maltoside in the aqueous medium. Such process is expected if the mixed micelles in the bulk solution are energetically more favourable than the mixed surface micelles. The observed synergistic effect in the formation of the mixed micelles in solution is consistent with this interpretation.

Another interesting finding of this study was the existence of morphological transition from ellipsoidal to larger surface micelles at high content of the maltoside surfactant in the mixtures with the same hydrocarbon groups when the total concentration of the mixture is higher than the *CMC* of the surfactant mixture. The reason of this morphological transition of the surface aggregates could not be fully resolved in the present work. Therefore, further investigation of this mixture in silica sol with high content of the maltoside surfactant and at concentrations higher than the *CMC* of the mixture is needed to discover the details of this process.

References of Chapter 7

- [7.1] (a) Király, Z.; Börner, R.H.K.; Findenegg G.H. *Langmuir* 1997, **13**, 3308-3315. (b) Király, Z.; Findenegg G.H. *Langmuir*, 2000, **16**, 8842-8849.
- [7.2] Zhang, L.; Somasundaran, P.; Maltesh, C. *J. Colloid Interface Sci.*, **1997**, *191*, 202-208.
- [7.3] Despert, G.; Oberdisse, J. *Langmuir* **2003**, *19*, 7604-7610.

8 Appendix

Scattering profiles $I(q)$ from silica dispersion with surfactant mixtures $C_{12}DAO/\beta-C_{10}G_2$ and $C_{12}DAO/\beta-C_{12}G_2$

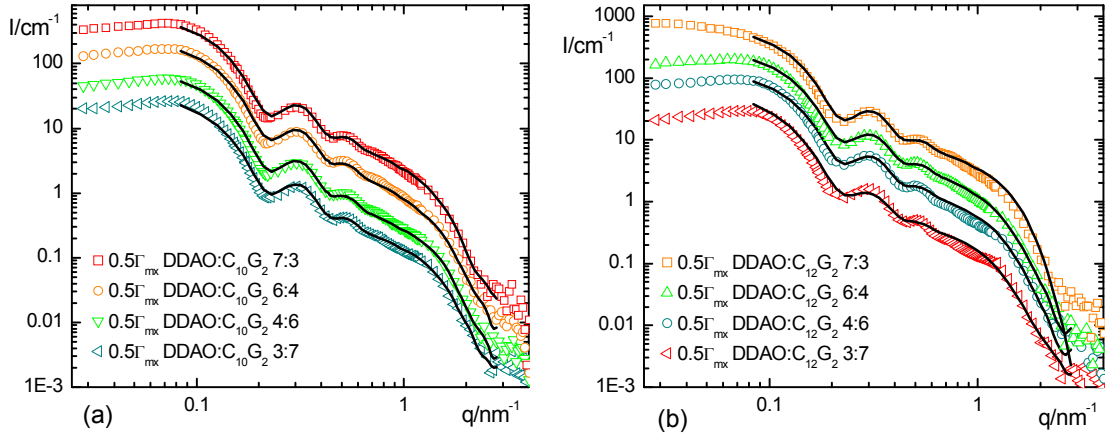


Figure A.1. SANS profiles $I(q)$ for silica with adsorbed surfactant mixtures based on the surface concentration $\frac{1}{2}\Gamma_{\text{mx}}$ of $C_{12}DAO$ in contrast matching H_2O/D_2O at pH 9 and 298 K (set of samples B, where the concentration of $C_{12}DAO$ and of $\beta-C_nG_2$ are varied) and fits by the micelle-decorated silica model for oblate ellipsoidal micelles (solid curves): (a) $C_{12}DAO:\beta-C_{10}G_2$; the curves with higher amounts of $C_{12}DAO$ are displaced vertically by factors of 2 (4:6), 5 (6:4), 12 (7:3) relative to that of the mixture with ratio 3:7. (b) $C_{12}DAO:\beta-C_{12}G_2$; the curves with higher amounts of $C_{12}DAO$ are displaced vertically by factors of 3 (4:6), 6 (6:4), 16 (7:3) relative to that of the mixture with ratio 3:7.

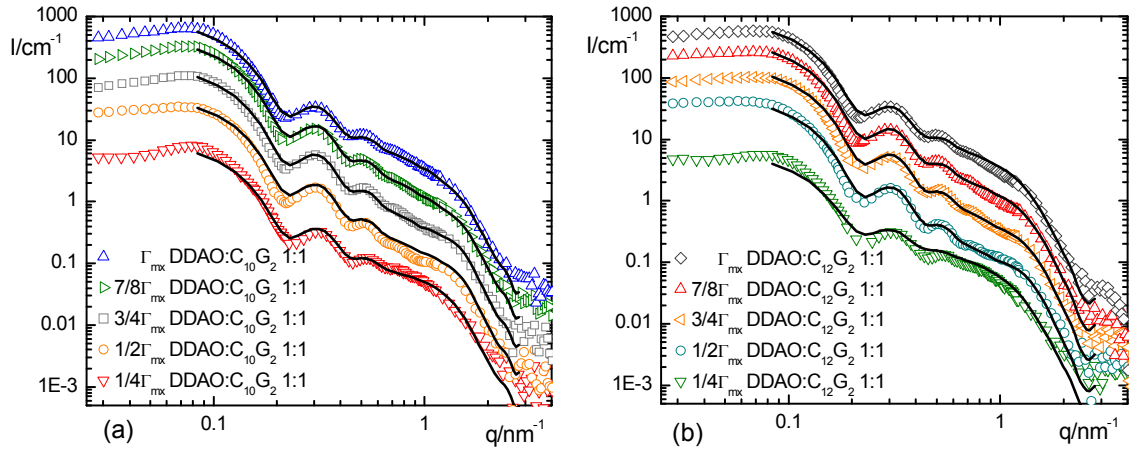


Figure A.2. SANS profiles $I(q)$ for silica with adsorbed surfactant mixtures based on five surface concentrations of $C_{12}DAO$ at a mass ratio 1:1 in the contrast matching H_2O/D_2O at pH 9 and 298 K (set of samples C) and fits by the micelle-decorated silica model for oblate ellipsoidal micelles (solid curves): (a) $C_{12}DAO:\beta-C_{10}G_2$; the curves with higher surface concentration of $C_{12}DAO$ are displaced vertically by factors of 2 ($\frac{1}{2}\Gamma_{\text{mx}}$), 4 ($\frac{3}{4}\Gamma_{\text{mx}}$), 10 ($\frac{7}{8}\Gamma_{\text{mx}}$), 20 (Γ_{mx}) relative to that of $\frac{1}{4}\Gamma_{\text{mx}}$ of $C_{12}DAO$. (b) $C_{12}DAO:\beta-C_{12}G_2$; the curves with higher surface concentration of $C_{12}DAO$ are displaced vertically by factors 1.5 ($\frac{1}{2}\Gamma_{\text{mx}}$), 3 ($\frac{3}{4}\Gamma_{\text{mx}}$), 8 ($\frac{7}{8}\Gamma_{\text{mx}}$), 18 (Γ_{mx}) relative to that of $\frac{1}{4}\Gamma_{\text{mx}}$ of $C_{12}DAO$.

Parameters of Geometric Modelling

Table A.1. Characteristics of the surfactant layer adsorbed on the silica nanoparticles derived from the SANS data of the set of samples B^{†,*}.

Sample	R_g (nm)	δ_{eff} (nm)	S/V (10^5 cm^{-1})	V_{dry} (10^3 nm^3)	N_{mic}
$\frac{1}{2}\Gamma_{\text{mx}} \text{C}_{12}\text{DAO}:\beta\text{-C}_{10}\text{G}_2$					
7 : 3	15.59	1.27	2.61	3.11	86
6 : 4	15.56	1.22	2.97	3.26	75
4 : 6	15.71	1.52	3.98	4.53	88
3 : 7	15.64	1.38	3.56	3.20	62
$\frac{1}{2}\Gamma_{\text{mx}} \text{C}_{12}\text{DAO}:\beta\text{-C}_{12}\text{G}_2$					
7 : 3	16.08	2.26	1.62	2.68	65
6 : 4	15.59	1.28	1.78	2.90	48
4 : 6	15.72	1.54	2.67	4.38	22
3 : 7	16.00	2.10	2.27	3.16	16

[†]prepared by varying the concentration of both surfactants; *gyration radius R_g , effective thickness δ , volume-based surface area S/V and dry volume V_{dry} of the adsorbed surfactant layer; N_{mic} is the number of surface micelles

Table A.2. Characteristics of the surfactant layer adsorbed on the silica nanoparticles derived from the SANS data of the set of samples C.*

Sample	R_g (nm)	δ_{eff} (nm)	S/V (10^5 cm^{-1})	V_{dry} (10^3 nm^3)	N_{mic}
$Z\Gamma_{\text{mx}} \text{C}_{12}\text{DAO}:\beta\text{-C}_{10}\text{G}_2$ 1:1					
$Z = \frac{1}{4}$	16.14	2.37	1.39	3.46	79
$Z = \frac{1}{2}$	15.37	0.85	1.72	3.30	76
$Z = \frac{3}{4}$	16.30	2.70	2.22	4.45	102
$Z = \frac{7}{8}$	15.97	2.04	3.07	4.37	100
$Z = 1$	15.74	1.58	3.25	3.41	78
$Z\Gamma_{\text{mx}} \text{C}_{12}\text{DAO}:\beta\text{-C}_{12}\text{G}_2$ 1:1					
$Z = \frac{1}{4}$	16.12	2.33	1.25	2.36	39
$Z = \frac{1}{2}$	16.18	2.46	1.37	5.49	90
$Z = \frac{3}{4}$	15.75	1.60	2.18	4.57	75
$Z = \frac{7}{8}$	15.74	1.57	2.14	3.89	64
$Z = 1$	15.72	1.54	2.14	3.16	52

*gyration radius R_g , effective thickness δ , volume-based surface area S/V and dry volume V_{dry} of the adsorbed surfactant layer; N_{mic} is the number of surface micelles

Table A.3. Characteristics of the surfactant layer adsorbed on the silica nanoparticles derived from the SANS data of the set of samples D.*

Sample	R_g (nm)	δ_{eff} (nm)	S/V (10^5 cm^{-1})	V_{dry} (10^3 nm^3)	N_{mic}
1 vol.-% $\text{C}_{12}\text{DAO}:\beta\text{-C}_{10}\text{G}_2$					
3 : 1	16.15	2.40	1.77	3.13	92
1 : 1	16.28	2.67	2.13	4.13	95
1 : 3	16.44	2.98	2.84	3.85	75
1 vol.-% $\text{C}_{12}\text{DAO}:\beta\text{-C}_{12}\text{G}_2$					
3 : 1	16.09	2.28	1.64	3.60	87
1 : 1	16.27	2.63	1.92	4.61	76
1 : 3	16.54	3.18	1.59	5.16	25

*gyration radius R_g , effective thickness δ , volume-based surface area S/V and dry volume V_{dry} of the adsorbed surfactant layer; N_{mic} is the number of surface micelles

Parameters of the Micelle-Decorated Silica Model

Table A.4. Parameters of the micelle-decorated silica model for $\frac{1}{2}\Gamma_{\text{mx}} \text{C}_{12}\text{DAO}:\beta\text{-C}_n\text{G}_2$ mixtures (set A[‡]) on silica particles with a fixed layer thickness of 4.0 nm.*

Sample	$\varphi_{\text{tot}}\%$	ρ_{surf} (10^9 cm^{-2})	X	V_{tot} (10^3 nm^3)	A_{tot} (10^4 nm^2)
$\frac{1}{2}\Gamma_{\text{mx}} \text{C}_{12}\text{DAO}:\beta\text{-C}_{10}\text{G}_2$					
1 : 0	0.61	-1.22	0.41	4.85	1.72
1 : 0.07	0.64	-0.71	0.50	5.92	1.77
1 : 0.33	0.76	0.84	0.57	6.80	2.25
1 : 1	1.09	3.95	0.74	8.78	3.25
1 : 3	2.04	8.27	0.77	9.17	8.74
$\frac{1}{2}\Gamma_{\text{mx}} \text{C}_{12}\text{DAO}:\beta\text{-C}_{12}\text{G}_2$					
1 : 0	0.61	-1.22	0.41	4.85	1.72
1 : 0.07	0.40	-0.88	0.50	5.92	1.61
1 : 0.33	0.52	0.59	0.50	5.92	1.75
1 : 1	0.66	3.32	0.71	8.37	2.51
1 : 3	1.37	7.34	0.89	10.58	6.80

[‡]constant concentration of C_{12}DAO and variable concentration of $\beta\text{-C}_n\text{G}_2$; *total volume fraction of the surfactant φ_{tot} , scattering length density of the surfactant layer ρ_{surf} , effective volume fraction of surfactant in the shell X , real adsorbed surfactant volume V_{tot} , total surface area of the adsorbed surfactant A_{tot} .

Table A.5. Parameters of the micelle-decorated silica model for $\frac{1}{2}\Gamma_{\text{mx}}$ C₁₂DAO: β -C_nG₂ mixtures (set B[‡]) on silica particles with a fixed layer thickness of 4.0 nm.*

Sample	$\varphi_{\text{tot}}\%$	ρ_{surf} (10^9 cm^{-2})	X	V_{tot} (10^3 nm^3)	A_{tot} (10^4 nm^2)
$\frac{1}{2}\Gamma_{\text{mx}}$ C₁₂DAO:β-C₁₀G₂					
7 : 3	1.64	1.43	0.89	10.58	4.79
6 : 4	1.64	2.71	0.89	10.58	5.45
4 : 6	1.41	7.18	0.95	11.23	7.31
3 : 7	1.55	5.56	0.87	10.25	6.54
$\frac{1}{2}\Gamma_{\text{mx}}$ C₁₂DAO:β-C₁₂G₂					
7 : 3	1.63	1.06	0.77	9.17	2.97
6 : 4	1.76	2.67	0.89	10.58	3.27
4 : 6	1.46	6.48	0.95	11.23	4.89
3 : 7	1.59	4.82	0.87	10.25	4.16

[‡]prepared by varying the concentration of both surfactants; *total volume fraction of the surfactant φ_{tot} , scattering length density of the surfactant layer ρ_{surf} , effective volume fraction of surfactant in the shell X , real adsorbed surfactant volume V_{tot} , total surface area of the adsorbed surfactant A_{tot} .

Table A.6. Parameters of the micelle-decorated silica model for C₁₂DAO: β -C_nG₂ mixtures at a constant mixture ratio 1:1 and different surface concentrations of C₁₂DAO (set C) on silica particles with a fixed layer thickness of 4.0 nm.*

Sample	$\varphi_{\text{tot}}\%$	ρ_{surf} (10^9 cm^{-2})	X	V_{tot} (10^3 nm^3)	A_{tot} (10^4 nm^2)
$Z\Gamma_{\text{mx}}$ C₁₂DAO:β-C₁₀G₂ 1:1					
$Z = \frac{1}{4}$	0.45	5.26	0.46	5.42	2.54
$Z = \frac{1}{2}$	1.09	3.95	0.74	8.78	3.25
$Z = \frac{3}{4}$	1.15	3.86	0.84	9.90	4.08
$Z = \frac{7}{8}$	1.33	4.07	0.89	10.58	5.63
$Z = 1$	1.69	4.19	0.91	10.72	5.97
$Z\Gamma_{\text{mx}}$ C₁₂DAO:β-C₁₂G₂ 1:1					
$Z = \frac{1}{4}$	0.44	3.63	0.39	4.58	2.29
$Z = \frac{1}{2}$	0.66	3.32	0.71	8.37	2.51
$Z = \frac{3}{4}$	1.23	3.55	0.89	10.58	4.00
$Z = \frac{7}{8}$	1.37	3.26	0.87	10.25	3.93
$Z = 1$	1.66	3.28	0.89	10.58	3.94

*total volume fraction of the surfactant φ_{tot} , scattering length density of the surfactant layer ρ_{surf} , effective volume fraction of surfactant in the shell X , real adsorbed surfactant volume V_{tot} , total surface area of the adsorbed surfactant A_{tot} .

Table A.7. Parameters of the micelle-decorated silica model for 1 vol.-% C₁₂DAO:β-C_nG₂ mixtures (set D) on silica particles with a fixed layer thickness of 4.0 nm.*

Sample	$\varphi_{\text{tot}}\%$	ρ_{surf} (10 ⁹ cm ⁻²)	X	V_{tot} (10 ³ nm ³)	A_{tot} (10 ⁴ nm ²)
1 vol.-% C₁₂DAO:β-C₁₀G₂					
3 : 1	1.07	0.93	0.71	8.37	3.25
1 : 1	0.98	3.96	0.74	8.78	3.91
1 : 3	0.92	8.20	0.67	7.94	5.22
1 vol.-% C₁₂DAO:β-C₁₂G₂					
3 : 1	1.10	0.72	0.63	7.48	3.01
1 : 1	1.03	3.36	0.62	7.39	3.53
1 : 3	0.96	7.27	0.57	6.80	2.92

*total volume fraction of the surfactant φ_{tot} , scattering length density of the surfactant layer ρ_{surf} , effective volume fraction of surfactant in the shell X , real adsorbed surfactant volume V_{tot} , total surface area of the adsorbed surfactant A_{tot} .

Parameters of the Oblate Micelle-Decorated Silica Model

Table A.8. Parameters of the oblate micelle-decorated silica model for ½Γ_{mx} C₁₂DAO:β-C_nG₂ mixtures (set B[‡]) on silica particles.*

½Γ_{mx} C₁₂DAO:β-C₁₀G₂				½Γ_{mx} C₁₂DAO:β-C₁₂G₂		
Sample	R_n (nm)	R_{lat} (nm)	N_{mic}	R_n (nm)	R_{lat} (nm)	N_{mic}
7 : 3	1.47	1.70	80	1.47	1.80	65
6 : 4	1.47	1.70	80	1.47	1.80	55
4 : 6	1.47	1.90	80	1.47	1.90	55
3 : 7	1.47	1.90	70	1.47	2.40	30

[‡]prepared by varying the concentration of both surfactants; *normal radius R_n , lateral radius R_{lat} , and number N_{mic} of the oblate ellipsoidal surface micelles.

Table A.9. Parameters of the micelle-decorated silica model for C₁₂DAO:β-C_nG₂ mixtures at a constant mixture ratio 1:1 and different surface concentrations of C₁₂DAO (set C) on silica particles.*

ZΓ_{mx} C₁₂DAO:β-C₁₀G₂ 1:1				ZΓ_{mx} C₁₂DAO:β-C₁₂G₂ 1:1		
Sample	R_n (nm)	R_{lat} (nm)	N_{mic}	R_n (nm)	R_{lat} (nm)	N_{mic}
$Z = \frac{1}{4}$	1.47	2.20	55	1.47	2.10	21
$Z = \frac{1}{2}$	1.47	2.00	85	1.47	2.10	84
$Z = \frac{3}{4}$	1.47	2.00	95	1.47	2.00	84
$Z = \frac{7}{8}$	1.47	1.80	92	1.47	2.00	70
$Z = 1$	1.47	1.80	70	1.47	2.00	55

* normal radius R_n , lateral radius R_{lat} , and number N_{mic} of the oblate ellipsoidal surface micelles.